Optimising Temperature and Electromagnetic sensing using Nanodiamonds and Fluorescence Microscopy

Author:
Ryan Corbyn

A thesis submitted in fulfilment of the requirements for the degree of Doctor of Philosophy.

Nanobiophotonics,
Department of Physics,
University of Strathclyde, Glasgow.

Submitted: February 14, 2023

Declaration of Own Work

This thesis is the result of the author's original research. It has been composed by the author and has not been previously submitted for examination which has led to the award of a degree.

Signed: 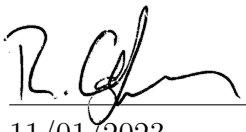

Date: 11/01/2023

Acknowledgements

I would first off like to thank my supervisor Dr Brian Patton, for selecting me for this research project and helping me to develop as a scientist. I have learned so much throughout this project and was given the freedom to learn how to be a scientist, whilst always knowing that I could rely on your support when it was needed. I hope that you have enjoyed having me within your research group as much as I have enjoyed being a part of the team!

Dr Graeme Johnstone, Your help and guidance through the early years of the project were invaluable, working alongside you in the lab I learned so much jamming along to the sounds of BBC Radio 6. I would also like to say a special thank you to you and Dr Alan Kemp for volunteering to read parts of this body of work. I really appreciate the time you took and the comments and suggestions you provided.

To my colleagues within the NanoBioPhotonics research group, the time in the lab/office that we spent together is something I will never forget. You guys all helped to get me through this project, whether it be through helpful suggestions, putting good music on in the lab, or days out in the Scottish countryside. It is amazing to think how far we've all come, and I still find it funny that we are all convinced that each other's projects are better/more interesting than our own.

A group that will likely never read this. Glasgow Raptors RFC, you have played one of the most important roles throughout my PhD. You lot will never truly know how much you helped me through the years of the Pandemic, or how much it meant to me to be chosen as Captain. I am so lucky to have found a team as accepting as you all and I hope that I am able to continue to play with you guys for many years to come!

My friends and family. You have been the cornerstone of everything that I have been able to achieve. To my friends, your ability to always pick me up when I am at my lowest and ensure I have memories that will last forever... and some I will never be able to recall, has been unbelievable during this project. I am

sure you all know (because I've told you numerous times) how tough this project has been at times. Knowing that I can call any of you, day or night, and have a sympathetic ear and a friendly voice is something special, and I just hope you all know how much I appreciate that.

To my family, without you, there is no way I would be where I am today. Luke, I will never stop being amazed at how talented you are, and that will always be an inspiration to keep on trying and never stop learning. Mum and Dad, you two have been the wind in my sails that have gotten me to this point. You have always been there to support me. The sacrifices you made when I was younger so that I could just focus on enjoying my childhood. The core values and work ethic you helped to nurture in me are two of the things that I value most in myself and have been a deciding factor in being able to reach this milestone in my life. I love you both dearly and hope that this thesis is something you can be proud of to have on your shelf.

Finally, to Future Ryan, I hope that this work forever remains a testament to the fact that there is nothing you can't do when you put your mind to it. You should be proud of everything you have achieved in this project, from the work conducted, right thought to the friends you have made. Keep it up, there is nothing you can't do!

Research Restrictions

This research project was completed during the 2020 pandemic caused by the global outbreak of COVID-19. From the period spanning from March 2020 - September 2020 and also January 2021 - Mach 2021, no access to the lab or the university was possible as a result of the restrictions put in place by both the Scottish Government and the University of Strathclyde. As a result of these restrictions, a total of 8 months was lost from this research project.

Throughout this project, I was also hampered in my research as a result of electromagnetic noise generated within the building coupling into our experimental equipment. This noise was generated by one of the research groups within the John Anderson Building, who were utilising a 350 TW laser as part of the Scottish Centre for the Application of Plasma-based Accelerators (SCAPA). The power drawn to operate this laser resulted in the generation of electromagnetic noise within the building's infrastructure that, in turn, coupled into our imaging system via the piezoelectric objective controller. The effect of the noise is discussed in section 3.5.2. To summarise, during the time im which the noise was present in our imaging system, I was limited to proof-of-principle experiments only, and was unable to progress further with my project until the appropriate filters were put in place and separation of power supply completed. The effects of this electromagnetic noise were observed in the imaging system from June 2019 - March 2021.

This statement has been provided so that the reader of this work has an idea of the context for the project. It is merely to highlight the state of global affairs, and the local conditions at the time that this project was undertaken.

Abstract

The motivation behind this research project was to add the capability of magnetic field and temperatures sensing using nanodiamonds as an all-optical probe in biological systems. Fluorescent nanodiamonds are an exciting prospect for use as an optical sensor within the field of biology. Not only does their small size (5 nm - 100 nm) allow them allow the targeting of micro-structures and organelles within single cells, but they have also been shown to be non-cytotoxic. Coupling these characteristics with optically stable fluorescent defects within the diamond structure, fluorescent nanodiamond could be used as a long-lived all optical sensor for investigating sub-cellular environments without impacting or impairing the ordinary function of the cell. The aim of the project was to introduce the ability to perform optically detected magnetic resonance spectroscopy (ODMR) measurements of an ensemble of nitrogen-vacancy (NV^-) defect centres within nanodiamond crystals, with the aim of refining the magnetic and temperature sensing measurement protocols for use in biological systems.

Initial experiments revolved around implementing the well established ODMR measurement regime for use in our confocal system. In this investigation, I discovered that ring resonators were are suitable for use in our experimental set-up, as the oil-immersion objective grounded the microwave field generated, limiting the contrast of the ODMR measurement to under 1% across the region in which a uniform microwave field is produced. More effective for ODMR spectroscopy proved to be the combination of the coplanar waveguide and copper micro-wire antenna for microwave delivery to the sample, regularly resulting in ODMR contrast greater than 10%. I also explored the measurement parameters that can effect the sensitivity of the NV^- centres to an static magnetic field. Throughout this investigation, and optimising the applied excitation and microwave power, I was able to achieve a maximum DC magnetic field sensitivity of $1.13 \pm 0.04\,\mu T/\sqrt{Hz}$.

In the pursuit of the temperature sensing capability of the NV^- centre, I attempted to perform ODMR measurements using the Oko-Labs 301-H temperature stage. The stage was incompatible with our measurements owing to the large sample drift observed when the stage was in operation. This drove the de-

velopment of an ODMR with Referencing measurement scheme that allowed us to compensate for the effects of measurement drift across an experiment. This measurement technique proved to be very powerful and was able to allow for accurate determination of the resonant microwave frequency of the NV^- centre even when faced with 15% loss in fluorescent signal due to drift across the ODMR spectra. Further development of the NV^- thermometry protocol was made with the introduction of a multi-point measurement scheme that had been outlined in literature. The introduction of this measurement scheme still allowed for the measurement of temperature using the ODMR spectra from an NV^- ensemble, despite using just four applied microwave frequencies. In the absence of a suitable environment chamber, I developed a measurement protocol to simulate the effects of a temperature change on the measured ODMR spectra of the NV centre. With this measurement protocol, I was able to compare and contrast three different multi-point ODMR thermometry analysis schemes that had been presented in literature.

Finally, I was able to test the ODMR measurement protocols developed throughout this project on nanodiamonds inside Macrophage and THP1 cells. In these experiments I showed that our confocal system is capable of measure the effect of an applied magnetic field and simulated temperature change on the ODMR spectra of a nanodiamond embedded within biological material. In the case of the simulated temperature change experiments, we were able to determine that the measurement scheme first presented by Fujiwara *et al* in [1] is the most effective measurement scheme for monitoring temperature changes using our measurement system and biological samples.

Contents

List of Figures

List of Tables

Glossary

AO adaptive optics. 18

DSRR double split ring resonator. 51

FSM fast-steering mirror. 14

FWHM full-width half maxima. 82

GFP green fluorescent protein. 2

NA numerical aperture. 14

ND nanodiamond. 3

NV^- negatively-charged nitrogen-vacancy centre. 3

ODMR optically detected magnetic resonance. 4

PALM photoactivated localisation microscopy. 1

PCB printed circuit board. 71

PSF point spread function. 17

RESOLFT reversible saturable optical linear fluorescence transitions. 2

RMS root mean square. 27

SH shack-hartmann. 22

SPAD single photon avalanche diode. 15

SRRF super-resolution radial fluctuations. 1

STED stimulated emission depletion. 2

STORM stochastic optical reconstruction microscopy. 1

Chapter 1

Introduction

The development of the field of bio-physics is an excellent example of the multi-disciplinary nature of modern science. The cross-over between the knowledge already held by the two separate fields of biology and physics has been brought together to advance the understanding of biological systems. An excellent example of this synergy between biology and physics is the rapid development of a host of new microscopy techniques that enable the imaging of biological processes in previously undreamed of detail and precision [5]. Through collaborations with biologists, those working in the field of microscopy have managed to develop systems from the simple table top microscopes developed in the early 1600's which were able to see down only to the single cell level [6], to developing fluorescent imaging systems such as confocal microscopy, which is able to achieve diffraction limited imaging ($\approx 200\,\text{nm} \times 200\,\text{nm}$ laterally) of cellular structure that have been labelled with a fluorescent marker [7, 8]. These advancements have allowed researchers to investigate of the growth of dendrites in neural networks, offering insight into the development of neural pathways over time [9]. Indeed the search for the perfect image has pushed the imaging capability of microscopy further to beat the optical diffraction limit [10, 11, 12, 13]. Techniques such as photo-activated localisation microscopy (PALM), stochastic optical reconstruction microscopy (STORM) and super-resolution radial fluctuation (SRRF) mi-

croscopy all use computational methods to localise the emitters to a resolution of 10's of nanometers [11, 12, 13]. Other techniques such as stimulated emission depletion (STED) microscopy and reversible switchable optical fluorescence transition (RESOLFT) microscopy rely on stimulated emission depletion to beat the diffraction limit and have a resolution that is only limited by the laser power used during imaging [10, 14].

With the development of new imaging techniques are developed and the applications for the technology expands, new challenges arise that need to be addressed. One such challenge is the choice of fluorescent probe used for imaging [15]. Selection of the most appropriate fluorescent probe is a fundamental component of biological imaging as it dictates the ability to target specific biological structures within a sample [16] and the probe may also encode functional information on the state of the biological environment through e.g. emission brightness or wavelength [17]. In addition, there are number of other properties that need to be considered when selecting a fluorescent label for biological imaging, such as:

- Absorption spectra: The probe used must be compatible with the excitation wavelength(s) available from the imaging system.
- Emission spectra: The wavelength emitted by the fluorescent probe must be compatible with the detection properties of the microscope used.
- Labelling mechanism: There are many different techniques that can be used for the labelling of a sample for fluorescent imaging. Expression of green fluorescent protein (GFP) [18], anti-body labelling [19] and DNA-labelling [20] are all examples of labelling techniques that are used routinely in modern biology, other techniques also find regular use depending on the system under study.

- Photo-stability: Having a fluorescent probe that has a stable emission spectra and emission intensity under optical excitation allows for long-term imaging of a sample [21]

- Photo-bleaching: As a result of chemical changes that occur during imaging, many fluorescent probes "bleach" under excitation from an excitation laser and stop emitting, meaning the sample can no longer be imaged using fluorescence microscopy [22].

- Cytotoxicity: Some biological probes, such as quantum dots[23] and GFP [24] have been shown to be toxic to biological material. This poses a problems when investigating live-cell systems as the cell may be stressed due to the presence of the probe in the cell body and, therefore, not behaving naturally, but is instead responding to the toxic effects of the fluorescent probe.

- Phototoxicity: While not specifically related to the probes used in imaging, cells can be stressed to the point of cell death when under illumination from a laser [25]. The relative brightness of a given fluorophore needs to be considered when selecting a probe for imaging. With a relatively bright fluorescent probe, the laser power required to recover an image with good signal to noise can be kept to a minimum [26].

In this work, I investigated the use of fluorescent nanodiamonds (NDs) as optical fluorophores for biological imaging and the sensing of biologically generated magnetic fields and temperature changes within living samples. Nanodiamonds are fluorescent as a result of optically active crystallographic defects within their atomic lattice [27]. The atomic defect of interest for this research project was the negatively charged nitrogen-vacancy (NV^-) centre in diamond [28]. Addressing the considerations as outlined above for choice of fluorophore, nanodiamonds containing NV^- centres:

- Have a single photon absorption spectra ranging from 425 nm to 650 nm [28].
- An emission spectra that ranges from 637 nm to 800 nm [28]. This emission range is the result of the vibronic transitions that can occur within a solid-state emitter, such as the NV^- centre as a result of interactions between lattice phonons and the defect centre itself [29].
- Fluorescent nanodiamonds have been used to label targeted structures within live-cell using anti-body labelling [30]. Antibody labelled ND are now available to buy commercially.
- The fluorescence emission from the NV centre is extremely stable and, as it is a crystallographic defect, does not bleach, so can be continually imaged without losing any of its fluorescence intensity [31].
- Nanodiamond have also been shown to be non-cytotoxic [32].

Taking into account all of the properties outlined here, it is clear that nanodiamonds hold a lot of promise as a fluorescent probe for biological imaging. The NV^- centre is also of particular interest in this project as it has been used to monitor the magnetic fields generated by biological samples [33, 34], and has been used as a temperature probe for monitoring the response of live-cells as they are exposed to different stimuli [35, 1]. With the combination of the properties of the fluorescent nanodiamonds containing the NV^- centre, NDs is an interesting material as an *in vivo* probe for both long-term biological imaging and sensing. The aim of this project has been to implement an experimental protocol called optically detected magnetic resonance spectroscopy (ODMR) to measure both magnetic fields and temperature changes using nanodiamonds located within biological specimen [36, 37].

To assess the effectiveness of the nanodiamond probes for magnetic and temperature field sensing, we will need to compare the sensitivity that we are able to achieve with that reported for current existing technologies. In the case of magnetometry, one of the possible applications for nanodiamond sensing would be to measure the strength of the magnetic field generated by a firing neuron [34]. Current technologies used for such measurements are devices based on superconducting quantum interference devices (SQUIDS) [38] and atomic vapour cells [39]. Both of these techniques offer a magnetic sensitivity for the practical measurement of the magnetic fields produced by a neuron of $< 10\,\mathrm{fT}/\sqrt{\mathrm{Hz}}$ [38, 40]. In the case of SQUIDs, the limiting factor for the sensitivity of the device, is limited to the distance between the sample and the device owing to the need to operate at cryogenic temperatures to maintain the conditions for superconductivity within the detectors [41]. Both detectors are also limited in spatial resolution to the order of a few millimetres as a result of the size of the sensor heads [40, 38]. One of the benefits that of the application of nanodiamonds for biological sensing is the high spatial resolution of the nanodiamond crystals. By employing a confocal microscope system, and labelling the surface of neurons for imaging, we would have a high spatial resolution sensor that is directly in contact with the source of the magnetic field generation [42]. For a single NV^- centre in diamond, the maximum magnetic sensitivity has been calculated to be $3\,\mathrm{nT}/\sqrt{\mathrm{Hz}}$ [43]. The sensitivity of the NV^- based magnetometer increases with the square root of the number of sensors used for the measurement [44]. In this work, I have focused on the use of NV^- ensembles within nanodiamond crystals (diameter $>100\,\mathrm{nm}$) to monitor magnetic fields generated by living organisms. Such experiments have already been performed using NV^- centres within bulk diamond, in which the action potential from a marine fanworm *Myxicola infundibulum* was measured at 3 nT, following the averaging of 600 measurements performed on the same neuron [34]. This is a technique that could be used alongside currently existing

fluorophores, such as GCaMP, that are currently used to monitor the activity of active neurons [45].

Many methods have been explored for sub-cellular temperature measurement and are well reported in the review article by Okabe *et al* [46]. Two examples of *in vivo* temperature probes that have been used previously are Quantum Dots [47] and gold nano-clusters [17]. In each case, the researchers were able to achieve sub-kelvin temperature sensitivity, however each probe does have an associated drawback with the measurement. In the case of the Quantum Dots, temperature sensing was achieved by monitoring fluctuations in the fluorescence emission spectra from the fluorophore as a temperature change was applied [47]. In the case of the gold nano-clusters, the fluorescence life-time of the nano-clusters was monitored as temperature changes were applied to the sample [17]. The difficulty associated with this temperature sensing method is that the effect of temperature on the fluorescence life-time of the nano-clusters was strongly dependent on the media within which the nano-clusters were embedded [17]. To effectively use gold nano-clusters for temperature sensing in live-cell systems, one would need to have a calibration dataset to compare the results against to accurately measure temperature changes in the system [17]. The first identification of the NV^- centre for use in thermometry was in 2010, when Acosta *et al* quantified the temperature dependence of the spin-state transition energies that are monitored during ODMR measurements (see section 3.6). This emerging technology is already being used to monitor temperature changes that occur in micro-electronics [4], as well as monitoring temperature changes within live organisms [35, 1]. The sensitivity reported from these experiments is $1.4\,\mathrm{K}/\sqrt{\mathrm{Hz}}$ [1], with measurement errors reportedly as low as $0.5\,\mathrm{K}$ [4]. One of the benefit of using diamonds for temperature sensing experiments it's thermal conductivity. Diamond has the highest thermal conductivity of any material currently known to science [48], ensuring

fast thermal equilibrium through the crystal as soon as a temperature change occurs. NV^- thermometry using nanodiamond probes has been reported by Fujiwara *et al* in their paper published in 2020, in which the temperature change within *C. elegans* worms was monitored as chemical stimulants were added to their local environment [1]. In this work, the group observed an internal temperature change of up to 8°C over the course of these experiments [1]. From these results, we can see that it is desirable to be able resolve temperature changes on a sub-kelvin scale when performing *in vivo* thermomety experiments.

With the properties outlined above, fluorescent nanodiamond (FND) is a probe that could potentially offer us the chance to observe and investigate the further the temperature dynamics and magnetic field generation within live cell systems beyond that which we have previously seen [31]. With FNDs being both biocompatible and fluorescent, these nanocrystals offer the chance for investigators to insert an optical probe into a live biological sample of interest without impairment of the normal operational cell dynamics. This is something that is rarely achieved with traditional fluorophores that have been shown to be cytotoxic to cells [24]. In addition, FNDs also offer the opportunity to monitor both changes in temperature and magnetic fields within a single cell organism with a spatial resolution limited only by the microscopy technique that is used [49]. The focus of this research was to investigate and implement measurement techniques to use NV^- ensembles in nanodiamond crystals to monitor magnetic fields and temperature gradients within live cells.

1.1 Thesis Structure

Following this introduction, the thesis is organised into the following chapters:

Chapter 2: The Microscope. Here I will give an overview of the bespoke

adaptive-optics enhanced microscope. One of the defining characteristics of this microscope is the ability to remove sample induced aberration using adaptive optics [2]. We have made use of a deformable mirror within the confocal microscope, I have reported on the calibration of the deformable mirror and demonstrated its use improving the quality of the point spread function of the microscope following a realignment of the system.

Chapter 3: ODMR Development. In this chapter I outline the implementation and development of a protocol for optically detected magnetic resonance spectroscopy. The topics discussed here are:

- An overview of the nitrogen-vacancy centre and concepts behind ODMR.
- The characterisation and performance assessment of two different microwave delivery methods.
- The implementation and development of the ODMR techniques used throughout this work.
- An overview of the parameters that can affect the sensitivity of NV magnetometry/thermomerty.

Chapter 4: Towards ODMR for Biosensing. Here I discuss the development of ODMR measurement procedures that are specifically designed for use in biological systems. Included within this chapter is a discussion of:

- The application of adaptive-optics for ODMR measurements.
- The introduction of a multi-point ODMR protocol for temperature sensing.
- The development of a simulated temperature sensing protocol.

- The assessment of three different ODMR temperature sensing analysis protocols against the same experimental dataset.

Chapter 5: ODMR in Fixed Cells. In Chapter 5, I report the use of the ODMR spectroscopy to measure strength of an applied magnetic field and a simulated temperature change using nanodiamonds embedded within the body of a fixed cell. Through our partnership with the Centre for Inflammation Research at Edinburgh University, we were able to obtain samples of fixed immune cells that have had nanodiamonds incorporated into the cell body. In this portion of the thesis I assess the performance of the developed magnetic and temperature sensing algorithms developed as applied to the biological systems of macrophage and THP1 cells. The strengths and weaknesses of the experimental regimes used in this work are identified and suggestions are made for how the sensitivity of the measurements could be improved.

Conclusions: In the conclusions chapter I will summarise the work that has been presented in this thesis. This chapter will be broken-up into three distinct sections to highlight:

- The upgrades made to the confocal microscope.
- The development of the sample preparation routine.
- The creation of an ODMR protocol for bio-sensing.

Future Work: Finally I will discuss the opportunities for future investigations that exist for this project. This chapter will be targeted at both the applications of the further development of the microscope itself and the possible applications of the temperature and magnetic field sensing capabilities that have been outlined previously in the Thesis.

Chapter 2

The Microscope

2.1 Confocal Microscopy

In this body of work, I have made use of a confocal microscope system. Confocal microscopy is a well established technique [8, 50] and has been used extensively for ODMR measurements to investigate the properties of the NV^- centre [36, 51, 52, 53]. The confocal microscope was first designed and built by Marvin Minsky in the 1950's [54]. Minsky designed this confocal microscope to combat the problem of out of focus light reaching the detector when imaging through any extended biological structure, such as neural networks, which affected the image contrast of the wide-field imaging systems available at the time [54]. Optical sectioning was achieved by positioning an optical pinhole in the conjugate imaging plane for both the excitation and detection paths of the microscope [8]. The positioning of the pinholes within the optical path of the microscope are chosen such that:

- The excitation of the sample is confined to a small volume within the sample.
- Any out-of-focus light from the excitation of fluorophores within the cone of illumination is rejected by the detection pinhole [54].

The combination of these two pinholes in the system result in increased spatial

resolution from the confocal arm, with a $\sqrt{2}$ improvement over an equivalent wide-field imaging system [55]. What really sets confocal microscopy apart from wide-field microscopy, however, is the optical sectioning capability of the microscope [8]. With the ability to reject out of focus light, confocal microscopes can be used to construct a 3D volumetric image of a specimen under study [56, 57, 58]. The size of the pinhole used in confocal microscopy is an important factor in the imaging capability of the microscope. For optimal performance, the radius of the pinhole is usually chosen to be the size of an Airy unit. An Airy unit is defined as a radius of the first minima of the diffraction pattern from imaging a point source and is defined as:

$$r_{Airy} = 0.61\frac{\lambda}{NA} \tag{2.1}$$

In which, λ is the wavelength of the fluorescent light and NA is the numerical aperture of the microscope objective [59]. The NA of the objective is given by:

$$NA = n\sin\theta, \tag{2.2}$$

In n is the refractive index of the sample, and θ is the half angle of the cone of illumination from the objective lens [8].

If the pinhole is chosen to be smaller than the size of the first airy disk, then a modest increase in the imaging resolution limit of the microscope is observed, this comes at the expense of the photon flux observed, which can result in increased imaging times to retain the same signal to noise ratio of the image [55]. Conversely, for a specimen of study that has a low signal to noise ratio, the pinhole could be made larger than the airy unit, however, this comes at a detriment of image resolution [8]. As the pinhole size in increased, the resolution limit of the microscope tends towards that of the wide-field imaging systems, with a degra-

dation of the optical sectioning capability of the confocal system.

Confocal microscopes are considered as a point-scanning systems. This means that in order to build up a complete image of a sample, either: the beam is scanned across the sample or the sample is scanned relative to a fixed beam position [54]. The spatial resolution of the microscope is defined by the following equations:

$$\Delta r = 0.4\frac{\lambda}{NA} \tag{2.3}$$

$$\Delta z = 1.4\frac{n\lambda}{NA^2} \tag{2.4}$$

In which, Δr and Δz are the lateral and axial resolution limits for the microscope respectively, λ is the mean value of both the illumination and the emission wavelengths, n is the refractive index of the immersion media and NA is the numerical aperture of the objective lens [8].

In a confocal system using visible wavelengths for excitation, the diffraction limited resolution of the imaging system is: $\Delta \mathrm{r} \approx 200\,\mathrm{nm}$ and $\Delta \mathrm{z} \approx 600\,\mathrm{nm}$. With the advancements in the design of objective lenses, chromatic aberration can be removed as a source of aberration limiting image resolution. This leaves optical misalignment and the summation of the optical tolerances across all optical components as the primary source of residual aberration (e.g. astigmatism from dichroic mirrors) [59].

We have chosen to use the confocal imaging system for several reasons:

- The optical sectioning ability allows the microscope to be used for 3D imaging of biological samples labelled with optical fluorophores. It would not be possible to extract the same level of detail using a wide-field imaging system,

without implementing other technologies, such as: Light sheet microscopy [60], spinning disk [61] or computational super-resolution techniques [11].

- The single point detection scheme in confocal imaging is compatible with well documented ODMR experimental protocols [36, 51, 52, 53]. This is important as the research group had not attempted ODMR experiments at the time of my project starting. Using a system that had been shown to be compatible with the ODMR measurement protocol simplified the development of the initial ODMR protocols.

2.2 Building a Microscope for Biological Sensing

A schematic of the bespoke adaptive optics enhanced confocal microscope system used in this work can be seen in figure 2.1. The microscope was designed and built with the imaging of nanodiamonds embedded within biological material as its primary purpose. The microscope is equipped with three excitation lasers with wavelengths of 488 nm, 532 nm and 640nm, these are commonly used wavelengths for imaging traditional fluorophores used in biological imaging, such as: GFP [62], fluorescent dyes [63, 64] and quantum dots [65]. The three excitation lasers are all co-aligned in the common path of the microscope allowing for multi-wavelength imaging of cells.

In the bottom left hand corner of the figure 2.1, we can see the coupling of the three excitation lasers into the common path of the microscope system. The power of the excitation lasers coupled into the microscope system is controlled by either: polarisation-based attenuation (Green), a variable neutral density filter (Blue) or by adjusting the alignment of the fibre coupling pinhole relative to the

optical axis (Red). The excitation lasers are coupled into the common path of the microscope via single mode optical fibres. The lasers are then guided into the common path of the microscope using a series of turning mirrors and dichroic mirrors. Once in the common path, a 20 times beam expander is used to expand the excitation beams to overfill the aperture of the deformable mirror. By overfilling the DM aperture, we ensure that we are able to use the full area of the mirror for aberration correction, allowing for higher order corrections to be made. It also allows us to ensure that we are filling the back-aperture of the microscope, and therefore utilising the full numerical aperture (NA) of the objective.

The excitation laser is centred on a fast-steering mirror (FSM) used to scan the laser focal spot across the sample. The total scan range available from the FSM is 40µm by 40µm across the sample. It is theoretically possible, using the FSM, to achieve a scan area four times this size; however, the functional limits of the FSM mean that it over-heated/stopped responding when when larger scan areas were trialled. The excitation laser is then focused down onto the sample through an 60x, 1.35 NA, infinity corrected, oil immersion objective (Olympus UPLSAPO60XO). Samples were brought into the focus of the objective by a movable sample stage and can also be illuminated in transmission mode by a high powered Thorlabs white-light LED (SOLIS-3C). Light from the sample is passed back through the common path of the microscope, with 10% of the light being picked off in the diagnostic channel via the 90:10 beam splitter. Within the diagnostic channel, we have a wide-field imaging arm, the Shack-Hartmann wavefront sensor (not used in this work) and a single pixel detection port. The single pixel detected in the diagnostic channel was aligned in such a way as to have a collection volume of $5\,\mu m \times 5\,\mu m$. This channel was co-aligned with the confocal imaging channel, and was used to check to see if there were any aberrations in the optical system between the deformable mirror and the confocal pinhole which

could affect the quality of imaging from the microscope.

The wide-field imaging arm was used to bring the samples into the focus of the objective. A Thorlabs DDC camera was used to monitor the back-lit sample as the sample stage moved into position. The imaging plane of the camera was co-aligned with the focus of both the confocal and wide-field detection channels, so when the sample came into focus on the wide-field camera, it was in (or close to) focus for the whole of the microscope system. During confocal imaging, the fluorescent light passes through the common path of the microscope and is imaged by single photon avalanche detector (SPAD) operating in Geiger mode. Depending on the sample under study the fluorescent signal is detected either through "Channel 1", used for nanodiamond imaging, or the green fluorescent protein (GFP) detection channel. The microscope is due to be upgraded to allow for STED imaging in the near future. The optical path has been designed and the components are on the table however due to time constraints has yet to be implemented.

2.3 Adaptive Optics

Optical aberrations have been the bane of deep tissue biological imaging for a number of years [66, 67]. In confocal microscopy the introduction of aberrations from microscope misalignment, or more commonly refractive index mismatch between the sample and the objective can degrade image quality [2, 68]. As a research group, we define "deep tissue imaging" as: the depth of imaging in which the sample induced aberration reduces the detected imaging signal to 80% of that which would be achieved in aberration free environment. Deep tissue imaging, as we have defined it, is sample dependent. The metric used to define the quality of

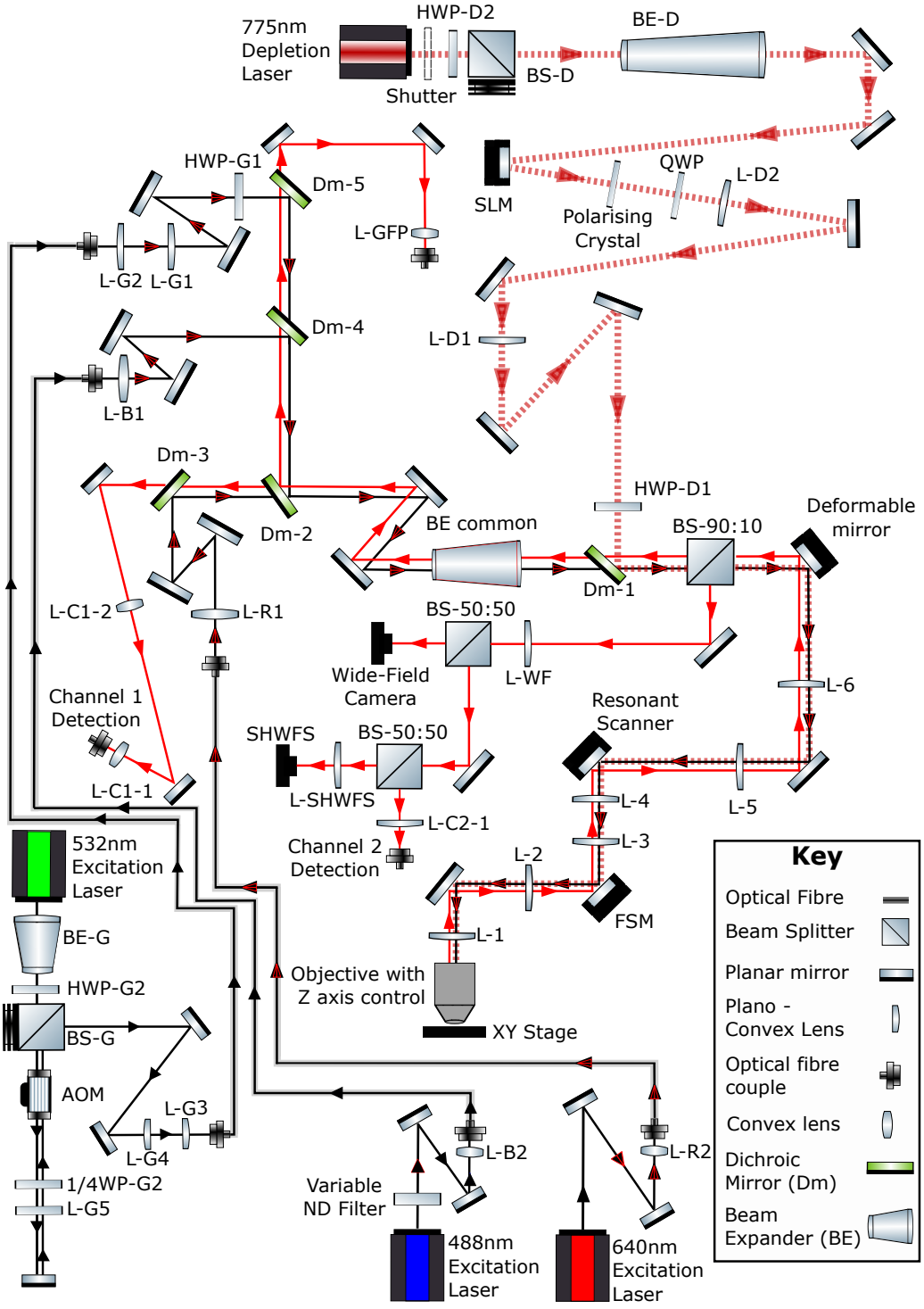

Figure 2.1: A schematic of the full AO STED microscope system. At the time of writing, the depletion arm is not yet operational.

imaging through optically complex samples is called the Strehl ratio, and will be defined in greater detail later in this chapter (section 2.7.1).

The point spread function (PSF) of a microscope is the diffraction pattern of the light observed from a point-like emitter. In microscopy, this a point-like emitter generally a fluorescent object that is smaller than the resolution limit of the microscope configuration used, e.g: quantum dots, nanodiamonds. [68] When performing deep tissue imaging on a biological sample, the wavefront of the excitation laser can experience phase changes due to the change in the optical path length the light experiences as it passes through various refractive index changes within the biological material [69]. This is also true for any emission from an excited fluorophore being imaged, resulting in a distortion of the microscope PSF [68]. In confocal microscopy, degradation of the microscope focal spot affects the optical sectioning capabilities of a confocal system, which, in turn, the reduces the lateral and axial resolution of the microscope, effecting the quality of the image produced [2]. Deformation of the focal spot of the confocal system also affects the signal-to-noise ratio of the image as the photon flux from the excitation laser is spread over a larger area [69]. This results in more out-of-plane excitation of fluorphores in the specimen, the light from which is rejected by the optical pinholes. The reduction in the signal to noise of the image due to aberrations can be compensated for by an increase in applied laser power; however, this runs the risk of photo-toxic effects changing the behaviour of the biological system under study [70].

A further problem when imaging biological samples is that the magnitude of induced aberrations can vary significantly between cells within the same sample and even vary across the structure of a single cell [71, 72]. Therefore it is difficult to mitigate for sample aberrations in conventional microscope design given that

the aberrations are liable to change, potentially over time scales as short as tens of seconds for live-cell imaging [69].

One solution for correcting for the aberrations induced when imaging through optically complex material is to use adaptive optics [2]. The concept for adaptive optics (AO) was first introduced in astronomy for correcting for aberrations induced by atmospheric turbulence by Babcock *et al* [73]. In this paper, Babcock discussed the use of actuators to control the shape of a reflective membrane to correct for the effects of a turbulent atmosphere when imaging stars. It was just over thirty years later Hardy *et al* reported the first use of a deformable mirror to actively compensate, in real time, for image aberration induced by atmospheric turbulence [74]. This technology has since been utilised in the early 2000's by Booth *et al* to show that aberration correction can be carried out in a confocal microscope using a deformable mirror [2]. The group developed a method of measuring the magnitude of an aberrating mode in a biological sample and used a deformable mirror to remove the aberration from the image. The results of the aberration correction are shown in the paper (reproduced in figure 2.2) and the sharpness and level of observable detail in the corrected image are highlighted as the aberrations are corrected for [2]. The aberration correction applied when using a deformable mirror is the result of changes in phase across the incident beam wavefront only, it does not correct for chromatic aberration, polarisation mixing or light lost due to scattering [75].

Aberration modes such as Coma and Astigmatism are well modelled by the Zernike polynomials [76]. The Zernike polynomials are described by the following equations:

$$Z_i(\rho,\theta) = \begin{cases} \sqrt{2(n+1)}\ R_n^m(\rho)\ G^m(\theta) & m \neq 0 \\ R_n^0(\rho) & m = 0 \end{cases} \tag{2.5}$$

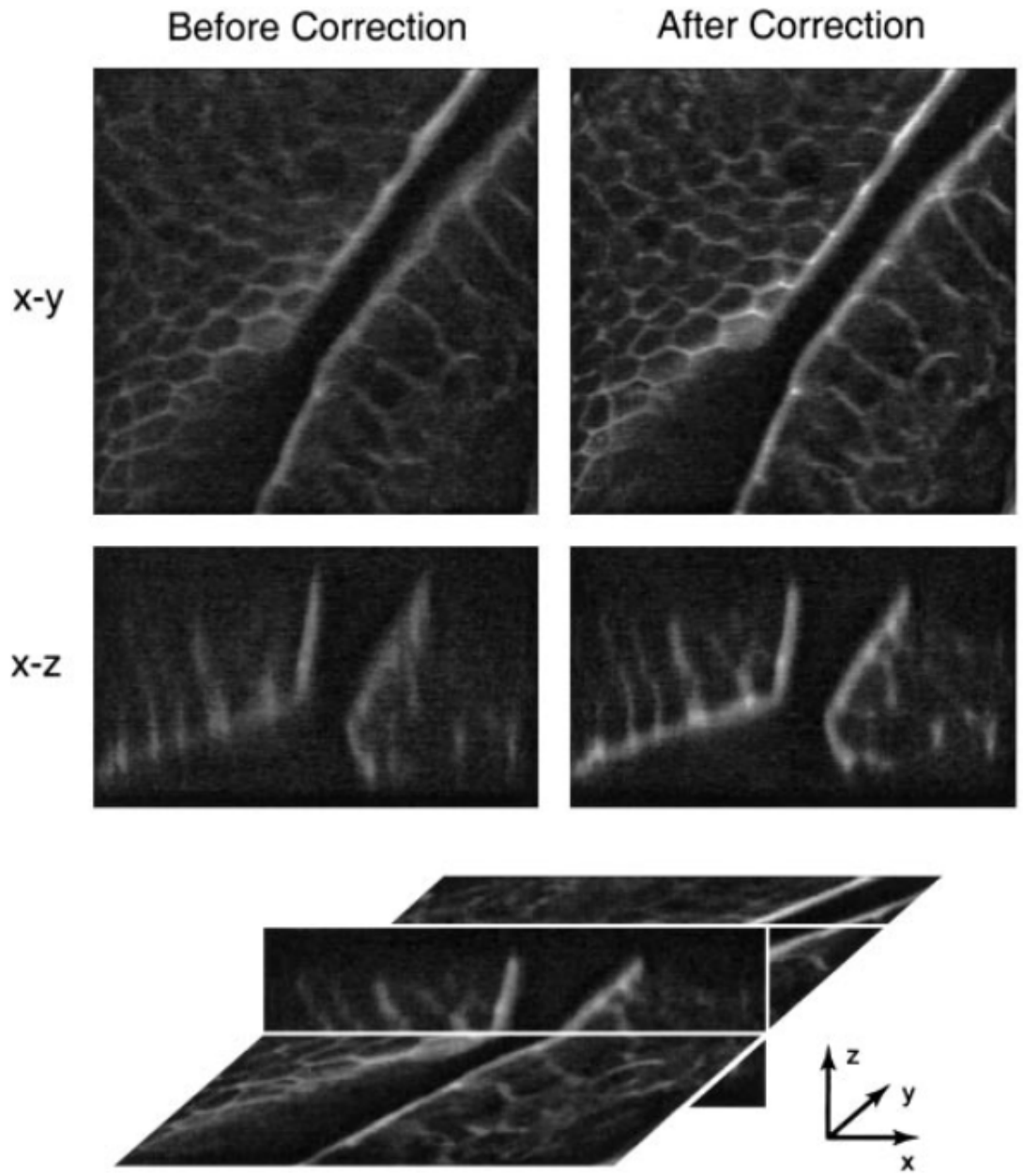

Figure 2.2: An example of confocal images of a section of mouse intestine that has been labelled with a fluorescent probe, both with and without aberration correction applied. The application of aberration correction has resulted in greater image contrast and produced a sharper imaging than before the correction was applied. This figure is from the a paper by Booth *et al*, [2]. Copyright (2002) National Academy of Science. U.S.A.

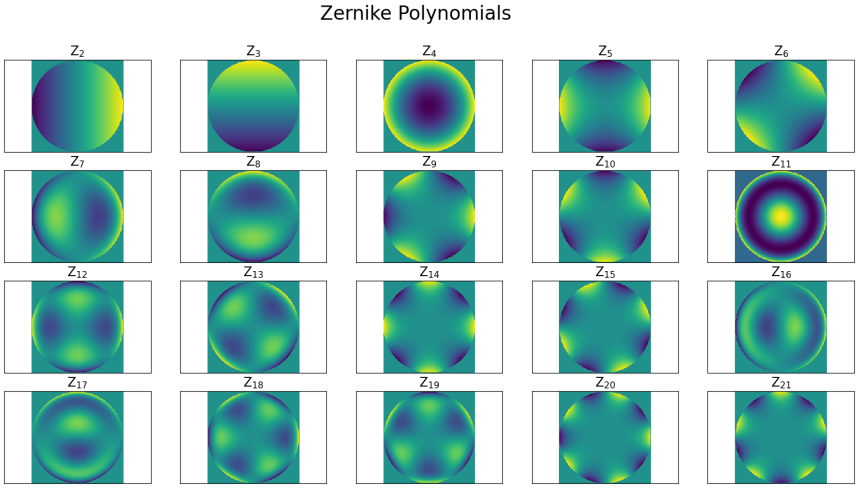

Figure 2.3: A model of the Zernike modes 2 - 21 within a unit circle. Modes Z_5 and Z_6 are the primary astigmatism modes, Z_7 and Z_8 represent the modes corresponding to coma, and Z_{11} represents primary spherical aberration. Script used for this figure provided by Dr Brian Patton.

In which, $R_n^m(\rho)$ is a function describing the radial component of the mode (radial distance = ρ). The value of ρ is bound between 0 and 1, inclusive. $G^m(\theta)$ is a function dependent on the azimuthal component (θ). m and n are non-negative integers [77]. These functions are defined by the following:

$$R_n^m(\rho) = \sum_{k=0}^{\frac{n-m}{2}} \frac{(-1)^k (n-k)!}{k!\left(\frac{n+m}{2}-k\right)!\left(\frac{n-m}{2}-k\right)!} \rho^{n-2k} \tag{2.6}$$

$$G^m(\theta) = \begin{cases} \sin(m\theta) & i \; is \; odd \\ \cos(m\theta) & i \; is \; even \end{cases} \tag{2.7}$$

A computational model of Zernike modes 2 - 21 can be seen in figure 2.3. Mode 1 has been ignored in this figure as the phase across the unitary pupil is constant [77].

Any arbitrary wavefront can be described by a series summation of weighted

normalised Zernike modes across a unit circle [78]. In aberration correction, the summation of these terms can be used to describe the optical aberrations which can be induced when imaging through optically complex material [78]. This is significant when trying to implement aberration correction using adaptive optics as the Zernike modes provide an orthogonal basis to describe the aberration modes [78].

2.4 Adaptive Optics in Our System

In this work, we make use of a deformable mirror (DM) for aberration correction. The DM used within our microscope system is a Mirao 52-e deformable mirror. The deformable mirror is made from a continuous flexible reflective membrane whose shape is controlled by 52 actuators corresponding to 52 degrees of freedom for correction, resulting in a maximum of 52 possible control modes for any given basis. The maximum stroke of these actuators is $\pm 25\,\mu m$, however, the total available stroke for correction may be limited depending on the positioning of the surrounding actuators. I worked alongside both Dr Brian Patton and Dr Graeme Johnstone to install the Mirao mirror within the microscope system following the failure of a previous deformable mirror used in the system. The DM was positioned in the common path of the microscope and imaged to the back aperture of the microscope objective (see figure 2.1). This allowed for aberration correction of both the excitation and detection arms of the microscope and optimal performance from the DM [69].

2.5 Aberration Correction using a Deformable Mirror

To correct for aberration in an optical system using a deformable mirror, one needs to be able to monitor the effect of any changes in mirror shape to the image and reliably control the shape of the mirror[71].

2.5.1 Monitoring Aberration Correction

There are two reported modalities for measuring the aberration induced when imaging in biological material: sensor or sensorless measurement. Using a wavefront sensor, such as a Shack-Hartmann sensor, is one way of directly measuring aberration in an imaging system using a point source within biological material, the principles of this measurement technique are explained in [79]. This will not be explored further in this thesis as the Shack-Hartmann (SH) sensor in our system was never used for adaptive correction of sample induced aberrations throughout this project.

Throughout this project, we have made use of a sensorless aberration correction methodology. The principle of the sensorless measurement regime used throughout this project has been based upon the maximisation of the fluorescent signal observed from point-like nanodiamond emitters over a 2D lateral scan around the diamond of interest [71]. The basic principle for the correction technique is shown in figure 2.4. One of the aberrations (Zernike modes) is selected for correction, eg: Vertical Astigmatism (Zernike mode 5 in figure 2.3), the magnitude of the applied mode is then scanned in discrete steps between an upper and lower bound chosen by the user. For each change in the shape of the deformable mirror, a 2D scan is recorded to assess the affect that the applied aberration has on the image quality using a chosen quality metric. The quality metric is chosen so that the applied aberration will tend towards a maximum value as the

image correction improves. A quadratic or Gaussian lineshape can then be fitted to the quality metric values plotted against aberration magnitude to extract the optimum amount of the selected Zernike mode to achieve the maximum image quality [3]. The quality metrics that have been used throughout this study are:

- **Sum of intensities:** This metric is used to identify the aberration mode that maximised the overall sum of intensities recorded for each pixel in the image.
- **Sum of intensities squared:** Each pixel value in the image is squared and then summed together. The optimisation routine then looks to maximise this value for each of the applied aberration correction modes.
- **10% cut-off:** This metric uses the sum of the top 10% of pixel values in an image to optimise the image quality.

This process is then applied to each of the aberration correction modes selected to to improve image quality. One of the drawbacks from this correction technique is that it can only be applied to one aberration mode at a time, so can be quite time consuming depending on the number of aberration modes chosen for correction.

The process of sensorless aberration is slower overall than using a Shack-Hartmann sensor for the implementation of adaptive optics. In our system, however, it makes more sense to implement sensorless AO control as the detector used for the measurement is the same SPAD that is used for imaging and ODMR experiments. Therefore there is no need to syphon off additional fluorescent signal from the main detection path in order to perform aberration correction, as would be the case if we were to use a Shack-Hartmann sensor in the microscope system. In a feasibility study for the equipment that we had to hand, we tried to monitor the aberration in the microscope system using a nanodiamond sample. We found that the 10% of detected signal from the nanodiamonds that is directed towards the diagnostic (wide-field) arm of the microscope was not enough for the

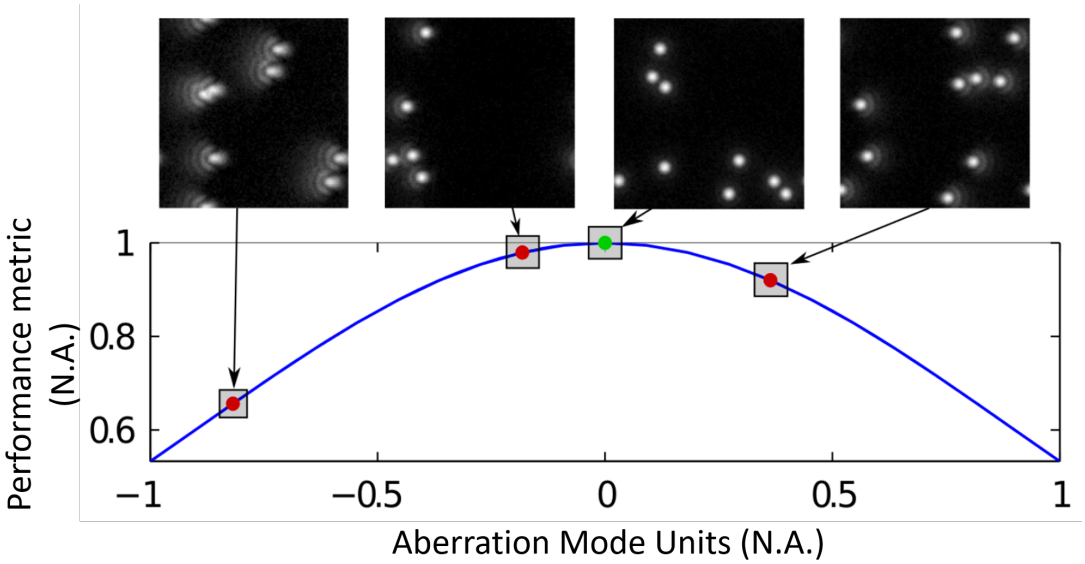

Figure 2.4: A representation of the sensorless aberration correction technique used to improve the image quality by removing the effects of sample induced aberration. This figure is taken from a 2015 paper from Burke *et al.* Reprinted with permission from [3] © The Optical Society

Shack-Hartmann sensor to be used to detect aberration in the system. This was a measurement performed during the re-alignment of the microscope following the installation of the Mirao deformable mirror using a nanodimaond sample. No further investigation of this result was performed as this was beyond the scope of the research project. We suggest that with a more sensitive SH sensor in the system, or a brighter fluorophore, it might be possible to implement aberration correction using a sensor-based correction system, taking advantage of the fact that the emission from fluorescent nanodiamonds can be considered to occur from a sparse set of sub-diffraction sized particles [79].

2.5.2 DM Calibration

As described above, in order to reliably perform aberration correction using a deformable mirror, one needs to determine the control matrix for the device [71]. The control matrix is a 2D matrix that represent the control signals that are required to generate known deformations to the shape of the mirror. The control matrix can be thought of as containing the description of the Zernike mode shape of the mirror in one dimension, and the control signals required to generate the mode shape on the mirror surface on the other [80]. To calculate the control matrix for our deformable mirror, Dr. Patton, Dr. Johnstone and I used the method and software described by Antonello *et al* in [81]. To implement this method we first had to position the deformable mirror in the correct place in the optical path of the microscope. Tracing back from the objective, we had to make sure that the deformable mirror was in the focal plane of the 4F system of lenses 5 and 6 in figure 2.1. This was to make sure that any beam scanning performed by the resonant scanner did not result in a movement of the beam across the deformable membrane. The resonant scanner was in turn positioned in the focal plane of the 4F system of lenses 3 and 4 to ensure that any movement of the fast

steering mirror (FSM) did not result in a misalignment of the microscope. Once the DM's position on the table was found and the microscope system aligned, we were able to start the process of calibrating the DM.

For calibration, Dr. Patton and I build an interferometer that now sits on the optical table permanently (with the exception of 1 turning mirror). The interferometer design was adapted from the design shown in [81] to be compatible with our experimental set-up. During the construction of the interferometer, we made use of an home built autocollimator. This was extremely useful when locating the correct lens positions to ensure that the light remained collimated when travailing through the interferometer. We recommend the following video as a first introduction to the autocollimator [82]. This is the most useful source that we have found for describing the function of the autocollimator and is a comprehensive guide to the construction of the alignment tool.

Following the construction of the interferometer, we then used the software developed by Antonello *et al* to calibrate the DM's control matrix. This was done by analysing the interferometric pattern produced when the voltage applied (control signal) to a single actuator of the DM was changed. This introduced a phase change to the wavefront of the calibration laser, which was then extracted from the interferogram [81]. In this process, the magnitude of the control signal applied to each actuator moved the actuator across 10% of its total travel range in 5 discrete steps. The phase change for each actuator movement is extracted by Fourier-based fringe analysis, this extracts the phase change introduced. The wrapped phase is then calculated (Phase changes bound between either: $-\pi$ and π or 0 to 2π) to extract a vector containing the coefficients of each of the control modes in the basis needed to recreate the phase change from the tested actuator. If we use singular value decomposition to analyse the results of the evaluation of

the interferometric data, one can determine the shapes the mirror can reproduce with high fidelity for a given control input [81]. To compute the control matrix for the DM in terms of the shapes of the Zernike polynomials, one needs to consider the phase change produced by the DM in terms of a linear summation of Zernike modes. Through this process, we are able to create a matrix H which has the dimensions ($N_z \times N_a$) in which N_a is the number of actuators used to control the DM, and N_z is the number of Zernike modes used to model the shape of the mirror, this is chosen so that $N_z > N_a$, to ensure the influence function (mirror shape change as a function of input voltage) is well described by the number of modes used [81]. The control matrix (C) used to generate Zernike modes for a given input signal across many actuators can be found from the pseudo-inverse of the matrix H [81].

$$\mathbf{u} = \hat{C}\mathbf{z} \tag{2.8}$$

$$\begin{pmatrix} u_1 \\ u_2 \\ \vdots \\ u_{N_a} \end{pmatrix} = \begin{pmatrix} C_{1,1} & ... & C_{1,N_a} \\ C_{2,1} & ... & C_{2,N_a} \\ \vdots & \ddots & \vdots \\ C_{N_z,1} & ... & C_{N_z,N_a} \end{pmatrix} \begin{pmatrix} z_1 \\ z_2 \\ \vdots \\ z_{N_z} \end{pmatrix} \tag{2.9}$$

Through this process, we were able to generate a control matrix for the Mirao DM that we were using for aberration correction in our system. The magnitude for a given Zernike mode generated by the DM is given as a unit, which is defined as the amplitude of an applied Zernike mode that would create a root-mean-square (RMS) phase change across the surface of the mirror of 1 radian [80].

2.6 Aberration Correction in Action

To test the effectiveness of the DM for aberration correction, I wanted to directly image the point spread function of the microscope. The PSF of a microscope is the image formed from a fluorescent point-like emitter. To image the PSF of the confocal microscope, I therefore needed to image an optical probe that was smaller than the diffraction limit of the microscope. From equations 2.3 and 2.4, we recover than the diffraction limited spot would be (207 nm, 207 nm, 725 nm) (in the Cartesian coordinate system, with $\Delta R = \Delta x = \Delta y$, for a circular focal spot.) assuming a mean fluorescent emission wavelength of 700 nm [8]. I made use of a 70 nm diamond sample as an optical fluorophore for direct imaging of the confocal microscope PSF.

In figure 2.5, the improvement to the quality of the PSF can be seen as a result of the influence of the deformable mirror. Figure 2.5a shows the PSF of the microscope without any aberration correction. The scan range was (3 µm, 3 µm, 10 µm) in the lateral and axial directions respectively. The voxel size for these images was (100 nm, 100 nm, 200 nm) and was recorded with a 1.5 ms dwell time per pixel. To allow for direct comparison with the corrected image, the PSF measurement has been cropped to have the same scan range dimensions as figure 2.5b. No additional information was lost in this process. The coma that was present in the confocal system can most clearly be seen in the x-z scan in the bottom right hand side of the figure . Fitting a Gaussian curve to each of these plots and measuring the FWHM of the curve, it is possible to determine the resolution of the microscope from these images. From this analysis I obtained a resolution of: (270nm, 270nm, 1010nm). After applying the aberration correction protocol outlined in 2.5 we can see the corrected PSF in figure 2.5b. The coma in the image has been all but completely removed from the image, this allowed

me to reduce the size of the scan use to record this PSF measurement to (3 µm, 3 µm, 5 µm) with a voxel size of (100 nm, 100 nm, 100 nm) and a pixel dwell time of 1.5 ms. If we look at the scale bar for these images, we also see that the maximum fluorescent signal from the nanodiamond has increased by almost double with the aberration correction. Using the Gaussian fitting algorithm on the corrected PSF, we obtain a resolution of (210nm, 270nm, 760nm). As a result of the correction, there has been a 25% improvement in the axial resolution of the microscope. There is also a slight improvement to the lateral resolution in one direction (x) as a result of removing the coma in the system. The lateral asymmetry in the corrected PSF is likely the result of some residual coma in the system. This correction routine was used to determine the DM "flat" mirror shape following a realignment of the microscope. The first and second order coma aberrations were corrected for in this image. It is possible that the residual coma in the system is the result of third order effects, which were not corrected for. The significant improvement of the shape of the PSF shown here was enough not to need to perform third order corrections.

Figure 2.5 shows the power of adaptive optics for improving the imaging quality of a confocal microscope when imaging through biological material likely to induce multiple aberration modes. The improvement of the PFS recorded came from the correction of aberration modes 5 - 11 (Primary astigmatism, primary coma, primary trefoil and primary spherical). In addition, I also performed an optimisation for the second order astigmatism, coma and spherical aberrations.

2.7 Microscope Performance

2.7.1 Strehl Ratio

As mentioned previously, it is useful to be able to quantify the improvement in image quality as adaptive optics are used to correct for sample induced aber-

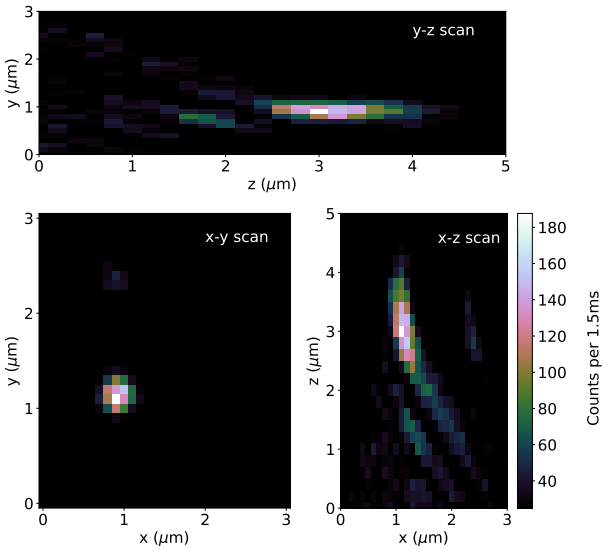

(a)

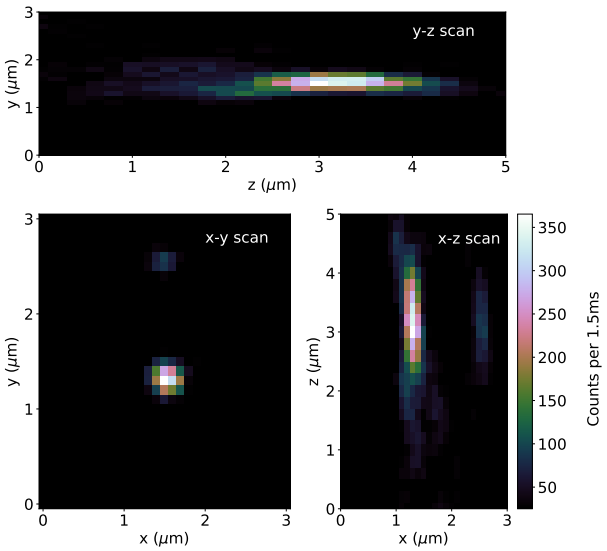

(b)

Figure 2.5: A comparison of a PSF measurement recorded from a point-like nanodiamond emitter mounted in immersion oil, both prior to aberration correction via the DM (2.5a) and after (2.5b).

rations. One metric that can be used to describe this improvement in image quality is the Strehl ratio [83]. There are many definitions and ways to calculate the Strehl ratio of an image [84]. With our research group, we focus on just two of the methods for calculation of the image quality metric. The first is just a straight comparison between the the image intensity recorded from the centre of the microscope PSF measurement both with and without aberration correction applied:

$$S = \frac{I_{aberrated}}{I_{corrected}} \tag{2.10}$$

This method of calculating the Strehl ratio assumes that the corrected image is completely free from aberration. The secondary method that we make use of for calculating the Strehl ratio of an image is to use the following formula:

$$S = \exp\{-\sigma^2\} \tag{2.11}$$

In which σ is the root-mean-squared wavefront phase error corrected for using the deformable mirror [49]. This value can be calculated as the root-mean-squared-sum of the magnitudes of the Zernike modes used for correction. The Zernike polynomials form an orthogonal basis for correction, with each mode normalised so that 1 unit of aberration correction is proportional to a unitary change of phase across the surface of the DM [81]. Assuming that the aberration correction removes all aberration from the image, the calculation of the Strehl ratio using these two calculations should be equivalent [49].

2.7.2 Noise Limit of the Microscope

One of the most important characteristics of our microscope that we needed to characterise is how the photon detection error scales with the number of photons counted. The optically detected magnetic resonance (ODMR) measurements we

want to perform rely on detecting the change in the fluorescence intensity from the defects within the diamond as the frequency of an applied microwave field changes (see section 3.1.1). Therefore, to track the sensitivity of the ODMR measurement, we need to know how the signal to noise ratio of the detection arm of the microscope scales with increased photon flux. In an idealised system, we would be shot-noise limited [85]. The shot-noise limit is the fundamental limit of sensitivity that can be obtained in photo-detection and arises from the statistical nature of photon emission/detection. In a shot noise limited system, the associated noise in a photon-flux measurement is proportional to the square-root of the number of photons detected (N) [86],

$$\delta I = \sqrt{N}. \tag{2.12}$$

To test if our system was shot-noise limited, I conducted two different experiments. In the first set of experiments, I monitored how the fluorescence intensity from a 40 nm diamond crystal changed as the laser power was increased from 5.5 µW to 710 µW. The integration time for the measurements was 10 ms and 13100 data points recorded per measurement. The results of the measurement can be seen in figure 2.6. A curve with the equation;

$$y = A\sqrt{x} + C, \tag{2.13}$$

was fitted to the data, with A and C being scalar values that were used to find the best fitting to the data. We are able to model the measurement error (standard deviation in data points per measurement per applied laser power) using equation 2.13. The results of the curve fitting produced values of $A = 1.88$ and $C = -3.5$. In the ideal case, we would expect the value of A to be 1, and the noise in the system to be modelled accurately by just the square root curve.

In an attempt to find an explanation for this pre-factor to the square-root

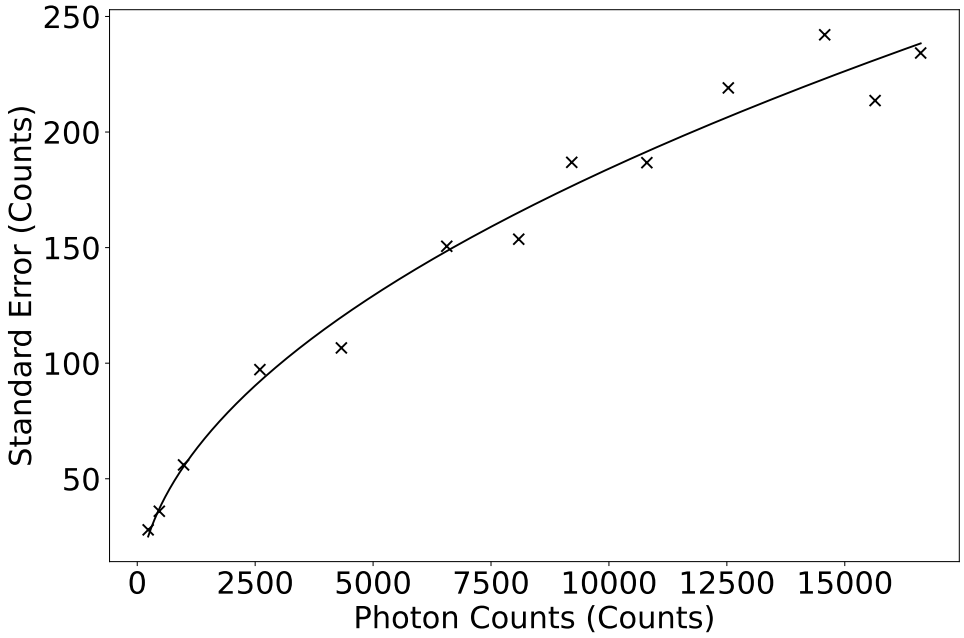

Figure 2.6: Shot noise limit measurement, data recorded from the fluorescence intensity of a nanodiamond as the applied laser power was increased. The error was calculated as the standard deviation of the number of photon counts recorded from multiple repeats performed for each applied laser power.

relation, I performed a second experiment. In this experiment, the fluorescence from a single nanodiamond was recorded, as before, however, the laser power remained fixed, while the photon integration time was varied from 1 ms up to 10 s, this allowed us to test the response of the photo-detectors when dealing with high photon-flux without approaching the saturation limit and risking damage to the detector. The results of this measurement can be seen in figure 2.7. In this graph, the mean number of counts per measurement and the associated measurement error are both plotted on a logarithmic scale. The plot has been split into three sections to highlight that the relationship between the measurement noise and the total number of counts recorded. It appears that as the photon integration time is increased, the measurement error also increases. In the region with the fewest photons recorded per measurement, the pre-factor was found to be $A = 1.76$. These measurements were recorded with a photon integration time between 1 ms and 10 ms. In the mid section, the photon integration time was varied from 20 ms to 200 ms and results in a gradient of $A = 2.6$. In the final section of the graph, the integration time is varied between 500 ms and 10 s and the gradient increases to $A = 28$. When the integration time is short, the pre-factor is close to the shot-noise limit approximation value of $A = 1$. As the integration time is increased, the pre-factor also increases. This suggests that we have some low frequency noise (> 10 Hz) in the system that can be considered as quasi-static when using short dwell times (1 ms - 10 ms). When the dwell time exceeds 100 ms, the noise in the system becomes incorporated in the number of photons recorded, degrading the photon detection error beyond the shot-noise limit of the microscope. To lend some support to this theory, I identified the effect of electro-magnetic noise from the building infrastructure that was coupling into the microscope through the objective axial control in the range of 0.5 Hz - 10 Hz. The noise observed in our measurement system is discussed later in this work (section 3.5.2). Other potential sources of noise that could be affecting the signal to noise ratio are:

- Thermal instability of the AOM.
- Laser power instability.
- Room temperature instability.
- Sample drift.

This data set was recorded for experiments discussed later in section 4.8.1. The aim of the experiment was to keep the length of photon detection constant while varying the dwell time and the number of repeats. As a result, as the dwell time decreases, the number of repeats increases. Therefore, we cannot say for certain that the increase in measurement error for longer dwell time is only down to the incorporation of low frequency noise that is averaged out for shorter dwell time measurements. It might be that not enough data-points were recorded for the long integration time measurements to accurately determine the photon-detection noise.

2.7.3 Common Laser Path Power Transmission

An important characteristic of our confocal microscope that we wanted to understand is the laser power transmission through the optical system from the laser to the back-focal plane (BFP) of the objective. With the transmission co-efficient defined, we are able to determine the laser power at the sample by measuring the laser power at a more convenient position in the microscope (eg: the exit of the fibre coupling into the common path of the microscope). The laser power transmission was measured using a Thorlabs PM400, with the laser power being set using the polarisation attenuation optics positioned at the laser output, and the laser power was then measured at various points throughout the microscope system.

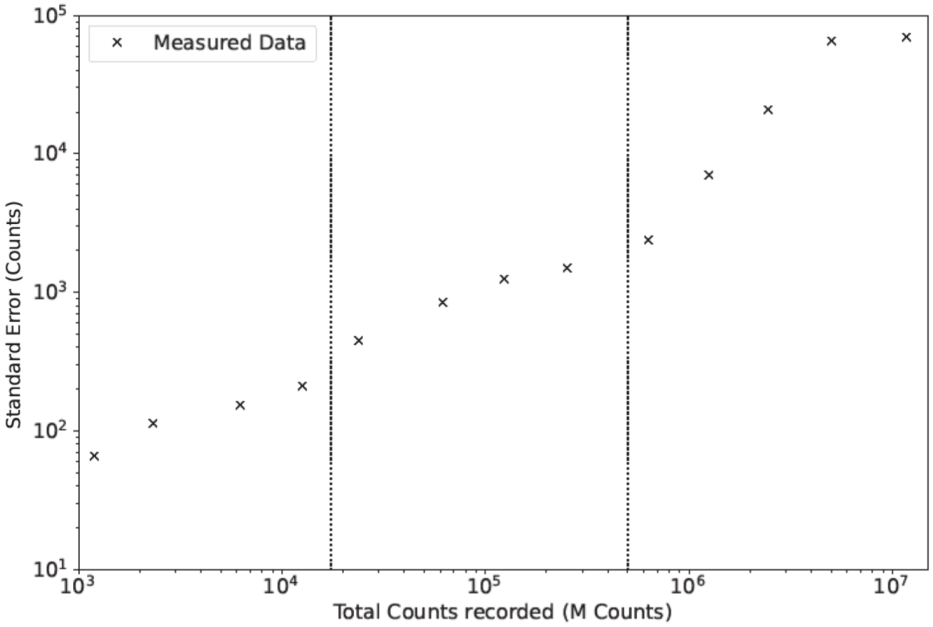

Figure 2.7: Shot noise limit measurement from increasing measurement dwell times.

I was able to achieve a 65% power transmission from the laser output through the double pass of the AOM and into the single mode fibre used to couple the laser into the common path of the microscope. The majority of the light lost in this section of the microscope comes from the double pass of the AOM. For each pass of the AOM, approximately 85% of the light is transmitted into the first order diffraction and allowed to transmit through the microscope system. This is then compounded by a 90% coupling efficiency of light into the single mode fibre. With the combination of these transmission efficiencies in the system, 65% of the laser power is transmitted from the excitation laser to the common path of the microscope.

To measure the efficiency of the laser power transmitted to the back focal plane of the objective, the laser power was monitored from the output of the fibre coupling the green laser into the common path of the microscope, and at the back focal plane of the objective. For this measurement, I varied the laser power through the microscope, monitoring the laser power at the fibre output and the back-focal plane of the microscope. The recorded laser power when then plotted against one another and a linear fit applied to the data to determine the percentage of laser power from the fibre output that is delivered to the back focal plane of the microscope. The results of this investigation can be seen in figure 2.8. A linear fit with a gradient of 0.249 ± 0.003 is used to model the trend of laser power transmission through the common path microscope. The results of this measurement show that roughly a quarter of the laser power at the output of the fibre used to couple the 532 nm laser into the common path of the microscope is transmitted to the back-focal plane of the objective.

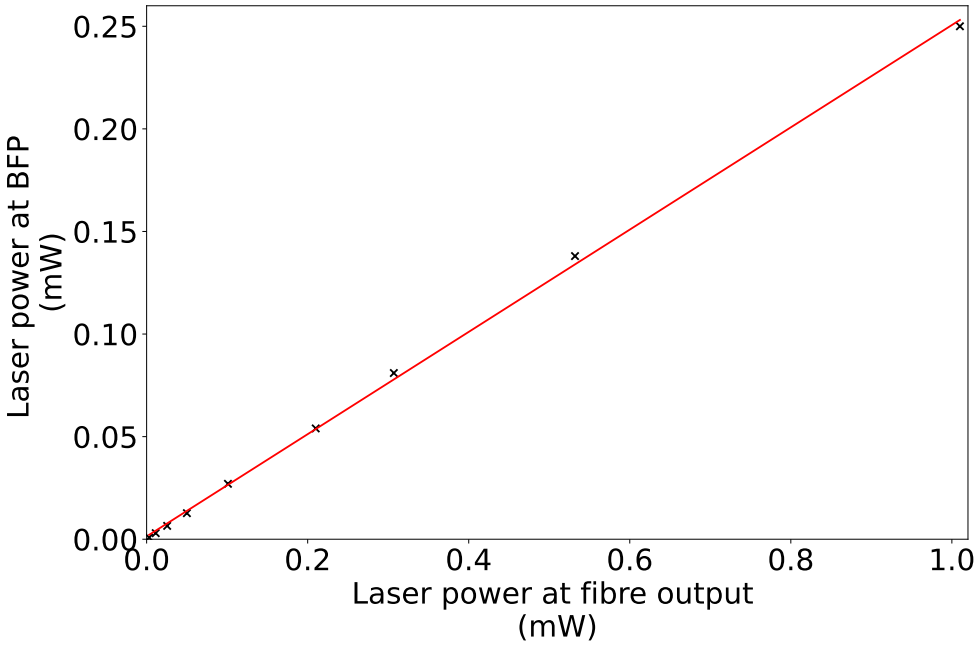

Figure 2.8: A graph showing the efficiency of laser power transmitted through the microscope system. The gradient of the linear fitting is 0.249 ± 0.003.

2.8 Summary

In this chapter of the thesis, I have introduced the bespoke, adaptive optics enhanced confocal microscope system used throughout this work. I have described the optical set-up of the imaging system and the key components of the microscope. I have also introduced the concept of aberration correction for biological imaging, both the core concepts and how it is implemented in our imaging system. This also includes a demonstration of the aberration correction used in our system and the effect this has on the PSF and therefore imaging capabilities of our confocal microscope.

In addition to the work on aberration correction, I have also included the calibration and implementation of the acousto-optical modulator. In this work I have investigated the rise and extinction time of the AOM for laser power mod-

ulation when used in the single and double pass configurations. The results of these measurements showed that the double pass of the AOM provided a much improved square wave laser power gating and reduced the extinction time by just over a third compared to the single pass iteration. The improved laser gating does come at a cost for the total laser power that can be transmitted from the laser source to the microscope objective; however due to the future aim of pulsed laser experiments being conducted using this system, it was decided that the loss in laser power was acceptable given the increase in the quality of laser gating.
I have also included a discussion on the work done to calibrate the properties of a resonant scanner device that is to be used to increase the imaging speed of our system. Much of the work conducted was to try and determine the relationship between the applied voltage used to drive the resonant scanner and the scan angle of the mirror. This work was used to then determine the total scan-range of the resonant scanner once in place on the microscope. Using a reflective grid of $10\,\mu m \times 10\,\mu m$ and the wide-field imaging arm, I was able to determine the relationship between the one dimensional scanning provided by the resonant scanner and the applied voltage. This data can be used in the future to control the scan range of the resonant scanner during imaging.

Finally, in this chapter I have discussed the evaluation of the performance of the microscope in a number of areas. Such areas of investigation were:

- **Signal to Noise ratio:** Here I evaluated the associated error in the photon counting. In a shot noise limited system, we would expect the standard deviation of multiple measurements recording a constant flux over a controlled time period to be equal to $\sqrt{N}$ [85]. In our microscope system, we require a multiplication factor in order to accurately fit the data using a square root relation. We also found that the multiplication factor observed in this work varied as the photon integration time increased. As a result,

we need to carefully consider what noise regime the microscope is operating in during any experimental analysis.

- **Laser power transmission:** In this measurement the laser power transmission efficiency was determined through the common path of the microscope for the 532 nm laser. The efficiency of the transmitted power was $24.9\,\% \pm 0.3\,\%$ from the output of the 532 nm single mode fibre input to the back-focal plane of the objective.

Chapter 3

ODMR Development

In this chapter of the thesis I am going to discuss the development of the optically detected magnetic resonance (ODMR) spectroscopy protocol within our experimental setup. Initially I will discuss the nitrogen-vacancy (NV) centre in diamond, its electronic and spin energy level structure and how this is exploited in ODMR experiments for magnetic field and temperature sensing. I will go on to explain the development of an ODMR measurement protocol. This includes the characterisation and performance assessment of a double split ring resonator (DSRR) used for microwave delivery [87], discussing the relative merits and demerits of the microwave delivery system in our setup. I will compare this to a coplanar waveguide microwave delivery system and the considerations that need to be taken into account when developing an ODMR protocol for our experimental setup. The testing of this experimental protocol for temperature sensing using an Oko-Labs H-301 temperature stage will be discussed. Finally, I show the development of our own ODMR with referencing protocol to mitigate the effects of sample drift on ODMR measurements.

3.1 The Nitrogen-Vacancy Defect

For the benefit of the reader not already familiar with the nitrogen-vacancy (NV) defect in diamond, it is a crystallographic defect in the structure of diamond that is formed when a vacancy (missing carbon atom) is situated adjacent to a substitutional nitrogen atom in the diamond structure [88]. The defect is optically active, absorbing light in the green part of the visible spectrum, and emitting in the region of 637 nm to 800 nm [28]. The NV centre can usually be found in one of the following two charge states: neutral (NV^0) or negatively charged (NV^-) [89]. For those that wish to learn more about the NV centre, I recommend the following review papers as an introduction to the nitrogen-vacancy defect: For a review of the NV centre as a whole, I recommend the paper "Theory of the ground-state spin of the nv^- center in diamond "[28]. For a thorough treatment of the theory of the NV^- centre in relation to magnetometry, I recommend "Magnetometry with nitrogen-vacancy defects in diamond" [90], and to discover more about the use of the NV^- centre in thermometry, I recommend reading the following paper "Temperature Dependence of the Nitrogen-Vacancy Magnetic Resonance in Diamond" [37].

The properties of the negatively charged NV centre form the foundation of much of the work presented in this thesis. The NV^- defect occurs when a donor electron from substitutional nitrogen atoms become trapped by the NV^0 defect[91]. The donor electron and the free unpaired electron from the nitrogen atom in the carbon lattice form a $S = 1$ spin system of two unpaired electrons [28]. A schematic of the electronic energy level system of the NV^- centre can be seen in figure 3.1. The electronic energy levels consist of a ground state spin triplet $^3A_2$, whose structure can be described by the following equation:

$$\hat{H} = \mathbf{S} \cdot D(T) \cdot \mathbf{S} + g\mu_B \mathbf{B} \cdot \mathbf{S} \tag{3.1}$$

In the above, **S** is the vector describing the spin-state of the NV^- centre, D(T) is the temperature dependent zero-field spitting of the NV^- centre due to the electron-electron interaction between the unpaired electrons making up the defect. g and μ_B are the gyromagnetic ratio of the NV^- centre (2.002) [28] and the Bohr magneton respectively. **B** is the vector describing an applied magnetic field. As discussed in the published work [92], the impact of the strain on the ODMR spectra recorded from an NV^- centre within a nanodiamond is generally seen as a lifting of the degeneracy between the $|\pm 1\rangle$ spin states. This results in two minima being observed in the ODMR spectra, representing the transitions $|0\rangle \rightarrow |1\rangle$ and $|0\rangle \rightarrow |-1\rangle$. Given the parameters of our investigation, we expect the effect of crystallographic strain in the nanodiamonds to remain constant throughout all experiments. As a result, we have chosen to ignore the effects of strain in the Hamiltonian, as have any paramagnetic defects that might induce hyper-fine splitting of the spin energy levels. In the absence of an applied magnetic field, the $|\pm 1\rangle$ spin energy levels are degenerate, producing an effective two level spin system separated by the zero-field splitting factor D(R.T.) = 2.87 GHz [37]. When a magnetic field is applied, the degeneracy of the $|\pm 1\rangle$ spin states is lifted and the three level structure of the electronic ground state is revealed [28]. The effect of the strain splitting, externally applied magnetic field and a change in temperature can be seen in figure 3.2. It can bee seen that the introduction of strain splitting has the same effect as that of an applied magnetic field, a loss of spin-state degeneracy, resulting in two spin-state resonances being observed in the ODMR spectra [28]. It is therefore possible for one to correct for the effect of strain splitting effects in the ODMR spectra from an NV^- centre via the application of an applied magnetic field with the correct magnitude and orientation.

In this work, we focus on the negatively charged NV centre owing to its

sensitivity to both magnetic fields and temperature [36, 90, 37, 93, 35].

The excited electronic energy level of the NV^- centre is also a spin-triplet system that mirrors the structure of the electronic ground state [90]. Transitions from the electronic ground state to the excited electronic energy levels can be accomplished via the absorption of a 532 nm photon [94]. These transitions are largely spin-conserving, meaning that energy level transitions via photo-absorption does not result in a change in the spin-state of the defect [95]. Once the NV^- centre is in the higher electronic energy state, the defect has two path through with it can decay: the "brighter" and the "darker" decay paths [28]. The "brighter" decay path results in the emission of a photon in the deep-red part of the visible spectra (637 nm - 800 nm), this decay path is spin-state conserving [96]. The "darker" decay path results in phonon-mediated inter-system crossing events [28]. The result of phonon-emission is that the NV^- centre decays into the excited singlet state (^{1}E) of the NV^- centre. From here, the NV^- centre emits a 1042 nm photon to decay down into the ^{1}A energy level before another inter-system crossing event occurs and the NV^- defect preferentially relaxes back down into the $|0\rangle_g$ spin state [28]. The NV^- centre is known to decay approximately 30% more often when in the $|\pm 1\rangle$ spin states [51]. As a result, we can describe the fluorescence intensity from the NV^- centre as being spin-dependent.

3.1.1 Optically Detected Magnetic Resonance Spectroscopy

The zero-field splitting of the NV^- centre is known to be equivalent to a microwave photon with a frequency of 2.87 GHz [89]. Transitions between the spin-states of the NV^- centre can be driven by the interaction of the defect with the magnetic field component of an absorbed microwave photon [97]. In resonantly driving the spin state of the NV^- centre out of the $|0\rangle$, the defect is more likely to decay via the darker decay path, described earlier, and therefore result in a drop in the fluoresent emission from the diamond sample under study [90]. By apply-

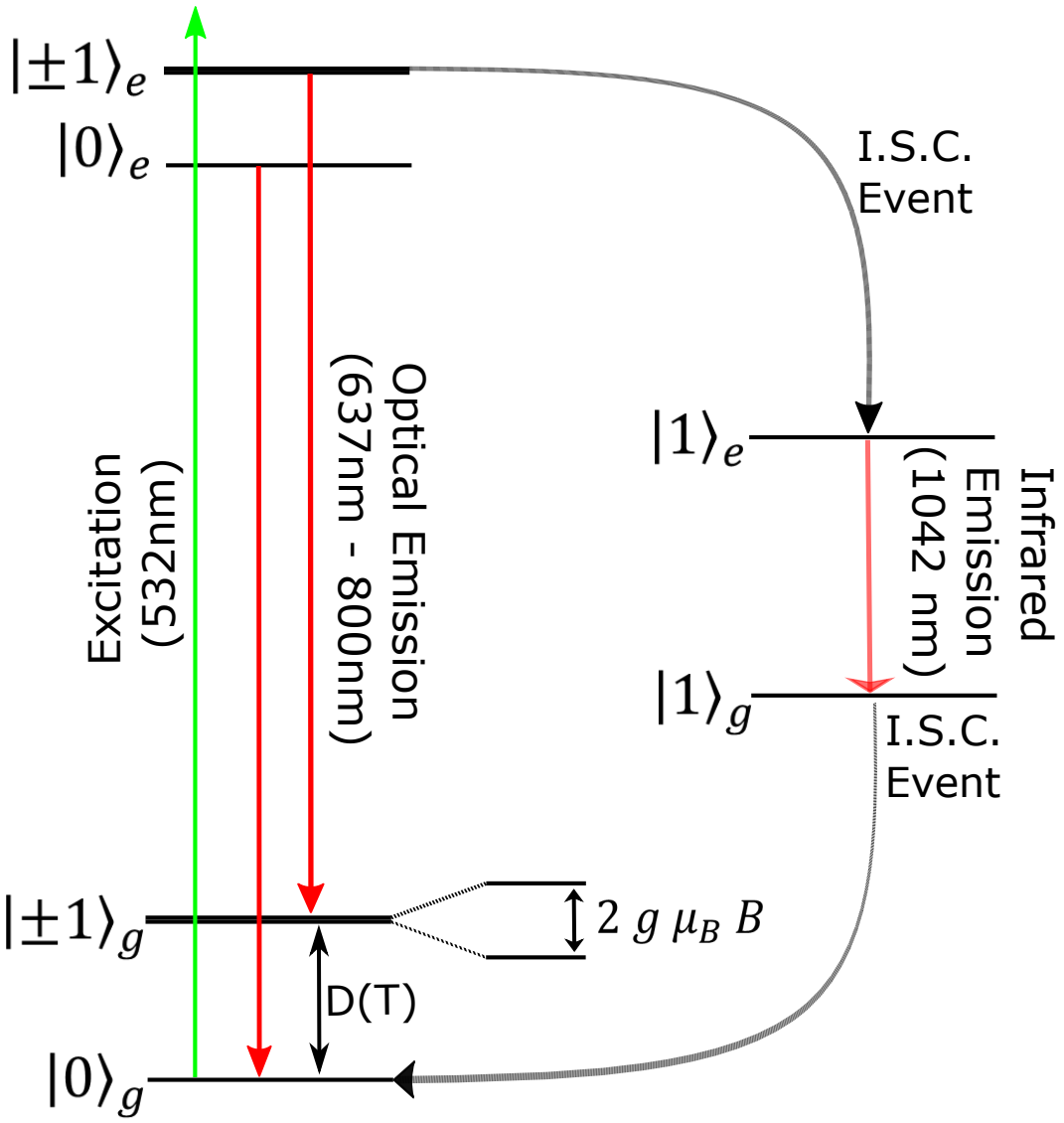

Figure 3.1: A schematic of the NV centre energy levels. In the above figure the decay paths involving an inter-system crossing are denoted by the abbreviation ISC event.

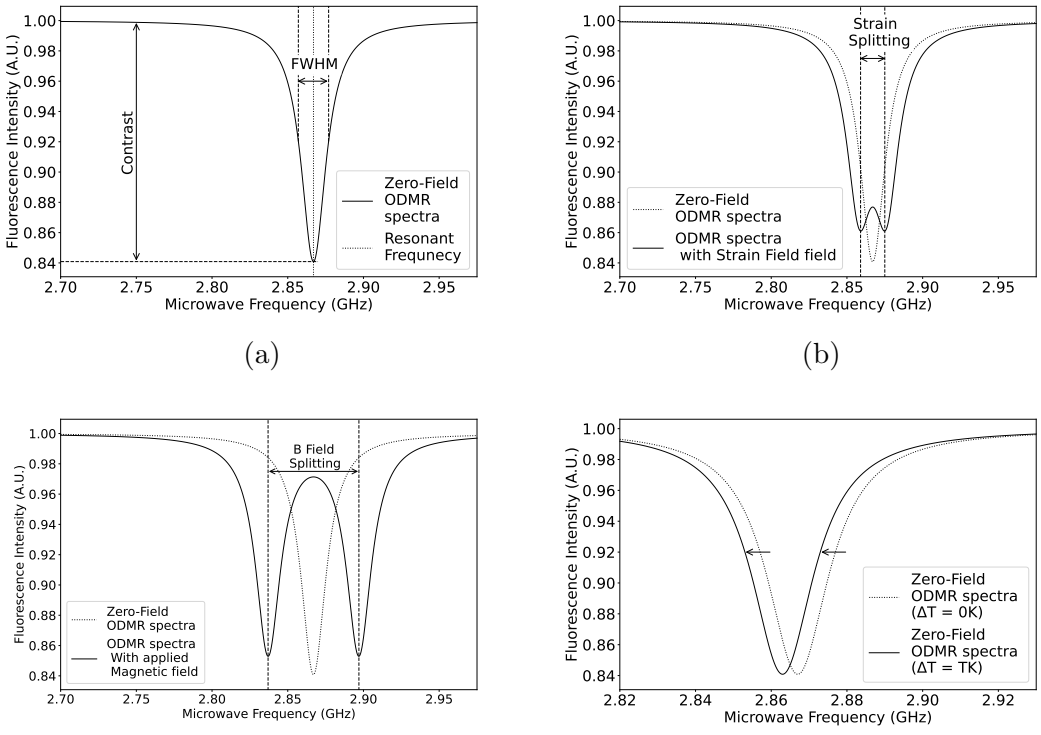

Figure 3.2: Here I show an example of a simulated ODMR curve from a single NV centre with no external fields applied (figure 3.2a). In the subsequent images, I have simulated the effects of: internal crystallographic strain (figure 3.2b), magnetic field (figure 3.2c) and the effect of a change in temperature (figure 3.2d). In figures 3.2b to 3.2d, the zero-field ODMR curve simulation has been added to the plot as a dashed line for reference.

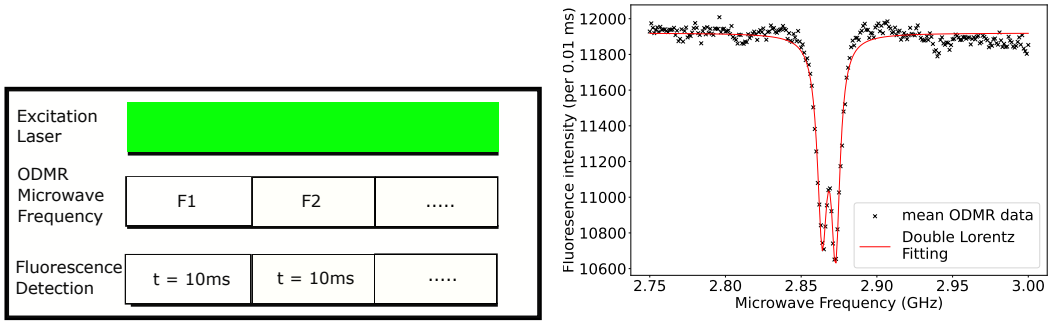

(a) (b)

Figure 3.3: A schematic of the measurement scheme of the optically detected magnetic resonance spectroscopy measurements 3.3a. In figure 3.3b is an exemplar ODMR spectra recorded from our experimental set-up.

ing a variable frequency microwave field centred around this value to the NV^- centre and monitoring the fluorescence intensity from the defect, we are able to accurately determine the resonant frequency of the NV^- defect [1]. This measurement process is known as optically detected magnetic resonance spectroscopy (ODMR) [89]. The measurement sequence can be seen in figure 3.3, alongside an example of the spectra recorded from an ODMR measurement in the absence of an applied magnetic field. In figure 3.3b, the ODMR spectra shows a double dip for the fluorescent minima. This is the result of the crystallographic strain in the diamond lifting the degeneracy of the $|\pm 1\rangle$ spin states.

Modelling the ODMR Spectra

In order to extract meaningful data from the ODMR spectra we wanted a mathematical function that could describe the emission intensity profile from the NV^- centre as the microwave frequency is swept. There were three choices for the distributions that could be used to model the ODMR spectra, these were:

- Lorentz function:

$$y_{Lorentz}(x) = \left(\frac{A}{\pi}\right) \frac{\Delta\nu^2}{\Delta\nu^2 + (2x - 2\mu_{res})^2} \; + \; C. \tag{3.2}$$

- Gaussian Distribution:

$$y_{Gaussian}(x) = \left(\frac{A}{2\pi\Delta\nu}\right) \exp\left\{-\frac{(x - \mu_{res})^2}{2\Delta\nu^2}\right\} \; + \; C \tag{3.3}$$

- Voigt Function

$$y = y_{Lorentz}(x) \otimes y_{Gaussian}(x) \tag{3.4}$$

In the above equations, A is a constant of fitting used to determine the depth of the ODMR dip, $\Delta\nu$ is the full width, half maxima (FWHM) of the Lorentzian dip, x represents the applied frequency, μ_{res} is the resonant frequency of the NV^- centre/ensemble spin state transition (either $|0\rangle \rightarrow |1\rangle$ or $|0\rangle \rightarrow |-1\rangle$).The Lorentzian distribution is used to describe the natural linewidth or the homogeneous lifetime broadening of a quantum state transition [98]. The Gaussian distribution by comparison is used to describe systems in which the lifetime of a quantum state undergoes inhomogeneous broadening [99]. The Voigt function is the linear convolution of these two functions and is often used to describe systems in which neither homogenous or inhomogenous lifetime broadening dominate the transition dynamics of a quantum system [99]. It is thought that the Voigt function would be the most useful to model the ODMR spectra from systems containing a small ensemble of inhomogeneously broadening oscillators [99]. As discussed later in this work (section 3.5.4), our nanodiamond samples vary in size and contain varying quantities of NV^- within their structure. We would expect that the larger diamonds, which have the highest quantity of NV^- defects, to be best described by the Gaussian distribution. With such a large number of defects within the crystal, we would expect to see inhomogeneous lifetime broadening as

a result of spin-mixing between the defects [100]. In figure 3.4, we can see the three different ODMR fits applied to the same ODMR spectra dataset, recorded from an NV^- ensemble within a 70 nm ND, using the ODMR with referencing protocol, described later in section 3.7. Included in these figures are the R^2 values, which was use to calculate the goodness-of-fit for the different distributions to the dataset. The R^2 value was calculated using the following equations:

$$SS_{Tot} = \sum (y_i - \bar{y})^2 \tag{3.5}$$

$$SS_{Res} = \sum (y_i - y_{fitting,i})^2 \tag{3.6}$$

$$R^2 = 1 - \frac{SS_{Res}}{SS_{Tot}} \tag{3.7}$$

In which y_i is the i^{th} normalised intensity value as a function of frequency, $\bar{y}$ is the mean value for normalised intensity, and $y_{fitting,i}$ is the i^{th} value for the statistical distribution fitted to the ODMR data as a function of frequency. SS_{Tot} then represents the variation in the experimental y values, and SS_{Res} is the sum of the squared residual error between the y data and the fitting of the statistical distribution. All of the fittings used to model the data show a goodness-of-fit of over 90%. From visual inspection, the Lorentz and Voigt functions more accurately describe the shape of the ODMR dataset than the Gaussian, which is reflected in the R^2 value. The Voigt function is also found to be equivalent to the Lorentzian function at describing the shape of the ODMR curve, with both fittings having an R^2 value of 97.8%. There is not much to choose between these two fitted statistical distributions. There is no benefit in calculating the Voigt function in terms of accuracy describing the ODMR dip, and is computationally more complex as the Voigt function is a convolution of the Lorentzian and Gaussian fittings. I have chosen, therefore, to use the Lorentz function to model the results of the

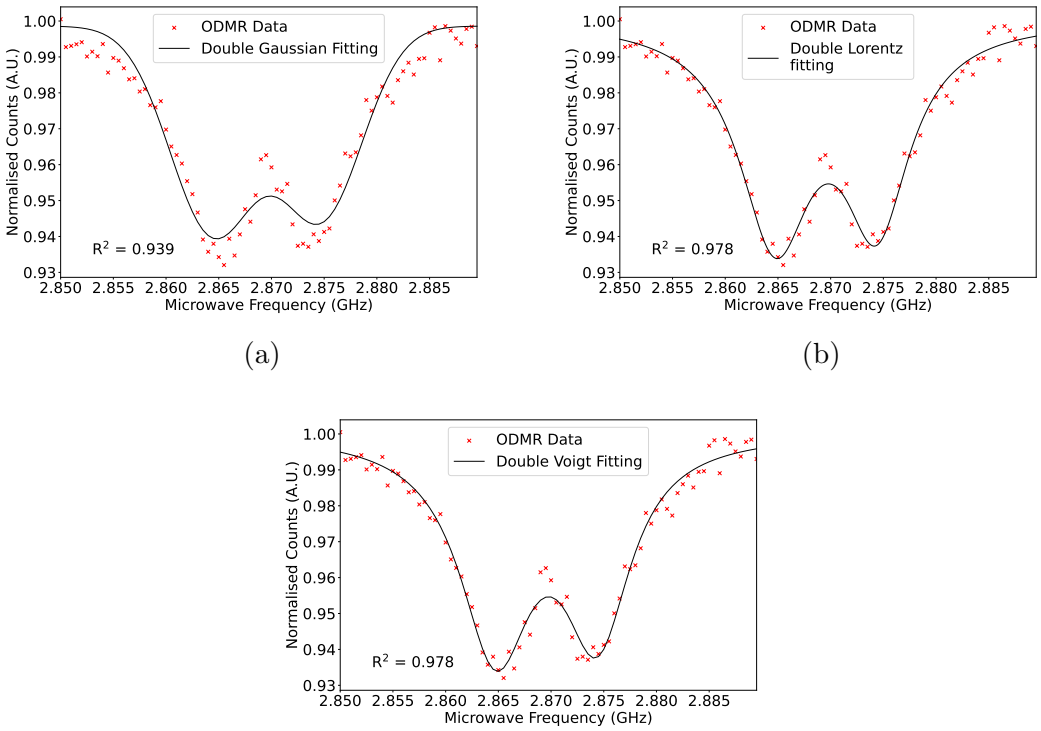

Figure 3.4: The comparison of the fitting functions used to model the shape of the ODMR spectra recorded using a 70 nm diameter diamond with ≈ 100 NV^- present. Shown here are the least-squares fitting of the Gaussian distribution 3.4a, Lorentzian distribution 3.4b and Voigt distribution 3.4c to the experimental data.

ODMR data. From this fitting I am able to extract the resonant frequency of the NV centre, the full-width half maxima and the contrast from the ODMR datasets.

This is an interesting result, as it implies that the lifetime of the NV^- centres is homogeneous for an ensemble of defects within a single nanodiamond [98]. The use of the Lorentzian function to fit ODMR data from NV^- ensembles within nanodiamond crystals is well documented in the literature [101, 102, 103]. The focus of this work was to utilise the ODMR spectra of the NV^- ensembles within nanodiamond for magnetic field and temperature sensing. As a result, knowing the best function to empirically model the shape of the ODMR spectra without

investigating the underlying crystallographic structure of the nanodiamonds or quantum interactions within the crystal was sufficient for this project.

3.2 Microwaves: Initial Setup

An integral part of performing optically detected magnetic resonance (ODMR) spectroscopy using the negatively charged nitrogen-vacancy centre is the delivery of microwaves to the sample [89]. When beginning this project we selected the SMB 100A microwave generator from Rohde and Schwartz for microwave delivery. The generator has a frequency range of 9 kHz to 3.2 GHz and a power range of -145 dBm to +30 dBm. Given the result published by [87] this frequency and power range was sufficient to perform ODMR on the NV^- centre. The microwave generator was connected to a +20 dB amplifier (Microwave Amps AM38-2.9S-20-40) by SMA terminated coaxial cables. The addition of the amplifier facilitates an increase in the microwave power to up to 40 dBm (10 W). This amplifier allowed us to compensate for any losses in the microwave circuit and ensure high microwave power delivery at the sample position. From the microwave amplifier, the microwaves travel along coaxial cables down to a circulator (Pasternack PE83CR1004) from which the microwaves are directed towards the sample. Any back-reflected microwave power from the sample arm is fed back into the circulator and sent towards a high power 50 Ω microwave terminator.

3.3 Split Ring Resonators

In 2014, Bayat *et al* published their work characterising a double split ring resonator (DSRR) for microwave delivery during ODMR experiments [87]. The group detail the design parameters for a microwave ring resonator that is able to produce a wide area (0.95 mm × 1.2mm) uniform microwave field for ODMR

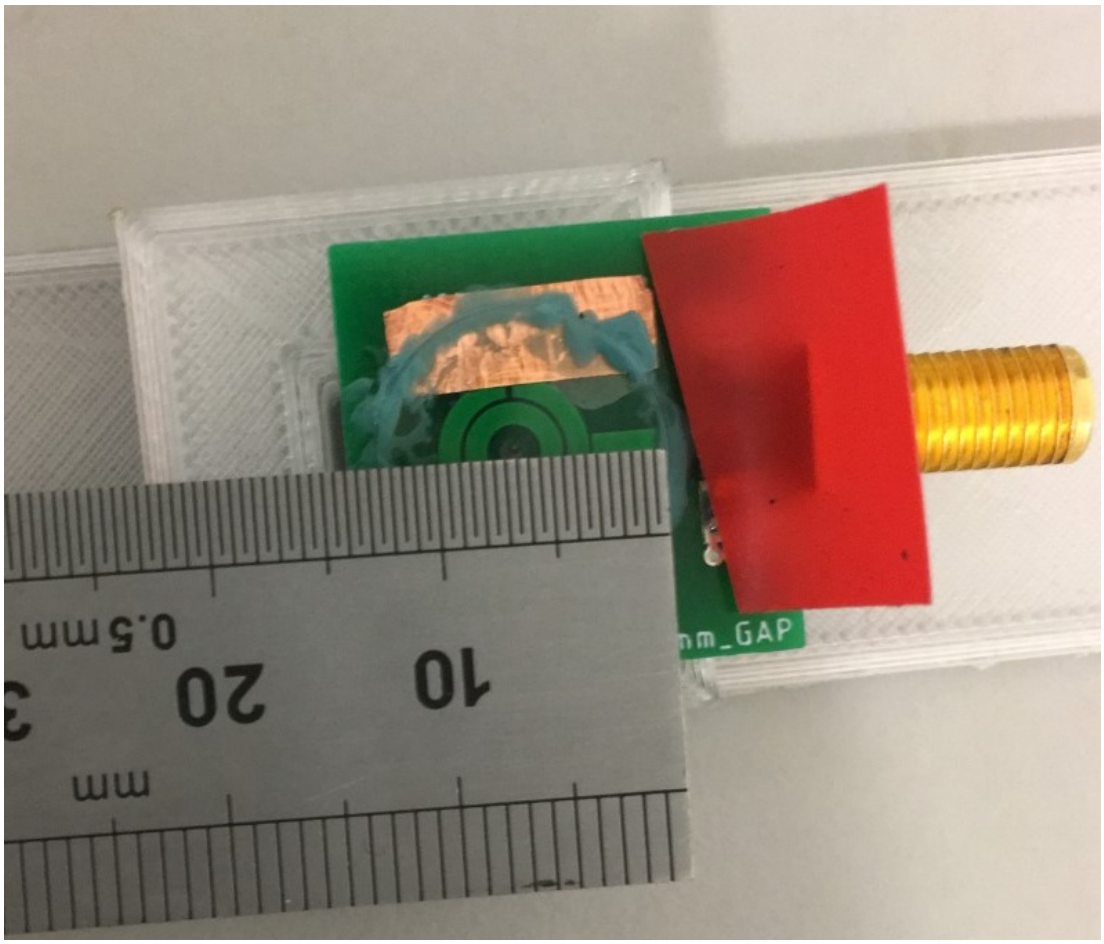

Figure 3.5: An image of the double split ring resonator with a nanodiamond coated coverslip fixed to the surface. A ruler with 0.5 mm divisions has been included in the image to be used as a scale.

experiments. They showed that in a home built confocal microscope, they were able to achieve a 10% ODMR contrast from NV^- defects within a bulk diamond sample [87]. An example of such a microwave resonator can be seen in figure 3.5. This work was of particular interest to for this research project as a uniform, wide-area microwave field would allow us to investigate a relatively wide-area of a biological sample when performing magnetic field or temperature sensing. This is compared to a system using a microwire for microwave delivery [104].

We ordered the manufacture of double split ring resonators (DSRRs) from the designs outlined by Bayat *et al.* The DSRR were used during the set-up of the microwave circuit and the initial ODMR measurements. Once we had developed a robust ODMR experimental protocol, we set about analysing the performance of the ring resonators in our experimental set-up. We did make one change to the resonator design, and that was to drill a 1 mm hole through the centre of the inner-most resonator ring. This was to allow for sample back-lighting, which was required for the identification of cell position when working towards using the resonators for biological sensing.

3.3.1 Characterisation

Before the DSRR's were used for ODMR experiments we wanted to characterise the resonant frequency of the resonators to make sure that they were suitable for our experiments. To characterise the resonant frequency of the DSRRs, we monitored the back-reflected microwave signal from the ring resonators when they were attached to our microwave circuit. The back-reflected signal from the resonators was recorded using the Aim TTI PSA3605 spectrum analyser, which was connected to the back-reflection port of the circulator. To assess the performance of the DSRR, the trace recorded with the DSRR in the sample position of the microwave circuit was compared to the trace recorded with nothing terminating the sample side of the circulator. While recording the back-reflected signals using the spectrum analyser, the microwave frequency was scanned using the Rohde & Schwartz SMB100A microwave generator from 2.5 GHz to 3.2 GHz in steps of 1 MHz. To record a complete frequency spectra, the integration time for each applied frequency was one second. The spectrum analyser was operated in "peak-hold" mode, meaning that the maximum power output observed for each of the applied frequencies was used to build the spectra used for analysis.

To quantify the magnitude of the microwave signal being coupled into the DSRR, I measured the mirowave signal at the back-reflection port of the circulator under two conditions: the first was without the DSRR attached to the microwave circit, and the second was with the resonator in place. Figure 3.6a shows the results of these two measurements. From the analysis of these results, it can be seen that the back-reflected microwave power with the DSRR in place is lower than the spectra recorded when the sample port of the circulator was not terminated. This suggests that the microwave power is being radiated through the ring resonator as we would expect [87].

Figure 3.6b shows the spectra of the back-reflected microwave signal from the DSRR with the spectra recorded when the sample port of the circulator was not terminated has been subtracted away. By plotting this signal, we can more clearly identify the resonant frequency of the DRSS, as the power fluctuations that arise from the microwave generator and the microwave circuit, both of which are constant and removed from consideration. In this figure, the minimum of the back-reflected microwave power is at 2.95 GHz the resonant frequency that the DSRR was tuned to. Ideally, the DSRR would be tuned to 2.87 GHz corresponding to the resonant frequency of the NV^- centre. This is approximately 200 MHz too high if we want to maximise the ODMR signal from the unperturbed spin-resonant frequency of the NV^- centre.

In their paper, Bayat *et al* mention the need to tune the resonant frequency of the DSRR using copper tape to maximise its effectiveness for ODMR measurements [87]. While attempting to perform such frequency tuning for our experiments, I noticed that the addition of the coverslip and the adhesive (nail varnish) used to fix the coverslip to the DSRR also had an effect on the resonant frequency tuning. As such, I performed a short investigation to find the frequency shift related to each stage of the sample preparation routine. By quantifying the resonant frequency shift at each stage of the sample preparation routine, I would

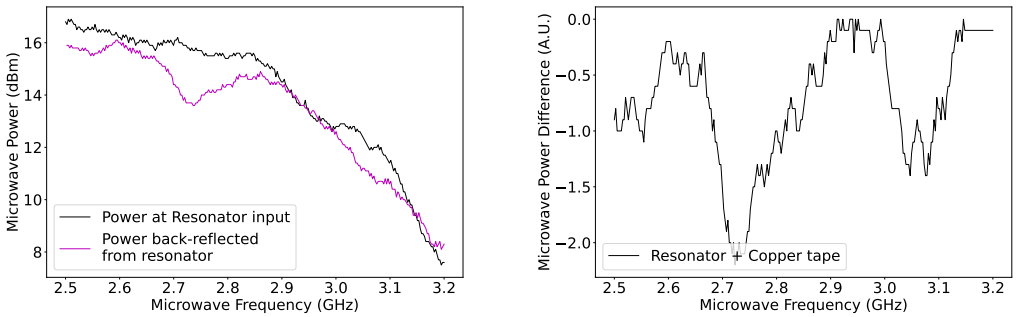

(a) (b)

Figure 3.6: A comparison of two microwave spectra recorded at the back-reflection port of the circulator. In figure 3.6a we can see the difference between the back-reflected spectra from the non-terminated (background) sample port of the circulator (black) and the reflections from the sample port when terminated by the DSRR (magenta). In figure 3.6b I have plotted the results of subtracting the spectra recorded for the background measurement from the spectra recorded with the DSRR in place.

be able to prepare samples with the resonance of the DSRR tuned as closely to 2.87 GHz as possible. I broke the sample preparation into 4 parts:

1. Frequency tuning of the DSRR using copper tape.
2. Placing a coverslip on the surface of the DSRR.
3. Placing a drop of immersion oil between the DSRR and the coverslip.
4. Fixing the coverslip to the surface of the DSRR using the nail-varnish adhesive.

The spectra recorded from these measurements can be seen in figure 3.7 and the mean frequency shift from each of the four steps of the sample preparation can be seen in table 3.1. The FWHM of the dip in the back-reflected spectra from the DSRR is approximately 200 MHz. The compound error for each stage of the sample preparation routine is 54 MHz. As the compound error for the

Table 3.1: The results of the investigation showing how each stage of the sample preparation of the DSRR for ODMR affected the resonant frequency of the resonator. The application of the copper tape in stage 1 of the sample preparation can create an arbitrary frequency shift, so was not quantified in this study. The error in these measurements comes from the standard deviation of measurements recorded at each step of three repeats of the DSRR preparation routine.

Sample Prep Stage	Frequency Shift (MHz)
1 (copper tape)	NA
2 (Coverslip)	-80 ± 20
3 (Immersion oil)	-120 ± 30
4 (nail-varnish)	-90 ± 40

measurement is smaller than the FWHM of the back-reflected spectra, the compound error can be largely ignored when reviewing these results. During stage 1 of resonator tuning, the application of the copper tape can be used to create an arbitrary frequency shift to the resonant frequency of the DSRR based upon the size of the copper strip and its placement across the resonator surface. As a result, the frequency shift due to this stage of resonator tuning was not quantified. The combined frequency shift from sample preparation stages 2 - 4 is -290 MHz. We know that to have optimal performance for ODMR, we require that the DSRR is tuned to 2.87 GHz with the sample mounted to the resonator. Using the information from this short study, I identified that by tuning the resonant frequency of the DSRR to 3.16 GHz to compensate for the detuning effects of the sample preparation routine gave me the best opportunity to correctly tune the resonator for ODMR measurements. The frequency shift measured during stages 3 and 4, in which the immersion oil and nail varnish were applied to the sample, were found to be highly dependent on the quantity used. These measurement reported here were used as a guide for the initial frequency tuning of the DSRR's. They should not be considered as a robust characterisation of the effect of either immersion oil or nail varnish on the resonant frequency of the double split ring resonators.

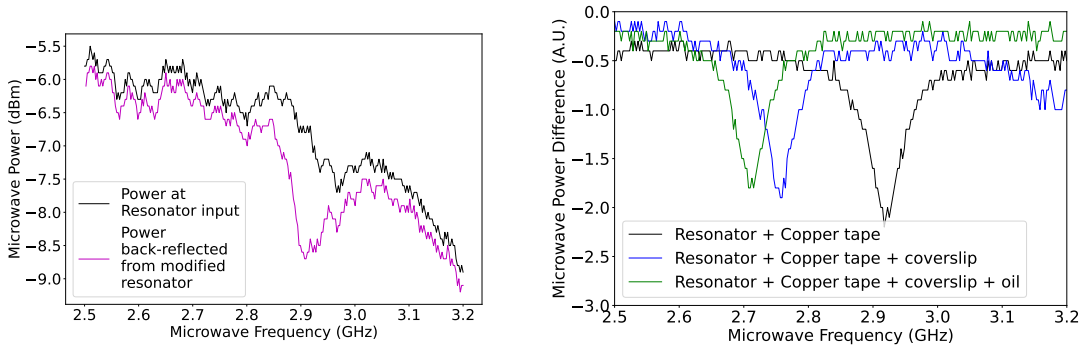

(a) (b)

Figure 3.7: A comparison between the back-reflected microwave signal from the double split ring resonator unmodified (black), and then when the resonator had been prepared for ODMR measurements (magenta) is seen in figure 3.7a. In figure 3.7b we see the back-reflected signal from the resonator during each stage of the sample preparation for ODMR. For each of these spectra, the back reflected signal from the unmodified resonator has been subtracted from the signal.

3.3.2 Initial ODMR Measurements

With the DSRR tuned to 2.87 GHz, we were able to start performing ODMR measurements. 90 nm diameter nanodiamonds were chosen for the initial ODMR experiments. The large NV^- ensemble in the crystal gave us the greatest signal to noise for an ODMR measurement, and thus made the drop in the fluorescence intensity due to the application of a resonant microwave field easier to detect.

In the initial ODMR measurements, the power output from the microwave generator was set to 15 dBm. The signal was passed through the 20 dB amplifier to give a total delivered power to the sample of 35 dBm (3.16 watt). The applied microwave frequency scan range ran from 2.82 GHz to 2.92 GHz with a frequency step of 1 MHz. The frequency step dwell time and photon integration time were both set to 10 ms, ie: the fluorescent signal from the nanodiamond was recorded every 10 ms, to match the length of time each microwave frequency in the sweep was applied. Throughout this experiment the nanodiamond was under continual

laser excitation, and at the beginning of the experiment, the mean fluorescence intensity was $99.000 \pm 0.001\,\mathrm{M\,Counts\,s^{-1}}$. For these initial experiments, we had yet to implement remote triggering of the microwave frequency scan to coincide with the recording of the fluorescence intensity. For this measurement Dr Graeme Johnstone and I manually synchronised the start of the microwave frequency scan with the measurement of the NV^- centre fluorescence. The fluorescence intensity from the NV^- ensemble was recorded for 60 s, during which time the microwave frequnecy scan was repeated multiple times. The results of this measurement can be seen in figure 3.8a. This graph shows the fluorescence intensity from the NV^- centre ensemble in the nanodiamond under study recorded through the duration of the ODMR measurement. One of the recorded ODMR dips is shown in the inset of the figure. The results show that we were able to successfully observe multiple ODMR dips throughout the duration of the measurement. Another key feature of this result is the observed drift in the system. This is likely the result of sample drift. This measurement was made soon after the sample was brought into the focus of the microscope and had not been given time to settle. As a result, the sample still has some residual movement from being brought into focus and the sample stage position being moved laterally. As this was a proof of principle measurement, we were not concerned with the amount of drift observed in this measurement. As seen in section 3.5.2, when the microscope is given time to settle, it is extremely stable (9% loss in detected fluorescence from a diffraction limited spot over 12 minutes).

To improve the signal to noise in this measurement, I wanted to find the mean fluorescence intensity for each applied microwave frequency. To do this I first performed a simple drift correction using a linear fit to the data. I determined the number of data-points equivalent to one full ODMR microwave frequency span (456 points) and segmented the results into a series of 456 data point arrays.

From this point, I was able to calculate the mean ODMR signal detected from the nanodiamond sample [105], the results of which can be seen in figure 3.8b. The contrast between the off resonant signal and the minima of the ODMR dip is between 0.76% and 1.2% depending on whether the high or low frequency region of the scan is used as the fluorescent baseline. The off-resonant fluorescent signal is not as stable as has been reported previously [94, 102, 90], which is not surprising given the sample drift that could be seen in figure 3.8a. These results also show the effect of the crystallographic strain within the nanodiamond lifting of the degeneracy of the $|\pm 1\rangle$ energy levels, resulting in the characteristic "double dip" ODMR lineshape [28, 101, 102, 106]. From previously published works studying the ODMR response of NV^- centres within nanodiamond crystals, we know that the strain splitting of the NV^- centre spin energy levels should be centred around the zero-field resonant frequency of the NV^- centre (2.87 GHz [28]. I have included a dashed line in figure 3.8b to represent where we would expect the 2.87 GHz microwave frequency to be applied, given the shape of the ODMR curve. I have left the x axis of this graph as the number of data-points per frequency line scan, rather than converting this to applied microwave frequency. This is for two reasons:

1. Due to the inability to trigger the ODMR scan and the frequency counting at the same time, it is very likely that no individual data-point in the measurement is perfectly aligned to the applied microwave frequencies. There is likely to be some overlap between two applied microwave frequencies in each data-point recorded.

2. There is some over-head in each measurement of the fluorescence intensity from the nanodiamond. The clock used for these measurements was not able to produce accurate 10 ms photon integration times. As a result, I am not able to accurately draw any relationship between the pixel value and

the applied microwave frequency.

There was much to learn from this measurement, chief among these findings was that the DSRR can be used to generate ODMR curves within our measurement system. More significantly, I was able to identify a series of improvements that could be made to improve the quality of the measurement system we were using. The most obvious of these improvements was the ability to trigger the start of the ODMR line scans with our microscope control software. This would allow the photon counting to be synchronised with the applied microwave frequency and thus allow deterministic measurement of the spin-dependent fluorescence of the NV^- centre. The data from these now synchronised ODMR measurements could also be saved so that each new frequency line scan was saved as a new line in the .dat file, simplifying data analysis. Finally, by linking the photon-counting dwell time to the internal clock of the FPGA (80 MHz) used to control the confocal microscope, we would have a more reliable counting method for performing the ODMR measurements.

With the identification of these improvements, Dr Brian Patton was able to design a new .vi using LabView, incorporating these recommendations to develop a robust ODMR measurement protocol. An example of an ODMR measurement performed using the new ODMR measurement software can be seen in figure 3.9. This figure shows a heat-map of the ODMR measurement, in which the applied microwave frequency and the number of frequency line scan repeats are the x and y axis respectively. The colour of each pixel then denotes the fluorescence intensity recorded for each measurement point. From this measurement one can see the stability of the measurement was much improved, with only a 10% loss in fluorescence over the course of the measurement. Figure 3.9b shows a scatter plot of the mean fluorescent signal recorded for each of the applied microwave

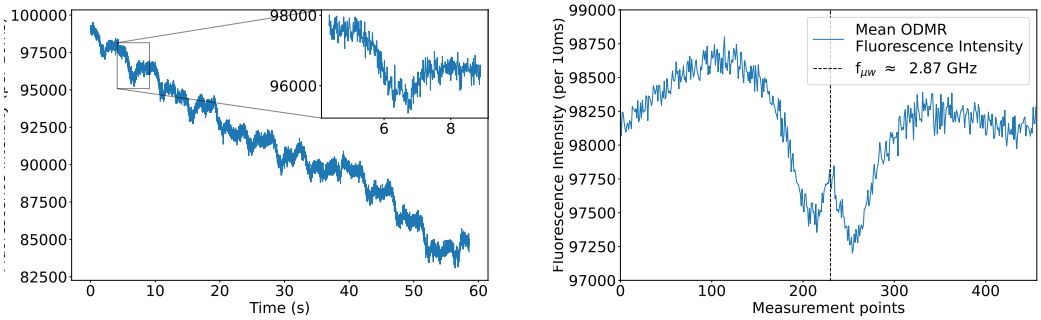

(a) (b)

Figure 3.8: The first ODMR measurement recorded using our microscope system. Figure 3.8a shows the fluorescence intensity from the nanodiamond under study recorded over time as the microwave frequency scan range is running. Multiple ODMR dips can be seen in this spectra (see inset). In figure 3.8b the mean drift-corrected ODMR signal from the graph is figure 3.8a can be seen. A dashed line has been included on the plot as an estimation of where we would expect the zero-field resonant frequency (2.87 GHz) should lie on this plot. This is not the exact value however as the frequency sweep and photon counting were not synchronised.

frequencies. The stability of the off-resonant signal in this measurement is noticeably improved when compared to figure 3.8b. A Lorentzian lineshape has been used to describe the ODMR dip from the ODMR results. Referred to throughout this work as a "double Lorentzian" fitting, the fit consists of the summation of two Lorentz distributions to the data to capture the resonant frequency of both ODMR dips seen in the data. From the shape of the graph in figure 3.9b. We measure the strain splitting in figure 3.9b to be equivalent to 11.7 MHz [107] using the resonant frequencies of the NV^- centre as determined by the double Lorentz fitting, which is comparable with the strain splitting reported from nanodiamonds [1, 102].

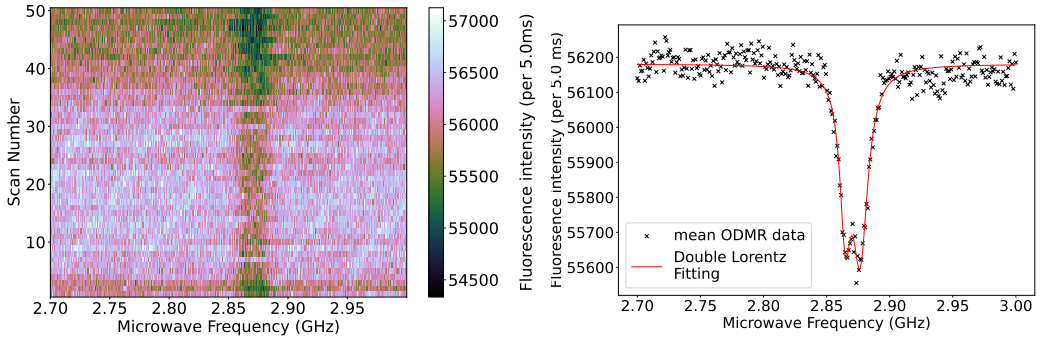

(a) (b)

Figure 3.9: The ODMR scan performed using the second iteration of the ODMR measurement protocol. Figure 3.9a shows a heat map of the complete ODMR experiment. Figure 3.9b shows the mean fluorescence intensity for each applied frequency in the ODMR scan.

3.3.3 Testing Microwave Resonator Field Uniformity

In the previous section we showed that we were able to perform ODMR measurements using the double split ring resonators to deliver a microwave field to a nanodiamond sample. The next step in the characterisation of the DSRRs was to test the uniformity of the microwave field across the resonator. From the results published by Bayat *et al*, we would expect that we would observe constant ODMR contrast across the resonator surface [87].

For these experiments, the microwave power supplied to the sample was kept constant across all measurements at 35 dBm (3.16W), with the microwave frequency scanned about the NV^- centre resonant frequency. A 90 nm diamond was prepared for imaging following the routine described in appendix A.2. Starting at the centre of the DSRR, ODMR spectra were recorded from nanodiamonds spread across the surface of the resonator design. The stage position is controlled by Zaber stepper motors to translate the sample stage (and therefore the resonator) laterally relative to the microscope objective. Using the positional feed-

back from the stepper motors, we were able to get an accurate determination of the position of the nanodiamond under study on the resonator surface. In figure 3.5 we can see the an example of one of the double split ring resonators prepared for these measurements. A ruler has been used to give an idea of scale and was used to determine the distance that needed to be moved across the surface of the resonator to reach the different areas of interest. We decided to test the ODMR contrast produced at 4 different positions on the resonator surface, these were:

1. The centre of the resonator design.
2. The inside edge of the inner most ring.
3. The outer edge of the inner most ring.
4. The inner edge of the outermost ring

The positions that we trialled here are beyond the area of the DSRR in which the uniform microwave field was reported [87]. The reason that we wanted to explore beyond this region is that we were consistently seeing ODMR contrast of 1% or lower in this region, which we did not feel would give us sufficient sensitivity when performing magnetic field or temperature sensing experiments [1, 35]. The results of these measurement can be seen in table 3.2. The results show that the ODMR contrast observed was less than 1% and relatively consistent across positions 1-3. At position 4 on the resonator, the ODMR contrast was more than 4 times the contrast that was observed throughout the rest of the resonator (4.03%). This was an unexpected result, however, on closer inspection of the simulations published by Bayat *et al*, it can be seen that at the inner edge of the outer most ring does have a maximum projection of the microwave field [87]. We believe that we are observing the effects of this maximum field projection in our measurements.

Table 3.2: A table showing the mean ODMR contrast observed from multiple measurements recorded at each point across the surface of the double split ring resonator. The error in the measurement is the standard deviation of the ODMR contrast values recorded.

Position on Resonator	ODMR contrast
1	0.7 ± 0.3
2	0.7 ± 0.1
3	0.40 ± 0.1
4	4.0 ± 0.5

3.3.4 ODMR Power Saturation Curves

One of the defining characteristics of ODMR measurements performed on the NV^- centre in diamond is the contrast saturation that occurs as the microwave power is increased [108]. The saturation limit for NV^- ODMR contrast is 30%, reflecting the saturation of spin-state transitions within the NV^- centre [28]. To test the capabilities of our measurement system, I varied the microwave power supplied to the sample while recorded ODMR measurements from a single diffraction limited cluster in the sample to observe the relationship between applied microwave power and ODMR contrast in our system. These measurements were performed using a 90 nm diamond sample. The microwave power was varied from 35 dBm down to 20 dBm, with the microwave frequency scanned around 2.87 GHz and the photon integration time fixed at 10 ms. The results of the experiment can be seen in figure 3.10. Rather than seeing saturation-like behaviour from the nanodiamond as the microwave power is increased, I observed a linear response of ODMR contrast to increased microwave power, with the maximum contrast recorded being 4.7%. When comparing our results to those published in Bayat *et al*'s paper, we see that our maximum contrast is about half that reported in their investigation, which was recorded with significantly less applied microwave power (30 mW). The results of this study suggest that we were not effectively coupling the microwave power into the sample chamber while using the DSRR.

Upon review of the Bayat *et al* paper, we noticed the key difference between our experiential setup was the choice of objective. In their paper, Bayat *et al* report using an air objective with a working distance of 4mm, in our microscope, we make use of an oil immersion objective with a working distance of just 150 µm.[87]. The DSRRs produce a 3D microwave field, however, the projection of this field normal to the focal plane is not given in Bayat's paper [87]. We suggest therefore that the microwave signal is possibly being grounded by the presence of our oil-immersion objective. This would then act to limit the microwave field generated by the DSRR, which would result in the lower than expected ODMR contrast that we observed.

3.3.5 Review of the Double Split Ring Resonator

The double split ring resonators presented by Bayat *et al* are a promising technology for quantum information processing [87]. With the ability to generate a large area uniform microwave field, loop-gap resonators open up the possibility of performing coherence time measurements across an entire diamond wafer [109]. In our system, which is set up for biological imaging and sensing, we found some draw-backs using the DSRR for microwave delivery. These are:

- The DSRR patterning on the PCB used in this experiment only allows for a 3.14 mm^2 hole to be used to back-light the sample for wide-field imaging. This limits the effective area of a glass coverslip that could be used for biological imaging.

- The strongest microwave field was located outside the field of view of the wide-field imaging arm of the microscope. For future experiments using biological samples this is not practical as we would not be able to identify the cells we wish to perform sensing on.

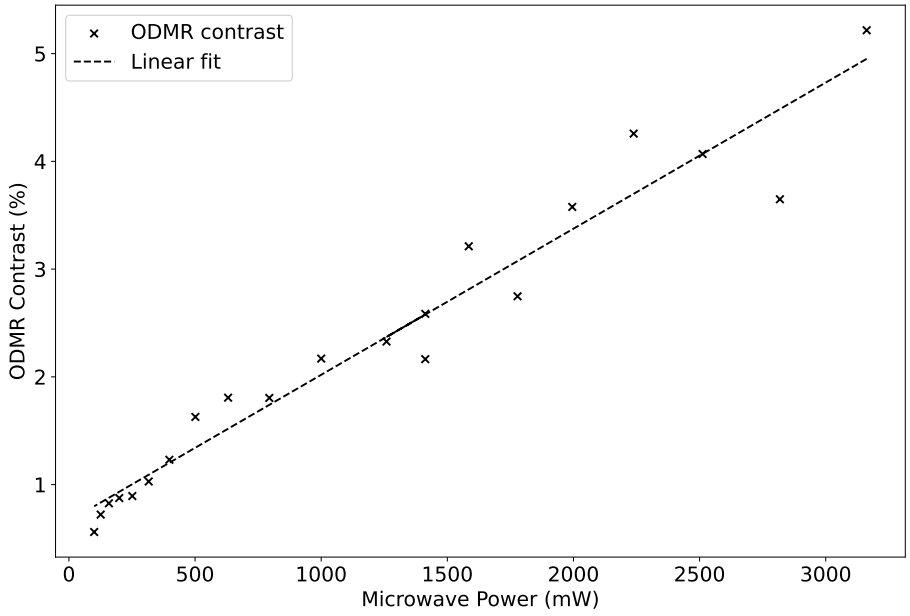

Figure 3.10: The dependence of the ODMR contrast from the NV^- centre on the microwave power applied via the double split ring resonator can be seen in this figure. A linear fit has been applied to the data shown here. Up to 3.16 W (35dBm) the ODMR contrast is linearly dependent on the microwave power applied. The gradient of the linear fit is 1.35 ± 0.07 % per 1 W of microwave power applied.

- The 3D microwave field seems to be grounded by our oil-immersion objective. The high NA of the oil-immersion objective is required for the field of view and detecting fluorescent emission from fluorophores within biological material. Therefore it appears that this method of microwave delivery is incompatible with our system.

- The resonators are difficult to tune to the correct resonant frequency. Small changes in the immersion media or coverslip adhesive quantity can result in a complete detuning of the DSRR resonant frequency away from the optimal 2.87 GHz.

For these reasons we decided that the double split ring resonator was not compatible with our experimental set-up and therefore we needed to try another approach for microwave delivery for ODMR experiments.

3.4 Coplanar Waveguides

Having ruled out the DSRR's as a method of microwave delivery, I reviewed the literature to find an alternative method of microwave delivery that would be compatible with our experimental setup. A coplanar waveguide with a micro-wire antenna seemed be most suitable and simplest method of microwave delivery we could use given the applications of our ODMR measurement system. The coplanar waveguide has been well documented previously for microwave delivery [110, 111, 112] and are known to deliver a relatively short-range microwave field around the microwire antenna [104]. This was potentially a benefit for our experimental setup, given the close proximity of the oil-objective was grounding signal projected by the DSRR.

A coplanar waveguide (microwave strip line) is characterised by a single conductive track sandwiched between two insulating strips which are in turn bordered

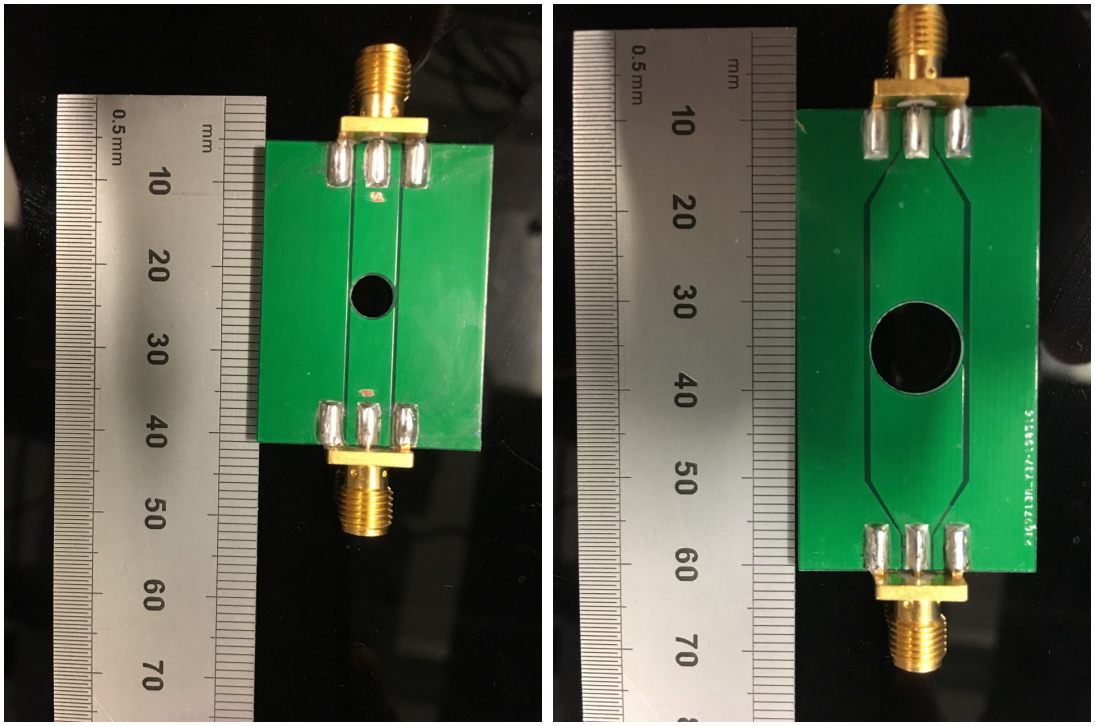

(a) (b)

Figure 3.11: Photographs of the linear (3.11a) and tapered 3.11b coplanar waveguides used for microwave delivery during ODMR experiments.

by a conductive ground plate [113]. By manipulating the size of the conductive strip and the insulating strips between the conducting and grounded plates, one can control the impedance of the coplanar waveguide [114]. To maximise the transmission of microwave power through the coplanar waveguide, the impedance of the device needs to be equal to that of the microwave circuit to which it is connected [115]. Using the website [116] I calculated the thickness and length of the conducting strips and the insulating layers to optimise the impedance of our coplanar waveguide design to match the impedance of the microwave generator at 50 Ω. Two coplanar waveguide designs were generated for our experiments, these are the "linear" and "tapered" waveguides that can be seen in figures 3.11a and 3.11b respectively. In both waveguide designs there is a hole drilled through the centre of the conductive strip. This hole serves two purposes. The first is to allow the back-lighting of samples to allow for bringing the sample into focus on the microscope and sample exploration. The second is it ensures that the copper microwire used to connect the two conductive tracks of the waveguide is the path of least resistance for microwave transmission, resulting in the delivery of the microwave signal to the nanodiamond samples. An example of how the waveguides are set up for ODMR experiments can be seen in figure 3.12.

3.4.1 Microwave Transmission

Before using the coplanar waveguides for ODMR measurements, I wanted to check the power that would be transmitted through the micro-wire and delivered to the sample. The waveguides were placed into the microwave circuit at the sample position and the applied microwave power was recorded at both the input and the output of the coplanar waveguides under two conditions: The first was with no wire attached to the surface of the waveguide, and the second was recorded with a micro-wire (40 µm copper wire) attached to the surface of the waveguide using silver paint to create an electrical connection. The microwave circuit used

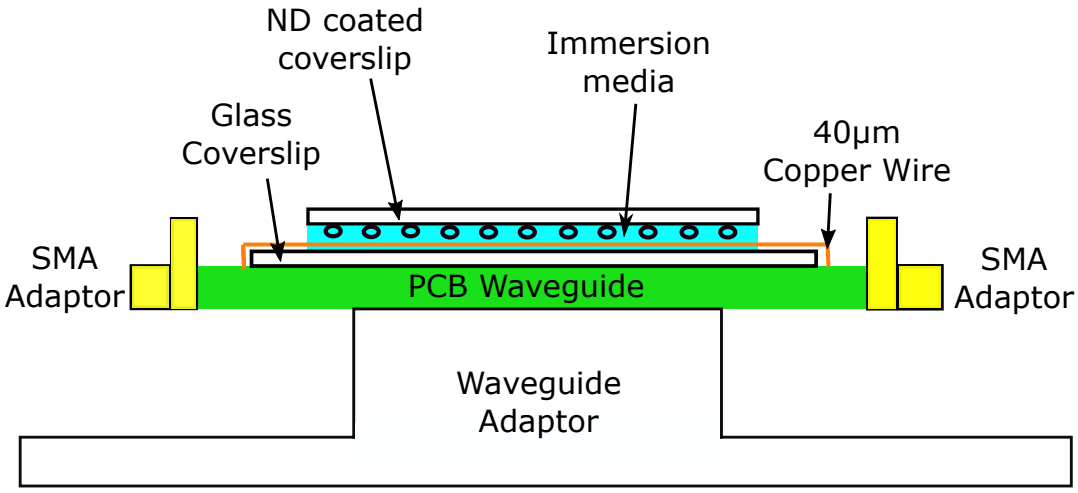

Figure 3.12: A schematic of the sample set-up for using the co-planar waveguides.

for these experiments can be seen in figure 3.13, alongside the measurement of the transmitted power for the three conditions outlined. The microwave power was measured using the PSA3605 spectrum analyser. The microwave power used throughout these measurements was 20 dBm at the output of the microwave amplifier, and the applied microwave frequency range was from 2.75 GHz to 3.00 GHz in steps of 1 GHz.

The results in figure 3.13b show several interesting characteristics of our coplanar waveguides and the microwave circuit as a whole. Firstly, the microwave circuit has a 2 dBm loss between the output of the microwave generator and the input of the waveguides. This loss is consistent with the expected losses for the length of coaxial cables between the microwave amplifier and the sample position in the microwave circuit. The next thing to notice is that there is a significant drop (approximately 12 dBm) between the input microwave power and the transmitted power through the coplanar waveguide and micro-wire. This loss is consistent with the reported efficiency of microwave transmission in microwave striplines [117]. When addressing the literature for microwave strip-lines one finds

that this loss in microwave power is likely to be the result of a combination of some of the signal being back-reflected from the waveguide and the absorption of some of the microwave power by the waveguide itself [113]. The most important finding from these results is that the microwave power transmitted across the waveguide is larger when a micro-wire is used to bridge the air-gap between the two conducting tracks. This is consistent with what we would expect given that the micro-wire offers a low impedance route across the waveguide when compared to the air-gap in the centre of the printed circuit board (PCB).

From these results, we were confident that we should observe an ODMR signal change in the fluorescence intensity from the nanodiamonds when performing ODMR experiments using the coplanar waveguides.

3.4.2 Sample Preparation

Before being able to test the coplanar waveguides we needed to address a couple of the practicalities of implementing the coplanar waveguide solution to for microwave delivery. It is not possible to mount a diamond coated coverslip to the surface of the waveguide with the immersion media present due to the hole in the centre of the waveguide. The solution to this problem was to cover the hole using a larger coverslip (base-coverslip) and mount the diamond coated coverslip on top of this. The larger coverslip (22 mm $\times$ 22 mm) was fixed to the surface of the PCB waveguide using nail varnish applied to each corner of the glass. The copper micro-wire was then attached to the surface of the waveguide using silver paint to create an electrical connection for the microwave signal be transmitted close to the sample. The diamond sample was drop-cast onto a smaller coverslip (12 mm or 18 mm diameter circular coverslip). The immersion media was then placed on the same side of the smaller coverslip as the nanodiamonds. The diamond coated coverslip was the placed, diamond side down, onto the base coverslip, with the

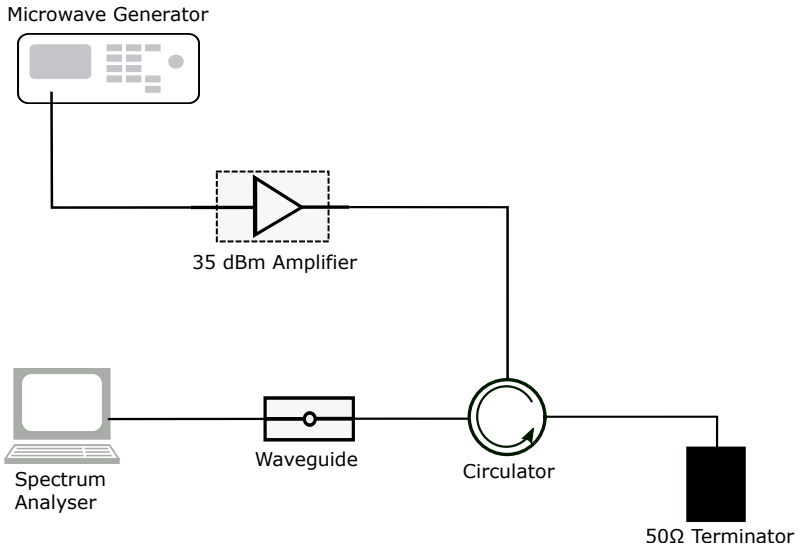

(a)

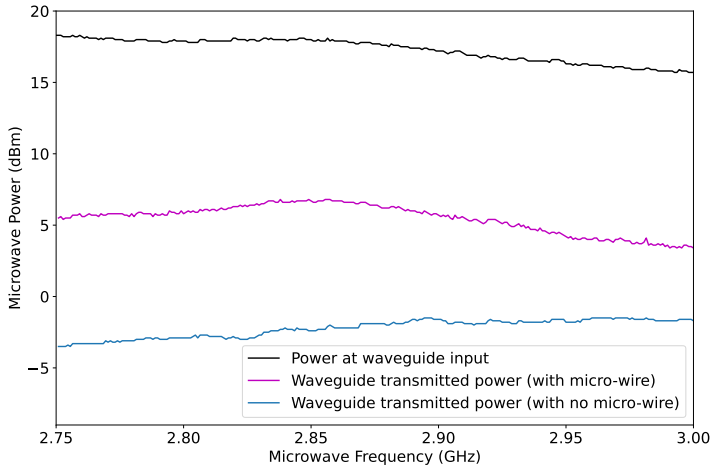

(b)

Figure 3.13: A schematic of the experimental set-up used to measure the transmitted microwave power through a coplanar waveguide 3.13a. In figure 3.13b we can see the measurement of the power supplied to the waveguide (black), The power transmitted through the waveguide with a micro-wire used to bridge the hole in the centre of the waveguide (magenta) and the transmitted microwave power through the waveguide with no micro-wire attached (blue).

micro-wire bisecting the diamond sample. The diamond coated coverslip was fixed to the base-coverslip using epoxy based glue. This configuration is shown schematically in figure 3.12.

Due to the SMA adaptors required for microwave delivery, our samples were also not compatible with our sample stage. To compensate for this, I created a 3D printed sample adaptor that would allow me to mount the coplanar waveguides into the confocal imaging system without needing to create a bespoke sample holder. The sample adaptor had the same dimensions as a glass microscope slide, with a raised plinth in the centre on which the coplanar waveguide could be mounted. This method of sample preparation allowed the coplanar waveguides to be recycled throughout the project, reducing waste and limiting cost throughout the project duration.

3.4.3 Waveguide Performance Analysis

Having created a sample preparation routine that made the coplanar waveguides compatible for imaging within our microscope, I attempted to perform ODMR measurements using the coplanar waveguide and micro-wire antenna for microwave delivery. The samples were mounted onto the waveguide as described in section 3.4.2. For the initial ODMR measurements the experimental parameters were:

- Microwave power after amplification: 20 dBm.
- Microwave frequency scan range: 2.75 GHz to 3.00 GHz with a frequency step of 1 MHz.
- Photon integration time/frequency step dwell time: 5 ms.

The sample used for these experiments was a 90 nm diamond. The distance between the nanodiamond used for these experiments and the microwire antenna

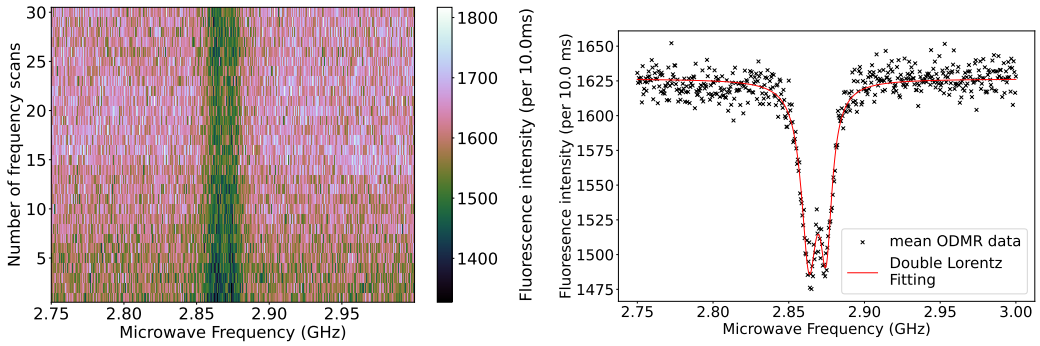

(a) (b)

Figure 3.14: The results of an ODMR measurement performed using the coplanar waveguide and micro-wire antenna for microwave delivery. In figure 3.14a, a repeating pattern can be seen in the heat-map. It is believed that this is a result of the electro-magnetic noise described further in section 3.5.2 . The repeating signal appears to be removed in figure 3.14b which shows the mean fluorescence intensity recorded for each applied microwave frequency.

was determined using the wide-field imaging arm. Using the fast steering mirror (FSM), the laser spot could be moved around the image formed on the wide-field camera. Making use of the speckle observed when the laser was positioned over the microwire antenna, I was able to use the calibration of the FSM to measure the distance between the edge of the mircowire and the nanodiamond used for ODMR. In these experiments, the nanodiamond was positioned 5 µm from the micro-wire. The ODMR heat-map and scatter plot for this measurement can be seen in figure 3.14. The ODMR contrast shown in this figure is 10.8 % which is over double the maximum contrast that was achieved using the double split ring resonator during the microwave power calibration tests preformed in section 3.3.4. This is even more impressive when considering that the microwave power is significantly lower at 20 dBm (100 mW) than was used in the DSRR calibration measurement in which the maximum contrast was achieved using an input power of 35 dBm (3.16W). These results suggest that the micro-wire antenna is significantly more effective at microwave power delivery than the DSRR.

Waveguide microwave power calibration

With the confirmation that the coplanar waveguides were suitable for performing ODMR, I went on to perform a measurement of the power saturation curves for the 90 nm diamond sample. A point-like emitter located 3.5 µm from the wire antenna was selected for these measurement.

This emitter may have contained more than 1 ND, as the nanodiamonds used in this study are smaller than the resolution limit of the microscope. With no method to prevent nanodiamond aggregation during the sample preparation procedure, we cannot say for certain that this is a single nanodiamond.

The microwave frequency scan range was kept constant for the duration of these experiments increasing from 2.75 GHz to 3.00 GHz in steps of 1 MHz with a photon integration time of 10 ms. 50 line scan repeats were used to determine the mean fluorescence intensity for each applied microwave frequency. The microwave power was varied from 39 dBm (7.94 W) to 4 dBm (2.5 mW) in 3 dBm steps (approximately equal to halving the applied microwave power with each step). An ODMR curve was recorded for each of the applied microwave powers used in this study. All measurements were analysed by fitting a double lorentzian lineshape to the data to extract the resonant frequency and the ODMR contrast from the experimental results. The relationship between the ODMR contrast and applied microwave power can be seen in figure 3.15. This measurement showed that the maximum ODMR contrast produced using the coplanar waveguide was approximately 3 times the maximum contrast observed when using the DSRR. The expected saturation behaviour of the ODMR contrast with increase microwave power is also observed. The relationship between the contrast and the microwave power can be described using the following equation:

$$C(P_{\mu Wave}) = \frac{C_{inf}\ P_{\mu Wave}}{P_{\mu Wave}\ +\ P_{Sat}} \tag{3.8}$$

In which the contrast as a function of the applied microwave power $C(P_{\mu Wave})$ can be determined by the product of the maximum possible contrast (C_{inf}) and the applied microwave power is divided by the summation of the applied microwave power and the microwave power required for ODMR saturation (P_{Sat}) [108]. Using the scipy.optimize tool, I was able to fit a saturation curve to the data set, which is denoted by a dashed black line in figure 3.15. From the results of this measurement, I obtained a saturation microwave power of 224 ± 36 mW and a maximum contrast of 15.4 ± 0.6 %.

Upon review of our results, we do not appear to be able to reach the theoretical ODMR contrast limit using the coplanar waveguides [105]. This appears to be a common feature of many ODMR measurements performed using nanodiamond probes [1, 42, 102]. In an investigation by Robinson *et al*, this loss in ODMR contrast from nanodiamonds in comparison to bulk diamond was attributed to a decrease in the fluorescent lifetime of the defect centre and to changes in the emission spectra [118]. Using the coplanar waveguide, I was consistently able to achieve an ODMR contrast above 10 % which was a significant improvement on the results of experiments performed using the double split ring resonators.

From literature we know that the 40 µm wire microwave antenna is not able to project a uniform microwave field over a wide area [104]. The next step in the characterisation of the micro-wire antenna was to see over what range we were able to produce a consistent ODMR signal from NV^- ensembles within the 90 nm diamond crystals.

ODMR Contrast vs Distance from Micro-Wire

To further investigate the suitability of the coplanar waveguides with a micro-wire microwave antenna for ODMR measurements, I investigated the distance

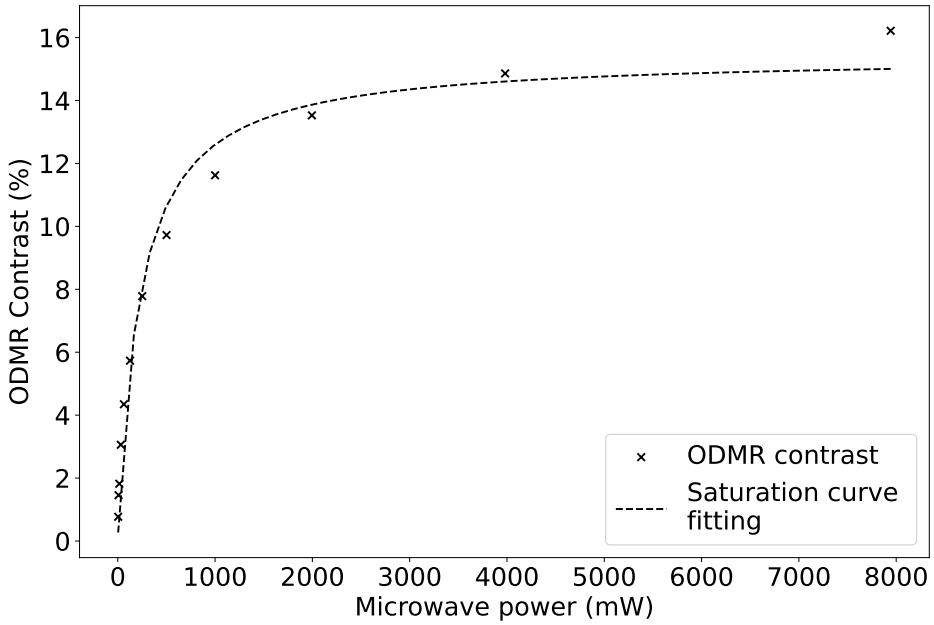

Figure 3.15: A plot showing the ODMR contrast as a function of applied laser power for a sub-diffraction limited cluster of 90 nm diamond. A saturation curve has been fitted to this data to simulate the relationship between the applied microwave power and the ODMR contrast.

from the micro-wire that a consistent ODMR signal is observed. The aim of this experiment was to get an idea of the total area of the sample that can be used for magnetic-field or temperature sensing.

Two separate measurements were performed to try to quantify the distance from the micro-wire that the ODMR contrast starts to drop off. For the first measurement a 90 nm nanodiamond sample was prepared for ODMR measurements using the procedure outlined in appendix A.2. The frequency scan was performed between 2.75 GHz and 3.00 GHz with a 1 MHz frequency step and a photon integration time of 10 ms. The microwave power was fixed at 39 dBm at the output of the microwave amplifier. The nanodiamond sample was positioned using the stepper motors and the wide-field camera. The sample was positioned so that the microwire was at one extreme of the FMS scan range, allowing me to investigate nanodiamonds up to 40 µm from the wire without requiring a shift in sample position. This was done by setting the initial FSM position to one extreme (eg: $+20$ µm) and moving the sample until the speckle from the laser hitting the micro-wire could be seen. I was then able to monitor the consistency of the ODMR contrast across the 40 µm field-of-view offered by the fast steering mirror. I was then able to determine the distance of the nanodiamond under study from the microwire by reading off the position from the FSM. The results of this measurement can be seen in figure 3.16, and show that over a 35 µm range from the micro-wire the ODMR contrast appears to be very consistent with almost all of the ODMR contrast measurements contained within a single standard deviation of the mean ODMR contrast (10.8 %) recorded.

The second measurement was performed using a 40 nm diamond sample. The change in sample offers no change to the experiment except that these crystals contain just 10 NV^- centres per crystal, compared to the 500 NV^- defects present

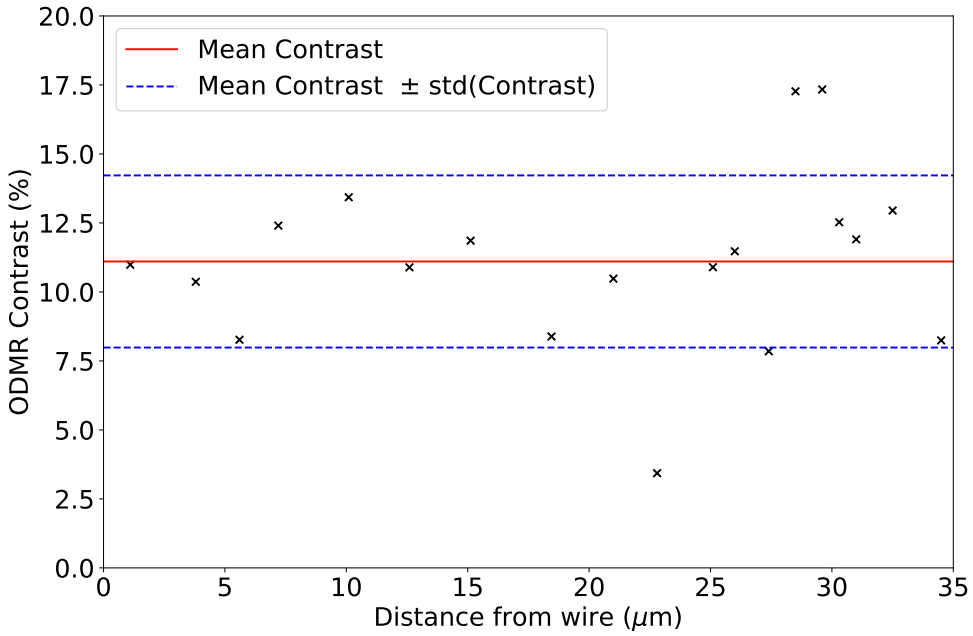

Figure 3.16: A measurement of the consistency of the ODMR signal recorded from a 90 nm diamond sample. Measurements were recorded from point-like emitters at increasing distances away from the micro-wire antenna.

in the 90 nm samples. A new coplanar waveguide was used for these measurements and the resolution of the frequency sweep was increased to 0.5 MHz steps. All other scan parameters remained the same between the two measurements. In this second measurement, the zaber stepper motors were used to explore the ODMR contrast produced at distances up to 60 µm from the micro-wire. The results of this experiment are seen in figure 3.17. Over the 60 µm range we can see that the ODMR contrast does decrease as the distance from the micro-wire increased. This trend becomes more pronounced when using the moving average across 5 measurements points (red circles in the plot). I have used a linear fitting algorithm to describe the decrease in ODMR contrast across the measurements. The gradient of this line is m = -0.05 ± 0.02 % per micron. Given that the y intercept of the graph is at 7.7 %, from this plot, we would expect to see a 50 % reduction of the ODMR contrast at a distance of 77 µm from the micro-wire. These experiments have been expanded on with the introduction of ODMR to wide-field imaging techniques currently being conducted in the research group. These experiments are showing that ODMR contrast can be reliably observed as far as 200 µm from the micro-wire antenna.

3.5 Optimisation of ODMR Performance

The coplanar waveguides provided a promising platform from which to expand upon the ODMR measurements performed. During the development of the ODMR system I identified some key factors that have been shown to effect the maximum contrast from an ODMR measurement. Some of these have already been reported in this work, such as the distance from the micro-wire antenna, or the microwave power applied. In the following sections, a further discussion the key parameters for the performance of ODMR measurements is presented.

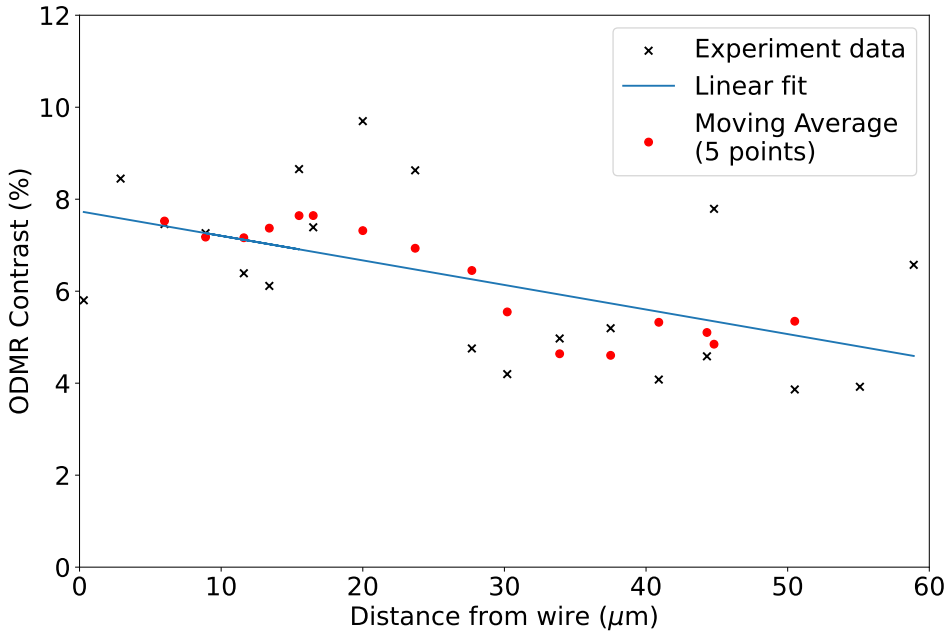

Figure 3.17: The relationship between the ODMR contrast recorded and the distance of 40 nm diamonds from the micro-wire antenna over a 60 µm range.

3.5.1 Microwave Power

In section 3.4.3, I showed that as the microwave power was increased, the ODMR contrast from the NV^- centre increased following a saturation relationship [28]. One might assume from these results alone than it would be best to apply as much microwave power as possible in order to achieve the maximum ODMR contrast for sensing. With the application of increasing microwave power, however, we also see an increase in the full width half maxima (FWHM) of the Lorentzian lineshapes used to describe the ODMR data. This occurs as a result of microwave power broadening [119]. An example of this power broadening can be seen in figures 3.18a and 3.18b, which show the ODMR spectra from the same 90 nm nanodiamond with the applied microwave power set to 251 mW and 3981 mW respectively. While the increase in the applied microwave power has almost doubled the ODMR contrast observed, the FWHM of the measurement has increased to the point that is it difficult to distinguish the two ODMR dips. I was able to investigate the effect of increased microwave power on the FWHM of the ODMR dips using the same dataset that was used to characterise the saturation behaviour of the ODMR constrast with increased microwave power in section 3.4.3. The results of this investigation can be seen in figure 3.18d, and show that the FWHM of the Lorentz fitting used to model the results of the ODMR data increased linearly with the square root of the applied power, a relationship consistent with that published in literature [120].

In their review paper, Radtke *et al* highlighted the importance of balancing the FWHM and the ODMR contrast to achieve the optimum DC magnetic field sensitivity [44]. The calculation used for the sensitivity (η_{DC}) of the NV^- ensemble is reported as:

$$\eta_{DC} = \frac{h}{g\ \mu_B}\ \frac{\Delta f}{\sqrt{I_0}\ C}. \tag{3.9}$$

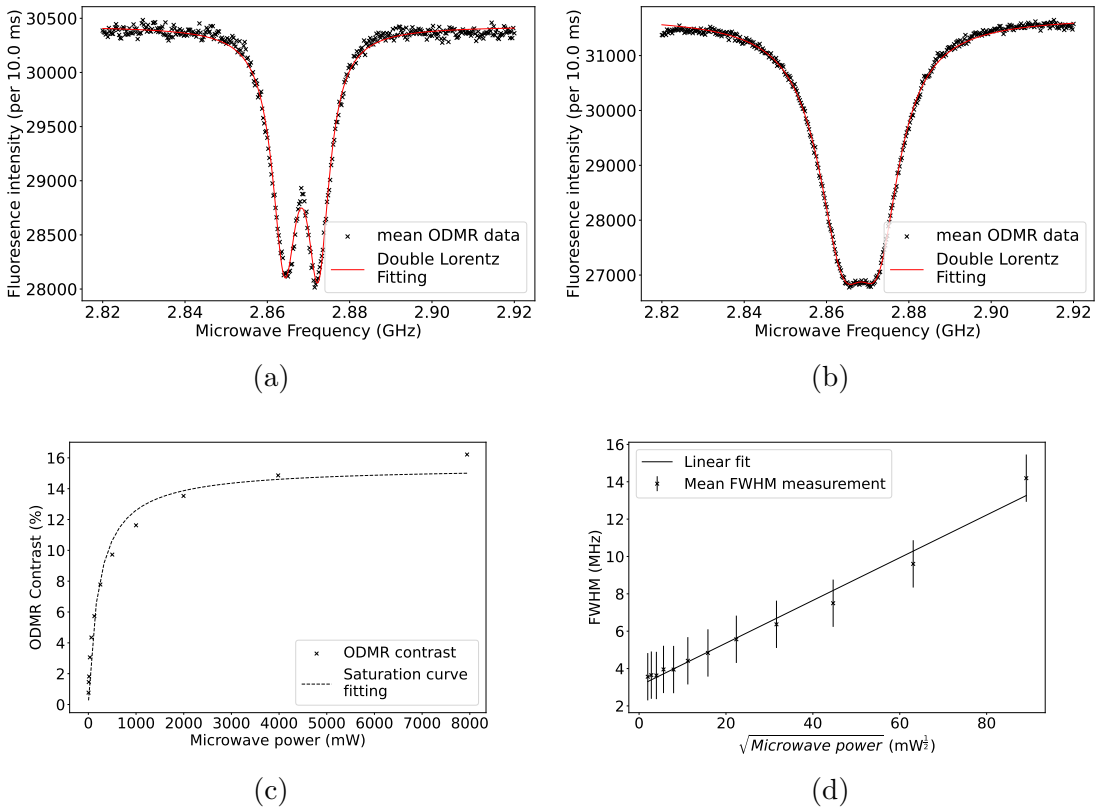

Figure 3.18: A demonstration of the effects of the microwave power broadening in the ODMR measurements recorded from a 90 nm diamond sample. Figures 3.18a and 3.18b show the ODMR spectra from the same nanodiamond with an applied microwave powers of 251 mW and 3981 mW respectively. The mean ODMR contrast function of the applied microwave power is plotted in figure 3.18c and the FWHM for the double-Lorentz fitting as a function of the square root of the applied microwave power is plotted in figure 3.18d.

In which g, h and μ_B are the Landé factor, Planck's constant and the Bohr magneton respectively. Δf is the FWHM of the Lorentzian lineshape, I_0 is the off-resonant fluorescence intensity of the measurement, and C is the ODMR contrast [44]. From this equation we can see that the DC magnetic sensitivity of the NV^- ensemble is linearly dependant on the FWHM of the ODMR dip, and, inversely proportional to the ODMR contrast of the measurement. Therefore, in order to optimise the sensitivity of the nanodiamond probe, the microwave power needs to be chosen carefully to maximise the contrast without compromising the line-width of the Lorentz fitting. In figure 3.19 we can see the sensitivity of the 90 nm diamond probe used in the above experiments changes as a function of the applied microwave power. The maximum sensitivity observed from these measurements is $1.13 \pm 0.04\,\mu T/\sqrt{Hz}$, with an applied microwave power of 1 W (30 dBm). Once the microwave power exceeded 1 W, the sensitivity of the probe started to decrease. This can be understood by figures 3.18c and 3.18d. Once the applied microwave power was greater than 1 W, the increase in the FWHM of the ODMR curve increased more with applied microwave power than the measurement contrast. As a result, the DC magnetic sensitivity of the NV^- ensemble starts to degrade. These results highlight the need to consider the appropriate microwave power required to optimise the sensitivity of the nanodiamond probes when performing magnetic-field or temperature sensing experiments.

3.5.2 Drift and Length of Scan

One of the major factors that affects our ability to perform ODMR measurements is the stability of the sample throughout the ODMR measurement. To be able to perform a successful ODMR measurement using the confocal microscope the sample needs to stay within the focal spot of the microscope. We have been able to show that the microscope has the potential to be suitably stable over 12.5 minutes. Figure 3.20 shows the results of an ODMR measurement in which the

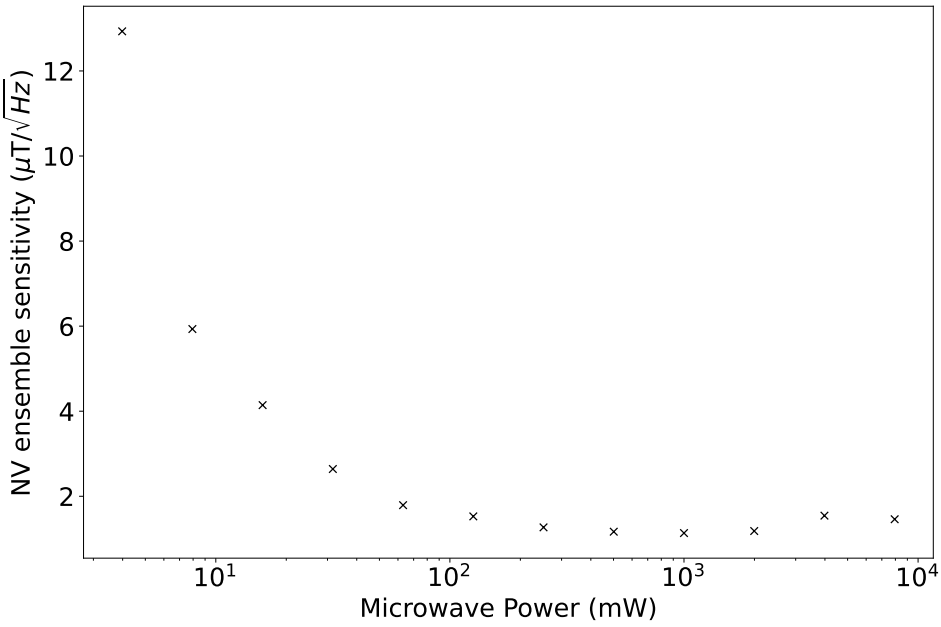

Figure 3.19: A measurement of the sensitivity of a 90 nm diamond probe to DC magnetic fields as a function of the applied microwave power.

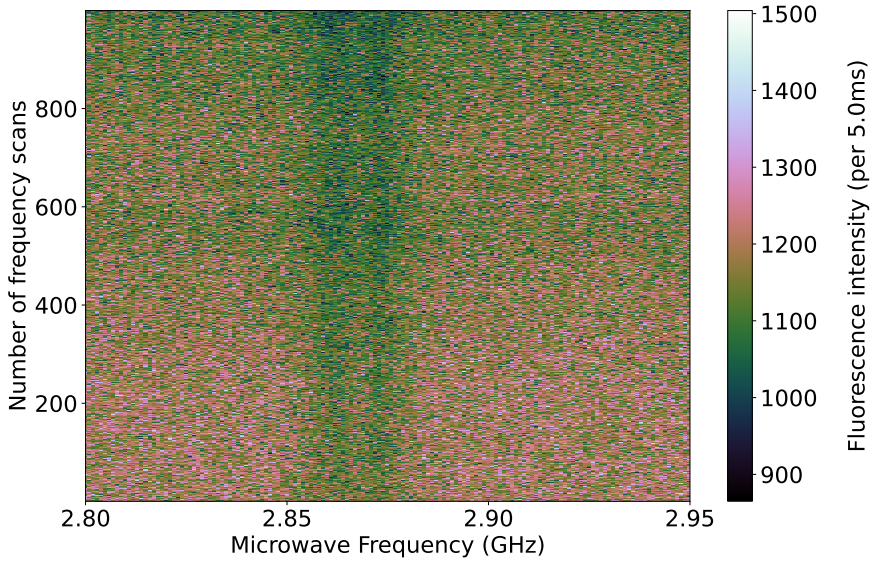

Figure 3.20: A graph showing 999 ODMR line scans performed over a 12.5 minute time period. The total loss of mean counts between the first and last line scan was 100 counts per 5ms (9% loss of fluorescence).

999 frequency line scan repeats were performed. Over the course of the 12.5 minutes ODMR scan, the mean fluorescence intensity per line scan only dropped by 9%. When the microscope was this stable the only consideration for NV^- sensing experiments would to ensure a high enough photon flux to observe the drop in fluorescence intensity as the ODMR measurement is performed.

One of the unexpected challenges I encountered during this project was the coupling in of electro-magnetic noise from the building supply into the control of the microscope objective position. The physics department at the University of Strathclyde houses the SCAPA high powered laser system (350 TW) [121]. We found that, when operational, the repetition rate of the laser could be seen within the electrical infrastructure of the John Anderson building in the form of electrical noise. This electrical noise was coupled into our experiments through the PiFOC piezoelectric objective mount. This caused the objective to "jump" by a few tens of nanometers with each oscillation, significantly effecting the stability of our

ODMR and confocal imaging experiments. An example of the effect of the electro-magnetic noise from the SCAPA laser system into our microscope imaging arm can be seen in figure 3.21. When this electro-magnetic noise was present in our microscope, we were limited to proof of principle experiments as the microscope is not stable enough for confocal imaging or accurate ODMR measurements. We were eventually able to separate the SCAPA laser power supply from the building and remove the electro-magnetic noise from our measurement system. In total, the noise was present in our microscope system for approximately 18 months, not including the time the university was closed due to the COVID-19 global pandemic.

3.5.3 Laser Power

As discussed in section 3.5.1 one way to increase the sensitivity of the nanodiamond probes is to improve the signal to noise ratio of the ODMR measurement [44]. One can increase the fluorescence intensity from the NV^- ensembles in bulk diamond by increasing the laser power applied to the sample. This will result in more frequent optical excitation of the NV^- centres within the nanodiamond crystals and therefore an increase in the fluorescence emission rate [28]. As the ODMR measurements are based upon the spin-dependent fluorescence intensity of the NV^- centre, we would expect that the sensitivity of the NV^- magnetometer would increase as the optical excitation power is increased, as described by equation 3.9 [44]. To test this I performed an experiment in which the ODMR contrast from a 40 nm diamond was tracked as a function of the applied laser power. The laser power was measured from the output of the single mode fibre coupling in the 532 nm laser into the common path of the microscope. The microwave power used for these experiments was 39 dBm (3.16 W) at the output of a +40 dBm amplifier. The results of this experiment can be seen in figure 3.22.

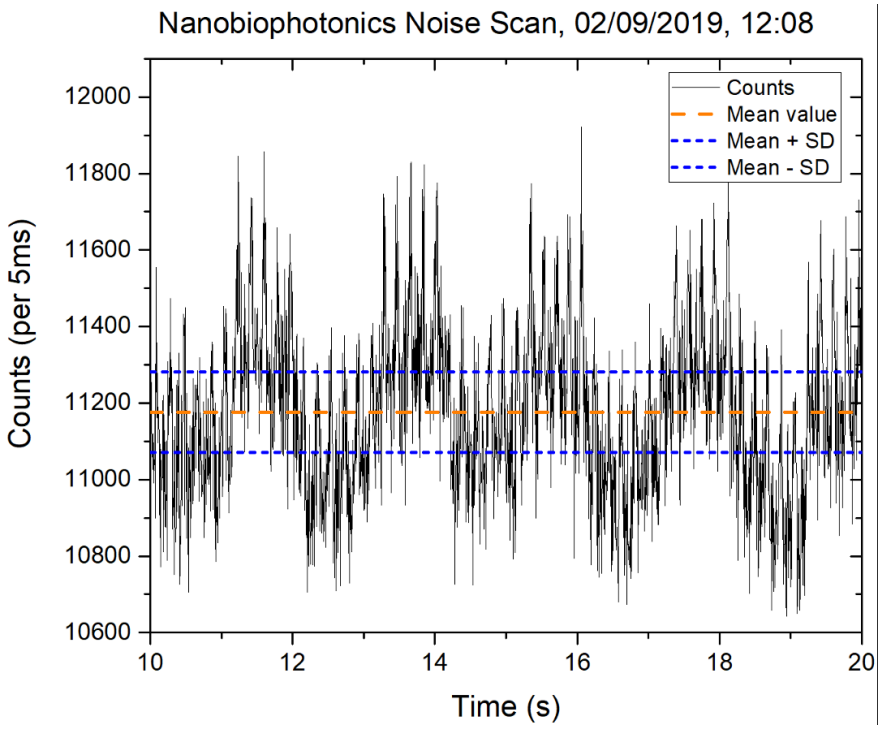

Figure 3.21: Here I present the electro-magnetic noise from the John Anderson building in which our microscope is housed. Super-imposed on the dataset are the mean fluorescent signal over the time period (orange dashed line) and the bounds for the shot-noise error that we would expect for the fluorescence intensity detected (two blue dashed lines). The noisy signal recorded from the nanodiamond falls well outside the normal operating range of the microscope. Figure credit: Brian Patton.

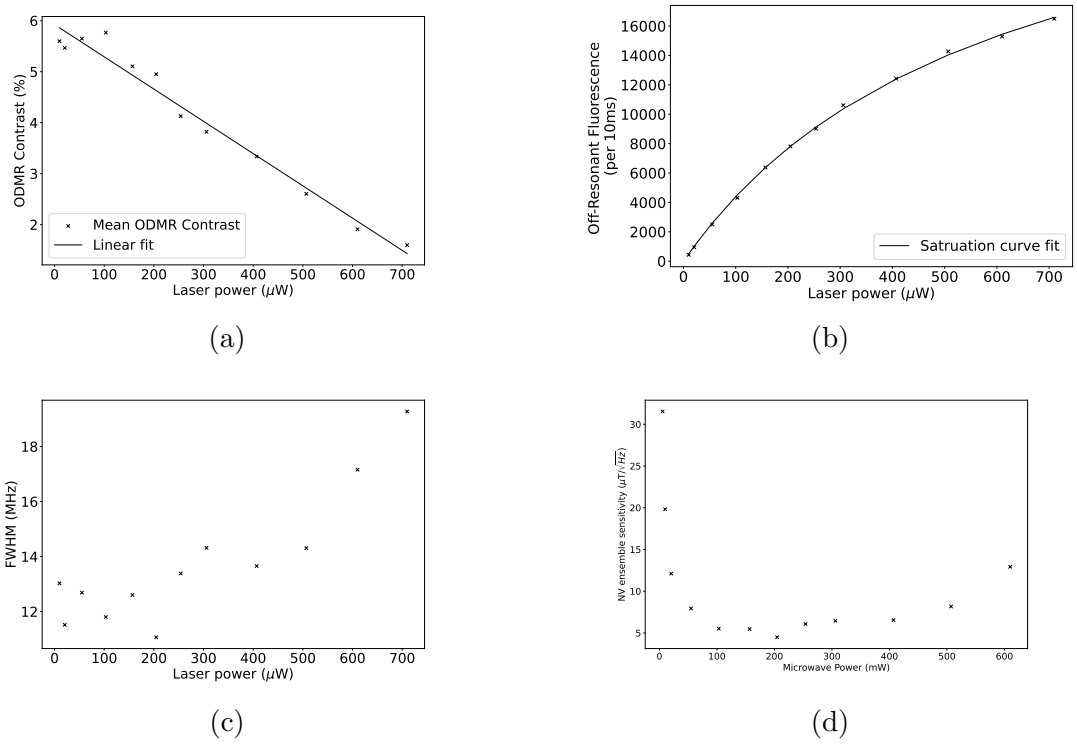

Figure 3.22: The response of the ODMR spectra from a 40 nm diamond as the laser power applied to the sample was increased. In figure 3.22a, the ODMR contrast as a function of applied laser power is shown. Figure 3.22b details the increase in the fluorescence intensity recorded from the nanodiamond as the laser power was increased. Figure 3.22c shows the response of the FWHM of the ODMR measurement to the increased laser power, and figure 3.22d details the change in the sensitivity of the nanodiamond sensor as the laser power is increased.

In figure 3.22a the ODMR contrast is plotted as a function of the laser power applied. Interestingly, the results show that as the laser power is increased, the ODMR contrast observed appears to decrease. A linear fit was used to model the drop in the ODMR contrast as a function of laser power and showed that the contrast dropped by $0.0063\% \pm 0.0003\%\,\mu W^{-1}$ of applied laser power. This was not the relationship that I was expecting to see from these results. Moreover the decrease in ODMR contrast with increasing laser power has been seen in our system across multiple measurements and multiple samples/nanodiamonds. After consulting the literature, I found that this phenomena had been previously reported, [122, 123], and has been attributed to the optical cycling between the NV^- electronic energy levels being faster than the resonant driving of the spin-state transitions. As a result, as the applied laser power is increased for a fixed microwave power, the ODMR contrast decreases.

In figure 3.22b, we can see that the off-resonant fluorescence intensity of the NV^- ensemble does not increase linearly with applied laser power, and indeed begins to approach a saturation value as the laser power is increased. These results suggest that with the increased laser power, we are beginning to saturate the electronic transitions of the NV^- centre [123]. We can see the combined effect of the increase in the fluorescence intensity from the ND and the reduction of the ODMR contrast on the sensitivity of the NV^- ensemble in figure 3.22d. As the laser power is increased from $5\,\mu W$ - $205\,\mu W$ the signal to noise ratio of the ODMR measurement increases due to the increased fluorescent emission. With an applied laser power of $205\,\mu W$, the DC magnetic sensitivity of the NV^- ensemble increased to a maximum of $4.8 \pm 0.8\,\mu T/\sqrt{Hz}$. As the laser power is increased further, the FWHM of the measurement starts to increase (see figure 3.22c) and the contrast starts to decrease to the detriment of the ND probe sensitivity. From these measurements, it is clear that the laser power applied to a nanodiamond

probe needs to be carefully considered to maximise the sensitivity of the NV^- probe.

3.5.4 ND Size

Throughout this research project, I have used commercially available nanodimaond samples. Coming from two different manufacturers (Adamas and Sigma Aldrich) I had access to four different sizes of nanodiamond that were stored as a colloidal, these samples were:

- Adamas - 20 nm, $\approx 1\,NV^-$ centre per crystal.
- Adamas - Biotin coated 40 nm, $\approx 10\,NV^-$ centre per crystal.
- Sigma Aldrich - 70 nm, $\approx 100\,NV^-$ centre per crystal.
- Sigma Aldrich - 90 nm, $\approx 500\,NV^-$ centre per crystal.

Apart from the size of the diamond, the other major difference between the nanodiamonds that I have been using is the quantity of NV^- defects within each crystal. Using nanodiamonds with a small number (1-10) of NV^- defects in the crystal gives the advantage that the full width half maxima of the ODMR spectra should be limited to homogeneous broadening [98]. If we assume that the ODMR contrast is constant across all nanodiamond samples used (none of our experiments led us to believe otherwise), then these nanodiamonds would produce a steeper gradient in the ODMR spectra for magnetic and temperature sensitivity measurements than the larger NV^- ensembles [44]. The larger ensembles do have a significant advantage in the fluorescence intensity from the diamond per unit laser power over the smaller ensembles. This has a significant effect on the sensitivity of the ODMR measurements as sensitivity is proportional to $\frac{1}{\sqrt{I}}$ [44]. In section 3.5.3, I showed how an increase in applied laser power can result in a reduction in the overall contrast of an ODMR measurement [122, 123]. Therefore,

by having a larger number of NV^- centres present in the crystal the increased fluorescent signal might be of greater significance in the calculation of sensitivity than any losses due to linewidth broadening due to spin-mixing [98]. It is noted that we would expect to see the quantity of NV^- centres in the nanodiamond crystals to vary from crystal to crystal as NV^- centre generation on this scale is a random process, although efforts are being made to achieve deterministic NV centre generation [124]. We would therefore expect to see that the nanodiamonds used in this study would have a number of NV^- centres normally distributed about the mean number of expected defects within the crystal. In the case in which we are working with nanodiamonds with ≈ 10 NV^- centre per crystal, this random distribution of defects would make it difficult to determine if there was a single crystal under investigation, or if the point like emitted in the focal volume of he microscope was a small cluster of two or three NDs. The random distribution of NV^- centres throughout the diamond crystals also makes it very difficult to directly compare multiple nanodiamonds from the same experiment, as they may not only have a different number of NV^- defects within their structure, but these will likely be orientated differently to the applied microwave and magnetic fields during an ODMR experiment due to the uncontrollable nature of the orientation of the nanodiamonds on the surface of the glass coverslips/within biological samples. This is something that needs to be remembered when choosing a nanodiamond for use in an sensing experiment.

3.6 Thermometry

One of the aims of this research project was to use the temperature dependency of the resonant frequency of the NV^- centre for thermometry experiments, with the long term goal of monitoring temperature changes within live-cell samples. In their work, Acosta *et al* identified that the resonant frequency of the NV^-

centre is linearly dependant on temperature changes around room temperature [37]. This is thought to be the result, at least in part, to thermal expansion of the diamond lattice reducing the strength of the electron-electron interaction which causes the zero-field splitting [105].

The addition of an environment chamber would allow us to maintain a viable environment for live-cell cultures to survive the imaging process without the temperature affecting normal cell function [125]. For this purpose we brought an Oko-Labs 301-H temperature stage. The temperature stage came complete with: a thermal stage, a heating collar for the objective, an environment chamber and a temperature probe. The majority of the components could be seamlessly added to our bespoke imaging system. Due to the coplanar waveguides and the sample adaptors needed for ODMR measurement, however, I had to create a new 3D printed environment chamber in order for us to use the temperature stage effectively. The microscope sample chamber with the Oko-Labs temperature stage and the 3D printed environment chamber can be seen in figure 3.23.

In the following section I will discuss the initial experiments that were conducted to assess the performance of the temperature stage for ODMR and temperature sensing experiments. The initial tests of the sample stability and the first ODMR experiments were performed working alongside Dr Greame Johnstone. The CW ODMR thermometry experiments were performed independently as was the data analysis.

3.6.1 Testing the Temperature Stage Stability

Before we could perform NV^- based temperature sensing, I first had to assess the suitability of the temperature stage for our ODMR measurement protocols. In these measurements I wanted to assess the limits of the temperature stage's

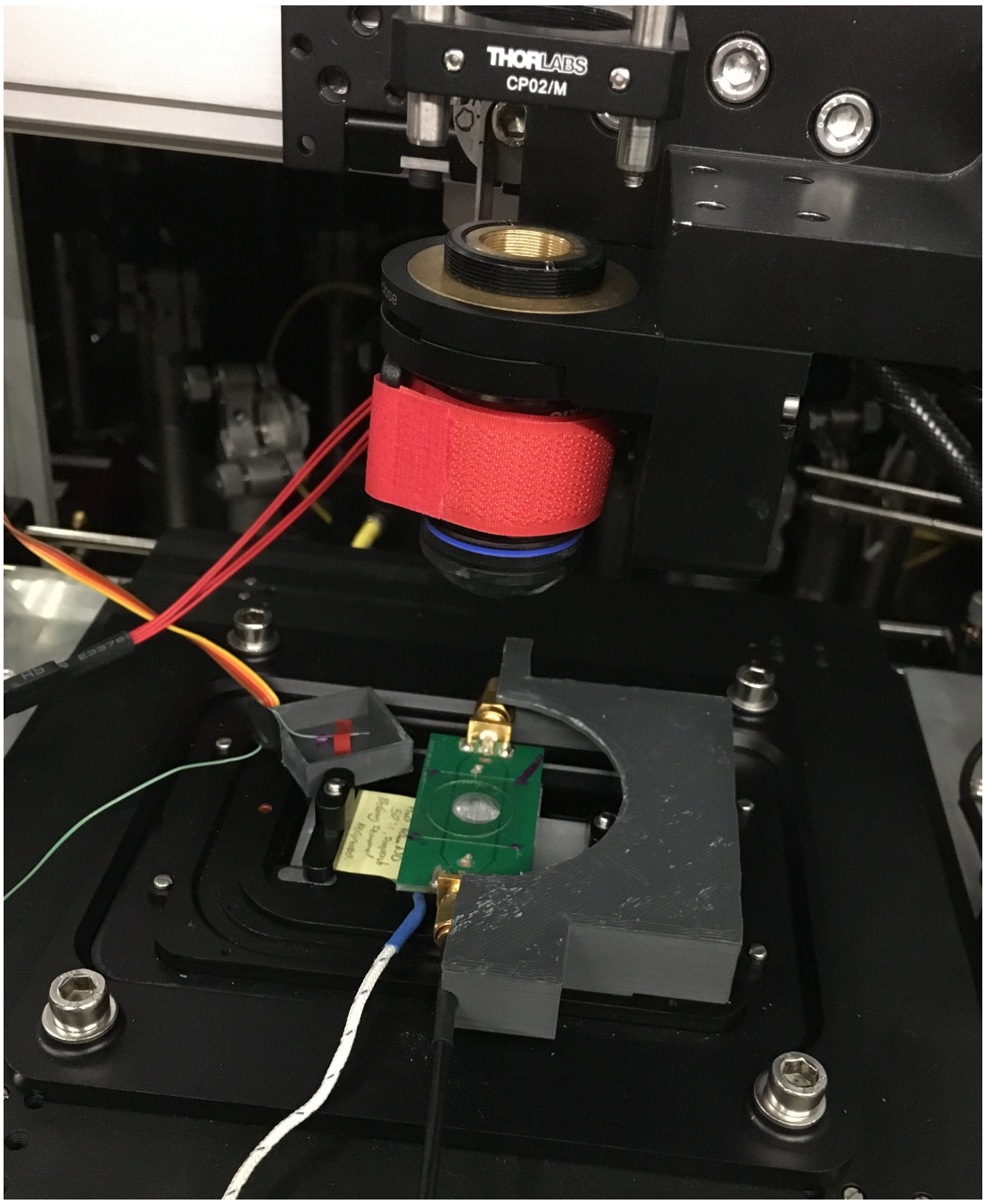

Figure 3.23: An image of the set-up of the microscope sample chamber when using the Oko-Lab temperature stage.

performance. To this end, I wanted to know: the maximum temperature we were able to maintain in the 3D printed environment chamber, how long it took for temperature stability to be achieve and, finally, how the stability of the microscope was affected when the temperature stage was in operation. To perform these measurements a 70 nm diamond sample, prepared using the method described in appendix A.2, was mounted on a tapered coplanar waveguide and installed within the environment chamber. The control unit for the 301-H temperature stage has an LED that is used to indicate the stability of temperature within the sample chamber as been achieved. The temperature within the chamber was monitored using the temperature probe included in the sample stage package. A control feedback loop was used to maintain temperature in the environment chamber and stability in the environment chamber is achieved when the temperature variation is within 0.1°C of the target temperature. When temperature stability is achieved, the LED on the control box turns from orange to green.

From these measurements, we found that it took about 5-8 minutes for the temperature in the environment chamber to reach 0.5°C of the desired temperature, and a further 20-30 minutes for the temperature to stabilise within 0.1°C of the target temperature. The maximum temperature that could be maintained within the environment chamber was 45°C in these tests using the 3D printed environment chamber. 45°C is far beyond what is required for live-cell imaging, so from this respect, the temperature stage should be suitable for live-cell imaging. While these calibration measurements were being performed, the stability of the nanodiamond sample was also being monitored. The piezoelectric objective controller was used to determine the axial position of the sample as the temperature was varied from 30°C to 38°C in steps of 2°C. The results of the measurement can be seen in figure 3.24. From these measurements, we can see that the sample moved more than 20 µm axially over the course of these measurements. This

axial drift presents a problem for biological imaging and NV thermometry within our confocal microscope as the drift per degree Celsius temperature change is larger than the axial resolution of the microscope. The sample therefore moves out of the field of view each time a temperature change was applied. What is more troubling from the point of view of implementing this temperature stage for biological imaging/sensing are the drift dynamics that occur with each temperature step. Within the first 30 s of a change in temperature, the sample would suddenly undergo a very fast axial drift. This drift was so severe that the sample would drift out of the focal plane of the microscope, meaning the sample needed to tracked manually as each temperature step. Following a change in temperature, the sample required a settling time of approximately 1 hour, such is the severity of the drift in the system. The drift dynamics of the sample due to a changes in temperature present a possible serious limitation in the application of the Oko-Labs temperature stage for bio-sensing experiments.

3.6.2 ODMR using the Temperature Stage

The Oko-Labs sample stage and the pins used to hold the sample in position on the microscope all contain magnets. From equation 3.1, we would expect to see further splitting of the $|\pm 1\rangle$ spin states of the NV^- centre due to the interaction of this magnetic field with the NV^- centre, this is called the Zeeman effect [90]. Additionally, we would expect the different orientations of the NV^- to experience different amounts of Zeeman splitting as the magnetic field has a different alignment relative to each of the NV^- axis in the crystal. The magnitude of the Zeeman effect in diamond is given by:

$$\Delta E = \mu_b g_e \mathbf{B} \cdot \mathbf{S} = \mu_b g_e B_{NV} S_{NV} \cos\theta. \tag{3.10}$$

where θ is the angle between the applied magnetic field and the NV^- dipole

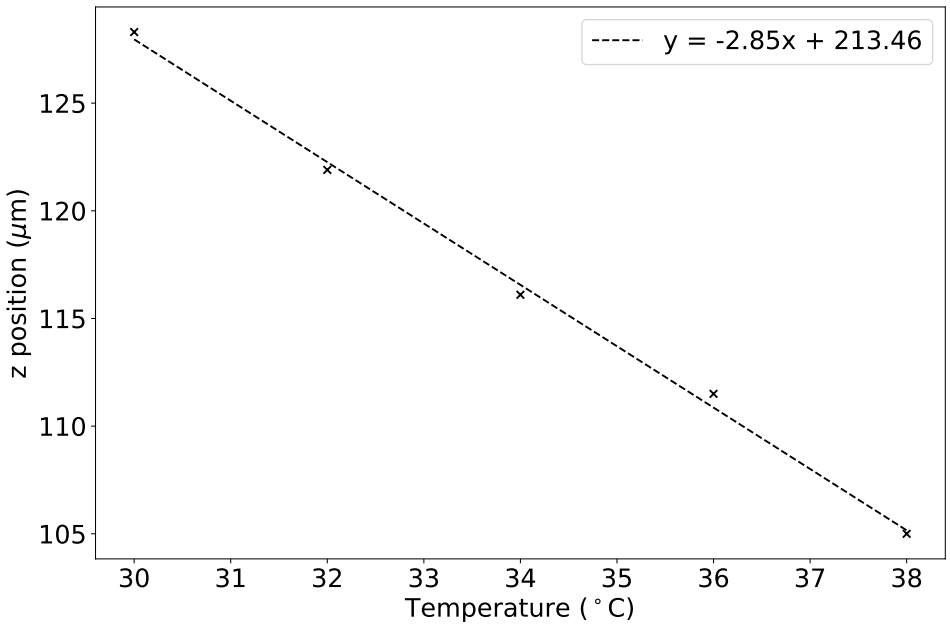

Figure 3.24: Here the axial drift in the sample position relative to the microscope objective as the temperature within the Oko-Labs environment chamber was changed.

moment, which is aligned to the crystallographic bonds within diamond [90].

The aim of these measurements was to see whether the effects of the magnetic field from the sample stage was enough to introduce Zeeman splitting to the ODMR measurement. This would manifest itself in the ODMR spectra as up to 4 distinct pairs of ODMR dips, corresponding to the 4 crystallographic orientations of the NV^- centre in diamond [90].

I performed a series of experiments to see if I was able to detect the effects of the induced Zeeman splitting from the magnets on the sample stage using our ODMR measurement protocol. A 90 nm diamond sample was used for these experiments, the sample was prepared as in figure 3.12. The experimental parameters used for this experiment were:

- Microwave power: 36 dBm at the output of the microwave amplifier.
- Microwave frequency scan: 2.75 GHz to 3.00 GHz in steps of 1 MHz.
- Photon integration time/frequency dwell time: 10 ms.

The results of this measurement can be seen in figure 3.25, and show that the magnetic field from the sample stage is indeed strong enough to introduce Zeeman splitting in the ODMR measurement. This ODMR spectra can be understood by considering that 3 of the NV orientations having an orientation within the diamond closer to perpendiclar to the magnetic field generated by the temperature stage. As a result, these NV orientations experience a smaller applied Zeeman splitting that the one NV orientation angled closer to parallel. See figure 3.1 as a visual guide to the change in energy levels that occurs as a result of NV orientation relative to an applied magnetic field.

The maximum projection of the magnetic field on the NV^- axis is 1.46mT. This presents a complication when performing ODMR thermometry using our

nanodiamond samples. As the nanodiamond crystals are deposited onto the surface of the coverslip, we have no control over their orientation. This means that any possible orientation of the NV^- ensembles relative to the applied magnetic field from the temperature stage is possible. Therefore, when using the Oko-Labs temperature stage for ODMR measurements, we will need to search for:

- A diamond that lies close enough to the micro-wire antenna for a strong ODMR signal to be observed.
- A ODMR spectra that is symmetrical around the zero-field resonant frequency of the NV^- centre.
- A diamond that is orientated in such a way that the magnetic field from the temperature stage produces clearly defined ODMR dips, such as is seen in figure 3.25b.

These criteria only limit the number of NDs that can be considered viable candidates for temperature sensing using ODMR. With the number of nanodiamond crystals that are deposited over the surface of the coverslip during the sample preparation, there will always be nanodiamonds within the sample that fulfil these requirements for ODMR measurement/temperature sensing. One way to mitigate against the complexity introduced by the magnetic field from the temperature stage would be to include a 3D Helmholtz coil [126] or an electromagnet able to produce a 3D magnetic field orientated in any direction [127]. This would not only allow for the magnetic field from the temperature stage to be compensated for, but would also allow an applied magnetic field to be preferentially aligned to one of the NV^- orientations. This would have the benefit of reducing the inhomogeneous broadening (FWHM of ODMR dips) brought about due to the spin-mixing between NV^- centres within an ensemble, as only NV^- centres with the same orientation relative to the magnetic field could contribute

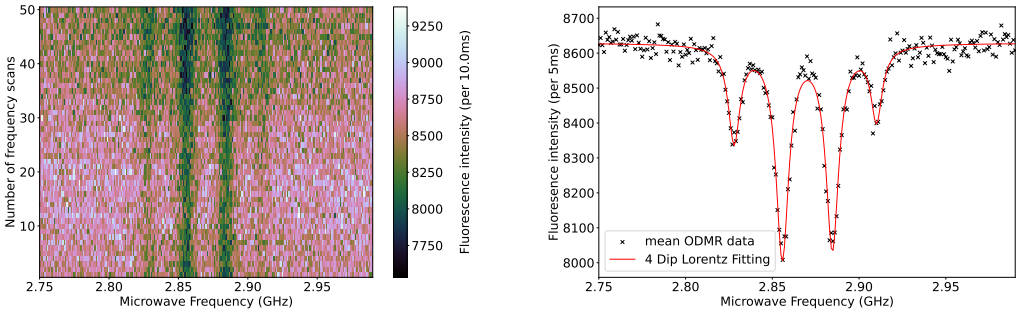

(a) (b)

Figure 3.25: The results of the ODMR measurement recorded from a 90 nm diamond sample mounted within the Oko-Labs climate chamber. A heat-map is shown in figure 3.25a to illustrate the stability of the measurement. The scatter plot shown in figure 3.25b shows the mean fluorescence intensity recorded from each of the applied microwave frequencies and the Lorentz fitting to each of the ODMR dips.

to the ODMR dip observed [128]. This may come at a cost of the ODMR contrast, however, as at least 1 crystallographic bond in the diamond will not have the same orientation to an applied magnetic field. Thus the total drop in fluorescence from the NV^- ensemble throughout an ODMR measurement will not be as pronounced were no magnetic field present at all. With the ability to control the orientation of the applied magnetic field, such effects can be minimised, but not removed [129].

3.6.3 CW ODMR Temperature Sensing

Having installed and suitably tested the Oko-Labs 301-H temperature stage, I attempted to monitor changes to the resonant frequency of the NV^- centre within nanodiamond crystals as the temperature within the sample stage was varied. For these experiments, a 70 nm diamond sample was used for temperature sensing, mounted upon a tapered coplanar waveguide, with the 40 µm copper micro-wire used for microwave delivery. The microwave power used for these experiments was

35 dBm at the output of the microwave generator and the microwave frequency scan range was 2.75 GHz to 3.00 GHz. The frequency step for these measurement was 1 MHz and the photon integration time/frequency dwell time was 1 ms.

From the previous experiments using the temperature stage, we know that there is a large amount of rapid sample movement when a temperature change is initiated. I therefore sought to identify a region of the sample with a distinct shape/feature within it. Using this distinct feature I could refocus the sample after each applied temperature step and return to the nanodiamond(s) used for the temperature sensing experiments. Use of the same nanodiamond(s) is important to determine the temperature dependency of the resonant frequency of the NV^- centre. An example of the ROI selection can be seen in figure 3.26.

With a suitable region of interest identified, I selected a nanodiamond for use in these experiments that had a symmetrical ODMR spectra and a contrast of over 5%. The ODMR spectra from the diamond chosen for these experiments can be seen in figure 3.27. To improve the accuracy of the NV^- defect thermometry measurements, I recorded three ODMR spectra from the nanodiamond for each of the applied temperature changes. From these measurements, I was able to find the mean change of the resonant frequency of the NV^- centre for each of the applied temperature changes. The experiment procedure was as outlined below:

1. An initial set of three ODMR spectra were recorded from the nanodiamond of interest at room temperature (27°C, as recorded using RS PRO - 1231841 digital thermometer).

2. The Oko-Labs temperature stage was switched on and the temperature within the environment chamber increased to 30°C.

3. Manual tracking of the sample was required as the temperature in the chamber increased to keep the region of interest (ROI) in the focal plane of the

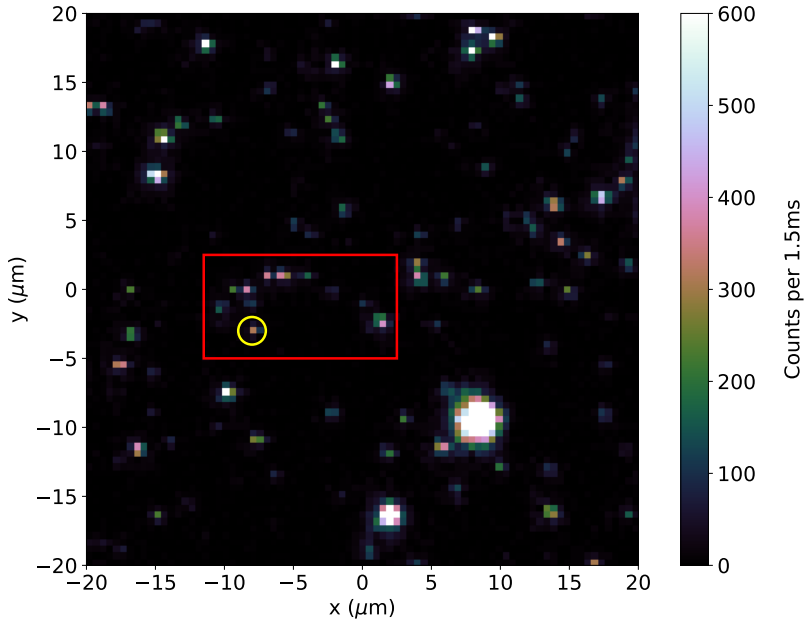

Figure 3.26: A 2D confocal image of a 90 nm nanodiamond sample. The image shows the full field of view for our microscope (40 µm × 40 µm). The red box in the image shows the selected region of interest for this sample, with the yellow circle showing the nanodiamond used for the thermometry experiments. The saturation seen in the image is caused by the chosen limits of the colour map.

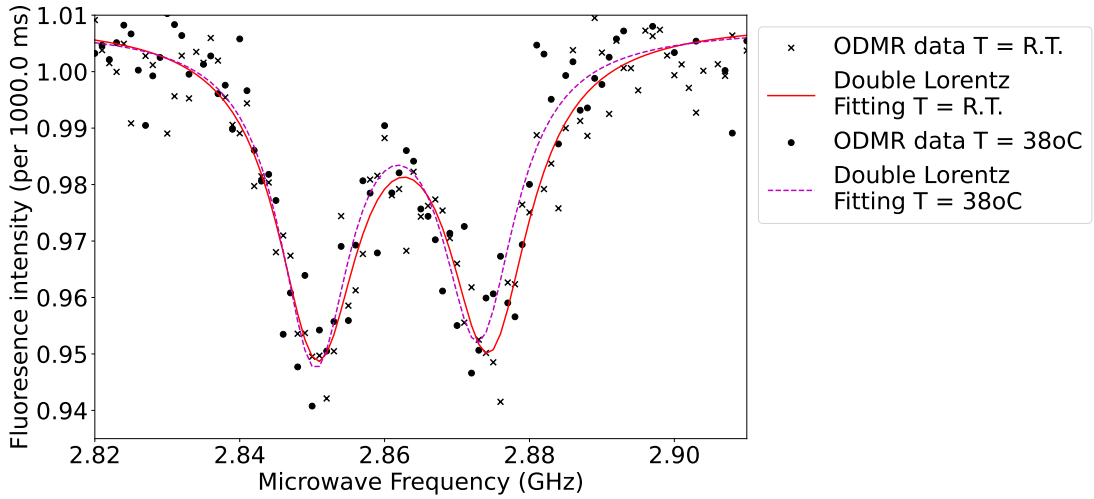

Figure 3.27: ODMR measurement from the 70 nm crystal used for the initial temperature sensing measurements using the Oko-Labs temperature stage. The figure shows the raw data for two ODMR measurements and the fittings recorded at two different temperatures, T = room temperature (R.T) or 20°C and a measurement recorded at 38°C.

microscope.

4. The environment chamber was left for 1 hour to allow the temperature to stabilise.

5. The nanodiamond of interest was then identified from the ROI, and three ODMR spectra were recorded.

6. The temperature of the environment chamber was then raised by a further 2°C.

7. Steps 3-6 were repeated with the experiment concluding once the temperature reach 38°C inside the environment chamber.

When analysing the data, I used the python scipy.optimize.curve_fit tool to fit a double-Lorentzian lineshape to each of the ODMR measurements. Using these fittings I was able to identify the resonant frequencies of the spin-state

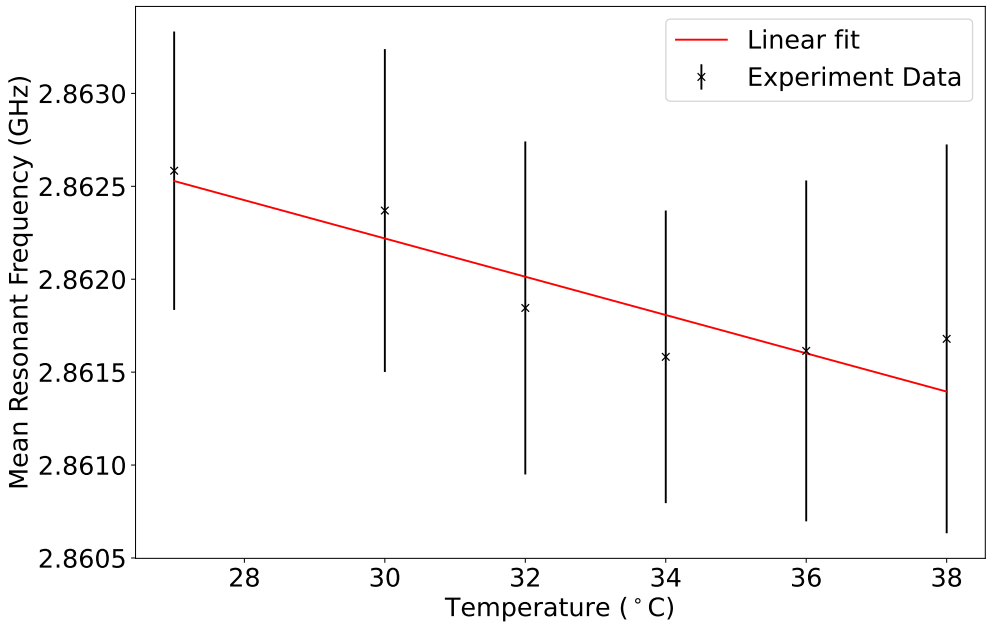

Figure 3.28: The results of the measurement of the change in the resonant frequency of the NV^- centre ensemble within the 70 nm diamond crystal as the temperature within the Oko-Labs environment chamber was increased. The error in these measurements come directly from the scipy.optimise function used to fit the double Lorentzian function to the experimental data.

transition of the NV^- ensembles for each of the measurements performed. The curve_fit function in Python also produces errors for the estimation of the two B-field split resonant frequencies from the ODMR data from the fitting of the double Lorentzian lineshape. Having found the mean microwave transition resonant frequency for each of the ODMR measurements made, I was able to plot these values as a function of the temperature within the environment chamber. The results of the temperature sensing experiments can be seen in figure 3.28 and show that the microwave resonant frequency of the NV centre decreases as the temperature within the environment chamber increases. The gradient of the linear fit used to describe the temperature dependence that we can see in the figure is -103 $\pm$ 23 kHz K^{-1}. This is of the same order as the expected value (-74 kHz K^{-1}) from the works of Acosta *et al* that first described the temperature dependence of the resonant frequency of the NV^- centre in bulk diamond [37]. While this measurement is promising, we must acknowledge that the error in the measurement of the NV^- centre resonant frequency is significant ($\approx$ 878 kHz). Using the gradient for the temperature response of the NV^- ensemble used in these experiments, the error in this measurement is equivalent to an applied temperature change of 8.5 K, which is only marginally smaller than the total temperature range over which these experiments were conducted. The main source of error in these measurements comes from the relatively low photon flux observed throughout these experiments. The photon detection error, for the photon integration time used here, is approximately $\sqrt{N}$. In these measurements, I observed a photon count rate of 350 $\pm$ 18 counts per unit dwell time, which is equivalent to a 5% error in the photon count. The 5% error in recorded photon-flux then propagate through to the error in the Lorentzian fit used to determine the NV^- resonant frequency.

Another factor that we found was affecting the stability of the fluorescent signal from the nanodiamond throughout these measurements was sample drift.

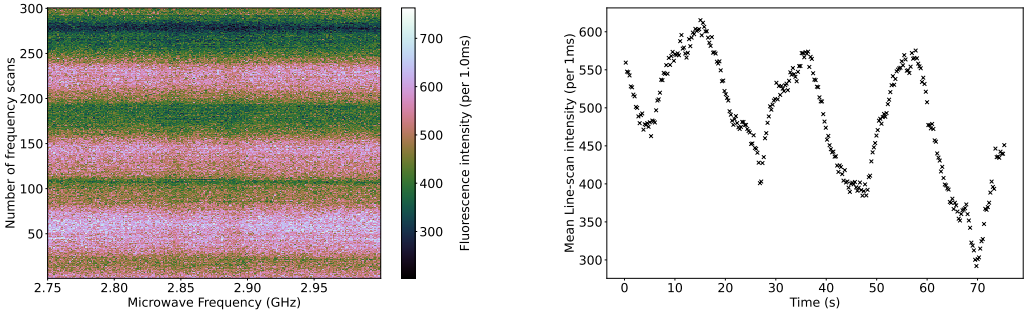

(a) (b)

Figure 3.29: The results of the ODMR measurement recorded with the Oko-Labs climate chamber activated trying to maintain the environment chamber temperature at 26°C. In both plots, the oscillation in the detected fluorescence can be seen. The effect was only seen when using the Oko-Labs stage, and is thought to be a function of the heating cycle used.

As the temperature stage attempts to maintain the temperature within the climate chamber the heaters in the sample stage and objective collar are cycled on and off. This heating cycle manifests itself as sinusoidal sample drift within the microscope, as can be seen in figure 3.29. The period of sample oscillation appears to be about 25s, and is consistent with what we would expect to see from a PID controller trying to maintain temperature within the sample chamber. I contacted Oko-Labs directly to ask them about the performance of their temperature stage. I wanted to know if it was possible for us to take control of the PID controller used to maintain temperature in the environment chamber. From this discussion it was made clear that it was not possible for us to access the PID controller or change the frequency of the heating cycles.

Conclusions from Initial Thermometry Experiments

From these initial thermometry experiments I learned a lot about our environment chamber and the performance of the Oko-Labs temperature stage:

1. The 3D printed environment chamber can be used to achieve temperatures

far in excess of the 38°C that would be required for live-mammalian cell cultures.

2. The magnetic field from the Oko-Labs temperature chamber causes Zeeman splitting in the spin-state transitions of the NV^- centre within our samples.

3. Temperature changes in the environment chamber can result in a sample drift that is significant enough for the sample to drift completely out of the field of view of the confocal microscope.

4. The Oko-Labs environment chamber and sample need approximately an hour between temperature changes in order to for the sample to be stable enough for imaging or NV^- sensing experiments.

5. Thermal cycles from the temperature stage cause cyclic sample drift that can be observed across an ODMR measurement.

6. We were able to see the effect of a temperature change on the spin-resonant frequency of the NV^- centre.

The most significant findings from these measurements from the point of view of implementing nanothermometry using the NV^- centre are numbers 5 and 6 from the above list. While I was able to observe the change in the resonant frequency of the NV^- centre with a change in temperature, the drift in the sample and the associated error in the measurement were significant enough that they needed to be addressed before the thermometry experiments could be implemented for live-cell samples. There are two ways that we could approach the problem of sample drift: We could increase the speed of the temperature sensing experiment, or, we could find a way to negate the effects of drift in the microscope. In the following section I will address our solution to compensate for the effects of drift in the sample via referenced ODMR measurements. The following

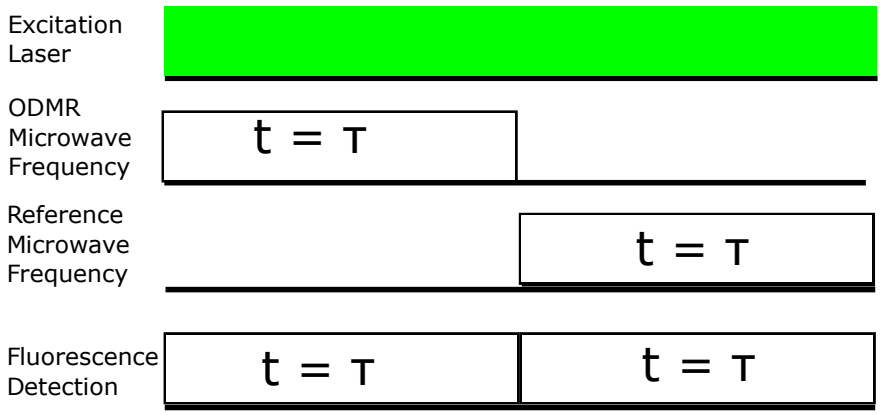

Figure 3.30: A schematic for the ODMR with referencing experimental protocol.

chapter will address the attempts to increase in scanning speed using multi-point ODMR in section 4.3.1.

3.7 Referencing with ODMR

As identified in the previous chapter, the ODMR protocol that I have been working with can be compromised by the effects of sample drift (see section 3.6.3). Addressing this problem of sample drift is not only important from the point of view of improving the quality of the data recorded during thermometry measurements, but also for ODMR measurements performed on nanodiamonds embedded within live cells [101]. In this section, I will discuss the implementation of ODMR with referencing, a measurement process that has been widely reported as a useful tool for combating the effects of sample drift in ODMR measurements [1, 4, 130].

ODMR with referencing requires that, after each measurement of the fluorescence from the NV^- centre for an applied ODMR microwave frequency, a reference measurement is made directly after. During the reference measurement, a fixed

microwave frequency (in our case, 2.75 GHz) is applied to the sample and the fluorescence intensity from the nanodiamond recorded for a fixed period of time. For our experiments, this time period was matched to that of the ODMR microwave frequency dwell time [101]. The reference measurement is then used to normalise the ODMR fluorescence measurement (I_{ODMR}/I_{Ref}). The benefit of ODMR measurements recorded with referencing is that, any sample drift is removed from the ODMR spectra during the normalisation routine, as can be seen in figure 3.31. In figure 3.31a, we can see the mean ODMR fluorescence plotted as a function of the applied microwave frequency plotted alongside the corresponding referencing measurements. This measurement was performed using a 70 nm diamond sample mounted on a tapered co-planar waveguide in the absence of any applied magnetic fields. Figure 3.31a shows the sample drift throughout this measurement was significant, with the mean ODMR fluorescence intensity dropping by 13.6% across the full microwave frequency sweep. It can be seen that the reference data (labelled as drift in the figure) tracks the sample drift very closely. Figure 3.31b shows the results of the normalisation routine applied to the dataset. The drift has been completely removed through the normalisation process, allowing for a Lorentzian line profile to be fitted to the data.

ODMR with Referencing measurements described above required a change the microwave circuit. I had to incorporate a second microwave frequency generator (Aim TTi TGR6000), used to supply a single reference microwave frequency to the sample, and an microwave switch (Mini-Circuits ZASWA-2-50DRA) into the experimental setup. Implementing the new hardware in the setup as shown in the schematic in figure 3.32, we were able to co-ordinate the switching between the two microwave signal generators with photon counting via the FPGA. This resulted in good discrimination between the ODMR data and referencing data, as can be seen in figure 3.31. The other change made to the microwave circuit was to

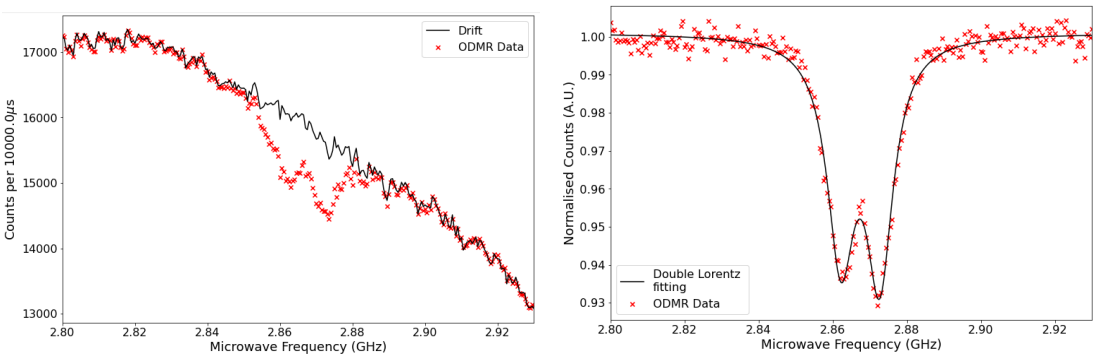

(a) Raw referenced ODMR data (b) Normalised ODMR curve

Figure 3.31: The effects of the referencing algorithm for ODMR at correcting for sample drift. In figure 3.31a the drift in the sample can clearly be seen over the duration of the measurement, the drift measurement was recorded with an off resonant microwave frequency of 2.75 GHz applied to the sample. In figure 3.31b, we see the result of normalising the ODMR intensity measurements to the fluorescence intensity recorded during the reference measurement. Through this process, the effect of the microscope drift is removed from the shape of the ODMR spectra.

replace the 35 dBm amplifier with a 40 dBm amplifier. This change allowed us to achieve the maximum 40 dBm output for both the Rohde & Schwartz and AIM TTI microwave generators used in these experiments. By matching the power output from both microwave generators, we could avoid the sample drift as a result of the heating/cooling that we see when the microwave power supplied to the coplanar waveguides changes. With the new hardware installed and tested, Dr Brian Patton was able to update the .vi script used to control the ODMR measurement to incorporate ODMR with Referencing measurements.

The benefits of this measurement protocol are clear. We are able to compensate for significant sample drift and obtain a high-quality ODMR spectra. We do face an interesting question in how we attribute error to such a measurement. From work presented previously, I have shown that the bespoke confocal microscope is close to shot-noise limited while the integration time is kept below 10 ms

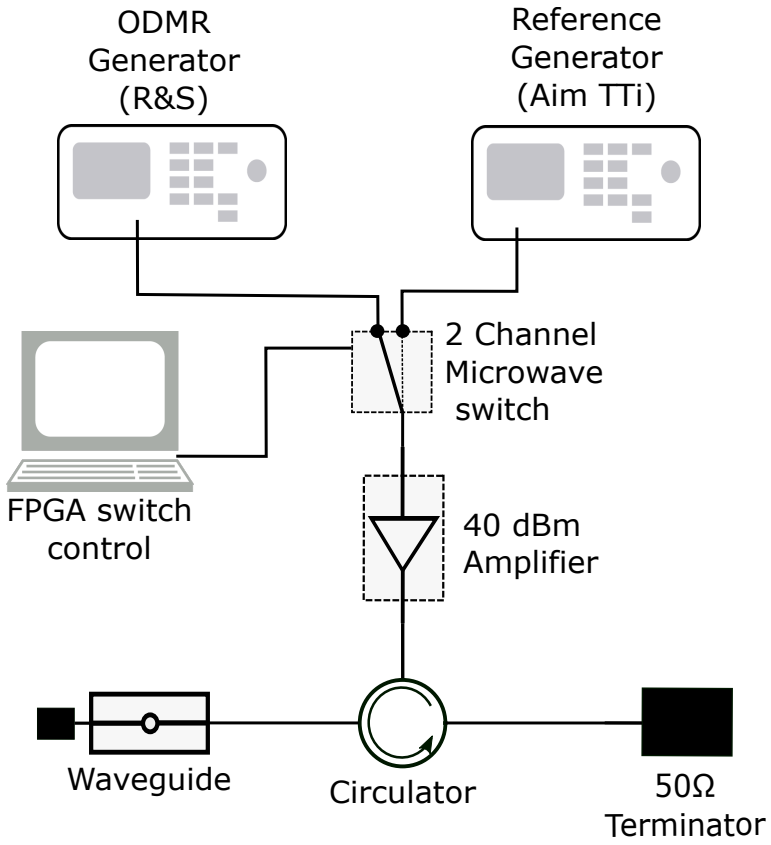

Figure 3.32: A schematic of the microwave circuit used to implement ODMR with referencing.

(section: 2.7.2). As a result we can approximate the measurement error to be:

$$\delta I(f_{MW}) = \sqrt{I(f_{MW})} \tag{3.11}$$

At the time of writing, the ODMR with Referencing measurements are recorded with n measurements of the fluorescence intensity from the nanodiamond sample for an applied microwave frequency performed before the next microwave frequency applied. As a result, it is conceivable that, if the fluorescence detection rate was low enough, and there was significant sample drift across the measurement, the percentage error may vary significantly between the beginning and end of the ODMR measurement. The error in the ODMR with Referencing measurement for each applied microwave frequency is calculated as:

$$\delta I(f_{\mu wave,i}) = \sqrt{\sum \frac{I(f_{\mu wave,i}) - \bar{I}(f_{\mu wave})}{N-1}} \tag{3.12}$$

In which: $I(f_{\mu wave,i})$ is the normalised intensity recorded for a microwave frequency ($f_{\mu wave,i}$), $\bar{I}(f_{\mu wave})$ is the mean recorded fluorescence intensity recorded for a specified microwave frequency, and N is the number of measurement point repeats per frequency line scan. This can also be described as the standard deviation for the normalised intensity recorded for each of the applied microwave frequencies.

3.8 Summary

In this section I have discussed the development of the protocol for performing continuous wave optically detected magnetic resonance (CW ODMR) spectroscopy. I have investigated the use of two different methods of microwave delivery for the ODMR measurements: the double split ring resonator [87] and the coplanar waveguides [104]. In our confocal microscope system, we believe

the microwave field generated by the DSRR was being grounded by the microscope objective and therefore the coplanar waveguide proved to be more suitable for our measurement schemes due to the projected field only extending a few 100 µm from the micro-wire antenna. Having then characterised the performance of the coplanar waveguides for microwave delivery, I have investigated the factors that need to be considered to optimise the ODMR contrast from a nanodiamond probe. I have looked at the relationship between:

- The applied microwave power and the percentage of the ODMR contrast, finding that while increased power does increase ODMR contrast, this come at the cost of increase microwave power broadening. Therefore the microwave power applied to a sample needs to be carefully considered to achieve the maximum sensitivity from a nanodiamond probe.

- The laser power and the ODMR contrast, the results of which showed that as laser power is increased, the ODMR contrast decreases. This is thought to be the result of optically-induced energy level transitions occurring so frequently that spin-state transitions are not able to be excited by the applied microwave signal [123].

- While investigating the factors that affect DC magnetometry measurements, the maximum sensitivity of observed from these measurements was $1.13 \pm 0.04\,\mu\mathrm{T}/\sqrt{\mathrm{Hz}}$.

I also investigated the application of the CW ODMR protocol for temperature sensing using the Oko-Labs temperature stage. The results of the experiment showed that it was possible to measure the effect of increased temperature on the resonant frequency of the NV^- ensemble used for the measurement. The error associated with these measurements was significant (as large as the full applied temperature range). One source of this error is thought to be the result of the sample drift that is induced when the Oko-labs H301-T environment chamber

is in operation. Another source of error in this measurement is the associated error in monitoring the fluorescence counts from the nanodiamond probe. In these measurements, the fluorescence intensity from the diamond was very low due to the low laser power applied. As a result, the error associated with photon counts ($\Delta I = \sqrt{I}$) in the measurement was about 5% of the overall signal. This secondary error source can be easily rectified by applying additional laser power, assuming the ODMR contrast is not compromised.

The drift introduced by the Oko-Labs stage did encourage us to develop an ODMR with referencing measurement scheme. This measurement scheme has resulted in a method of drift correction that allows ODMR measurements to be performed and the resonant frequency of the NV^- centre to be accurately determined even in the face of sample drift.

Overall, I have demonstrated that I have been able to implement a CW ODMR measurement protocol that allows us to measure both magnetic fields and temperature fields using nanodiamond probes as a sensor. I have also investigated the factors that can effect the sensitivity of the NV^- ensemble and commented on how one might choose to consider these parameters to ensure the greatest sensitivity when measuring either temperature or magnetic field.

Chapter 4

Towards ODMR for Biosensing

4.1 Introduction

There are many challenges that are faced when trying to perform live cell imaging. The structures of the cells are often complex systems with a variable refractive index throughout, which induce aberrations during imaging [72, 131]. The induced aberration from the sample impairs the signal to noise ratio and degrades image quality [132]. For our experiments, any loss of signal as a result of these aberrations would result in longer measurement times in order to achieve comparable measurement sensitivity to an unaberrated system [133]. In this section I describe experiments performed to see how the controlled introduction of aberrations using our deformable mirror affects the performance of ODMR measurements. These experiments were preformed to evaluate the usefulness of adaptive-optics in biosensing using a nanodiamond probe.

Another challenge with respect to performing temperature or magnetic field sensing on live cells samples is the speed at which the measurements are recorded [35]. The speed of the ODMR measurement needs to be carefully balanced so that the dynamics of the cell's response to an applied stimuli can be monitored,

while allowing a long enough detection time to accurately measure any changes in temperature or magnetic field [134]. Sample drift and live-cell movement also place time constraints on how long an accurate ODMR measurement can be performed [135]. The major time constraint in NV^- sensing is the time it takes to complete a high-resolution microwave frequency scan to record an ODMR measurement. From the measurements that we have performed in our system, a continuous ODMR spectra can require hundreds of frequency steps to obtain sufficient resolution to accurately determine the resonant frequency of the NV^- centre. In addition, it is often advantageous to perform multiple ODMR frequency line scans to improve the signal-to-noise of a measurement, by averaging the microwave frequency dependent fluorescence intensity [101]. I will introduce in this chapter a multi-point measurement scheme for NV^- thermometry as outlined in [1]. I will also evaluate three different multi-point ODMR temperature sensing algorithms that have been reported in literature [35, 4, 1].

4.2 ODMR and Adaptive Optics

As shown previously in this work (section 2.3), adaptive optics can be used to compensate for sample induced aberration to improve image quality and signal to noise in biological imaging [2, 49]. In this section, I outline an investigation to see how aberrations can affect the performance of our ODMR measurement protocols. With the deformable mirror, we are able to add aberrations into our system in a controlled way [136, 137]. Starting with an imaging system free from aberration, I recorded a measurement of the microscope's PSF and an ODMR spectrum from a single nanodiamond as a control dataset. I then added a fixed amount (0.3 mode units), of one of the Zernike modes (oblique astigmatism or vertical coma) and repeat the PSF and ODMR measurements using the same nanodiamond crystal.

Table 4.1: The changes in the characteristics of the recorded ODMR curves as the applied oblique astigmatism was increased. Here we look specifically at the recorded ODMR contrast, the R^2 value for the fitting, the mean fluorescent signal for the full ODMR curve and the standard deviation of the mean off-resonant fluorescence intensity from the diamond under study.

Applied Astigmatism units	ODMR Contrast (%)	R^2	Mean Fluorescent Signal (10 ms^{-1})	Standard Deviation of Off Resonant signal (10 ms^{-1})
0	7.4	0.91	2010	82
0.3	7.4	0.91	1891	79
0.6	7.0	0.93	1783	76
0.9	6.8	0.88	1638	75
1.2	7.0	0.90	1363	67
1.5	6.8	0.87	1072	59

The first of these experiments was performed using a 40 nm diamond sample. In figure 4.1 we can see a comparison between the PSF and ODMR spectra recorded at the beginning of the experiment with no aberration applied, and the effects on both after +1.5 units of astigmatism had been applied to the imaging system via the DM.

To analyse the dataset comprising all the different applied aberrations,, I have evaluated how the increase in applied aberration affected: The mean fluorescence intensity measured from the ND, the R^2 value for the double Lorentzian curve fitting to the ODMR data, the standard deviation of the off-resonant fluorescent signal (shot-noise) and ODMR dip contrast. Table 4.1 shows how these four characteristics of the ODMR measurement changed throughout this experiment. The analysis revealed that the ODMR contrast remained relatively constant as a result of the applied aberration is increased. This seemed a surprising result, however, the ODMR contrast is a percentage drop in the fluorescence intensity from the NV^- ensemble [36]. Therefore, regardless of the optical aberration that

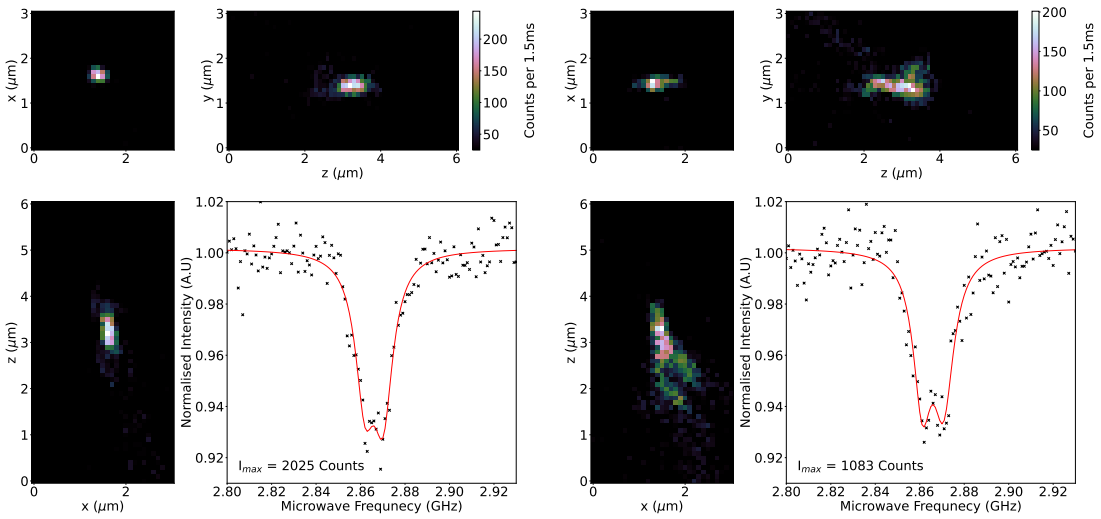

(a) (b)

Figure 4.1: An image of a clean (4.1a) and aberrated (4.1b) PSF from the microscope and the ODMR measurement recorded from the same nanodiamond using the same imaging parameters.

is applied to the system, if the ODMR contrast is larger than the measurement noise, one should recover the same ODMR contrast with or without optical aberrations applied. The R^2 value for the Lorentz fitting to the ODMR data show signs of decreasing as the applied aberration was increased. This is likely the result of the drop in the fluorescence intensity as the aberration is increased. The signal to noise of the ODMR curve increases as the fluorescence intensity decreases, resulting in the R^2 value for the fitting decreasing [85].

The second experiment of this type was performed using a 70nm ND. The same experimental process was repeated using this sample, however, vertical coma was applied rather than oblique astigmatism. The results of this experiment can be seen in table 4.2 and show an interesting trend, in that, the ODMR contrast increases as the aberration increases. This is an unexpected result given the stability of the ODMR contrast observed for the 40 nm diamond sample. One possible explanation could be that we are not seeing as much laser power reach

the sample as the aberration magnitude in increased. This is supported by the drop in the fluorescent signal recorded as the aberration magnitude increased. If this is the case, then what we may be seeing is the same effect observed in section 3.5.3, in which increased laser power supplied to the sample was found to decrease the recorded ODMR contrast [123].

Where we do see significant agreement between the two experiments is that mean fluorescence intensity from the ODMR measurement drops significantly with increased aberration applied, and the mean standard deviation increases as a percentage of the mean fluorescent signal. I also included a final measurement at the end of the experiment that removed the applied aberration and returned to a unperturbed system. The results of this final measurement are in good agreement with the first measurements in the dataset. This supports the argument that the loss in the fluorescent signal is a direct result of the aberration applied to the imaging microscope system and not the result of fluorophore bleaching or sample degredation. Herein lies the importance of a deformable mirror when performing bio-sensing experiments. With the ability to correct for the aberrations introduced to the system by biological material, the DM allows us to achieve a fluorescence intensity from the nanodiamond during ODMR measurements that would not otherwise be possible for a given applied laser power. This is a benefit as it limits the photo-damage that is caused to the sample (be it fixed or live) [25] and reduces the integration time for photon collection during ODMR spectroscopy. This in turn reduces the total measurement time in comparison to a system not capable of aberration correction. By decreasing the total measurement time, we improve the ability of our system to track temperature changes occurring within live-cells in real time, as they are exposed to different external stimuli.

Table 4.2: The table here shows the response of the ODMR from a 70nm nanodiamond as the vertical coma applied to the system via the deformable mirror.

Applied Astigmatism units	Mean ODMR Contrast (%)	R^2	Mean Fluorescent Signal (10 ms^{-1})	Standard Deviation of Off Resonant signal (10 ms^{-1})
0	5.2	0.96	7157	169
0.3	5.9	0.96	6330	153
0.6	6.1	0.96	5130	137
0.9	6.1	0.97	4703	126
1.2	6.3	0.96	4022	115
0	5.5	0.97	7463	163

4.3 Four-Point ODMR

4.3.1 Introduction

One of the drawbacks to performing NV^- thermometry or magnetometry using a CW ODMR measurement is the length of time it takes to complete a high resolution frequency sweep [1]. An ODMR sweep in which there are: 100 applied microwave frequency points, a 10 ms photon integration time per applied frequency and 150 frequency line scan repeats, results in a total experiment time of 150s. This puts a minimum stability requirement on the microscope that the diamond under investigation must remain within the focal spot of the excitation laser for the length of the experiment. It also limits thermometry to measurements of temperature dynamics that happen on a longer time scale than the length of time of a full ODMR sweep [1]. One method that has been suggested to overcome the time constraints of a CW ODMR measurement is to perform ODMR using just a few frequency points, selected from the point of maximum gradient from a high resolution ODMR spectra [101]. An example of the selection of four microwave frequency points for multi-point ODMR can be seen in figure 4.2b. By monitoring the change in the fluorescence intensity from the NV^- centre from these four applied frequencies one can determine the resonance frequency

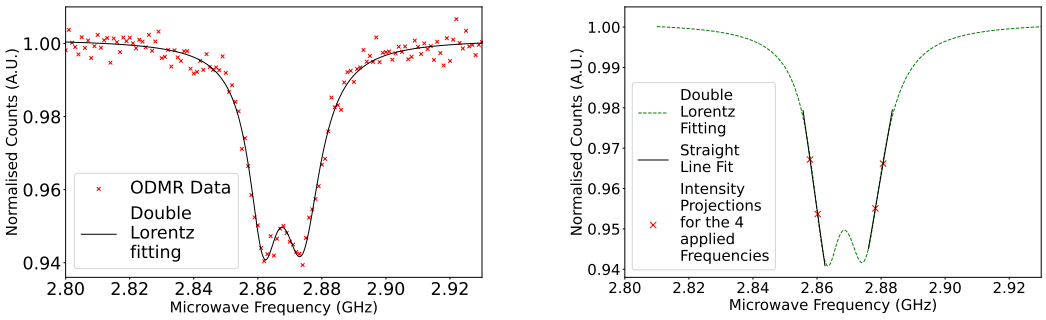

(a) ODMR with referencing

(b) Normalised ODMR curve

Figure 4.2: Here we can see in the normalised CW ODMR spectra from a 70nm diamond that is to be used for the investigation of the four-point ODMR measurement 4.2a. For this measurement, the off-resonant signal was 10,000 counts per 10ms. In 4.2b, we can see the linear fitting to the slopes of the ODMR dip and the four frequency points extracted from the ODMR curve. These four points are denoted by the crosses on the graph.

of the defect [35]. Therefore, the four point ODMR measurement can be used to monitor the changes in temperature of the environment surrounding the NV^- centre as they occur [37]. Multi-point ODMR has already been used in previous studies to monitor temperature changes both within single cell organisms [35] and within living *C.elegans* [1].

In the following sections I will discuss the implementation of these multi-point protocols within our experimental set-up. I have investigated how the integration time and the number of point repeats used in these experiments affects the reliability of the measurement. The aim of this study was then to determine the optimal parameters for performing four-point ODMR. These experiments were conducted using the ODMR with Referencing measurement protocol discussed in the previous chapter (section 3.7).

4.3.2 Dwell Time

To begin these experiments, I investigated the effects of increasing dwell time on the precision of the four point ODMR process. For these measurements, I used a 70 nm diamond mounted on a coplanar waveguide for microwave delivery. The microwave power at the output of the microwave amplifiers was constant at 35 dBm throughout these measurements. The laser power was also kept constant to maintain a constant fluorescence photon-flux of 800 kCounts s^{-1} from the nanodiamond under study. I will now outline some of the language used in this section for the clarity of the reader:

- Dwell time - This will be used interchangeably with integration time, and defines the period of time used for photon counting. This also defines the length of time that each of the applied microwave frequencies is applied to the sample.

- Point repeats - Defines the number of times that photon counting over a fixed dwell time is performed for an applied microwave frequency. eg: 100 point repeats were made for an applied frequency of 2.87 GHz.

- Measurement - A single ODMR (CW or multi-point) measurements, comprising of n point repeats for each of m applied microwave frequencies. We are particularly interested in the case where m=4, i.e. the four point measurement schemes as explored in this section.

For each of the measurements, 100 point repeats were used for each of the applied microwave frequencies. The full ODMR spectra from the nanodiamond under study and the four selected microwave frequencies can be seen in figure 4.2. The dwell time used for photon collection was varied from 1 ms to 100 ms. For each of the dwell times used, the 4-point ODMR measurement was repeated seven times. The precision of the measurement was calculated using the standard

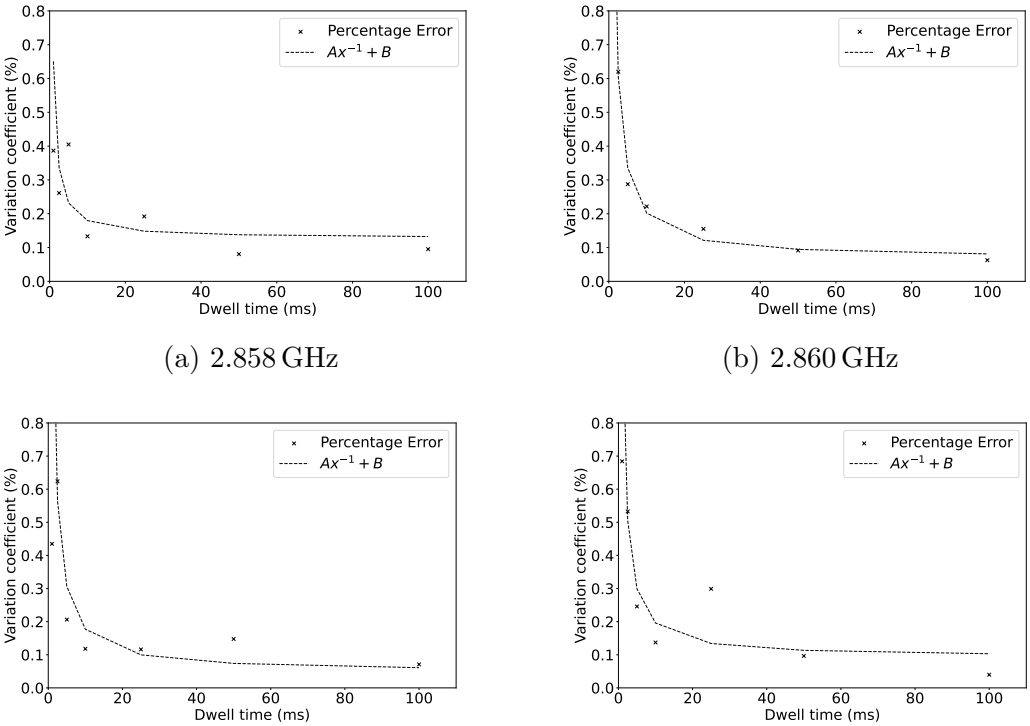

(a) 2.858 GHz (b) 2.860 GHz

(c) 2.878 GHz (d) 2.880 GHz

Figure 4.3: Presented here are the plots for the percentage errors plotted for the normalised intensity measured for the dwell times used for the four applied microwave frequencies.

deviation of the mean-normalised fluorescence intensity from across the seven measurements.

To assess the accuracy of a measurement, the root mean square difference between, the mean-normalised fluorescence intensity for each of the four applied microwave frequencies, and that of the fluorescence intensity for each of the four applied microwave frequencies from the complete CW-ODMR spectra.

$$\delta I(f_i) = \sqrt{(\bar{I}(f_i)_{4,\ points} - I(f_i)_{full\ ODMR})^2}. \tag{4.1}$$

4.3.3 Measurement Precision

The analysis of the precision measurements can be seen in figure 4.3. The graphs show the coefficient of variation of the normalised intensity for each of the four applied microwave frequencies. The coefficient of variance (CV) was calculated using the following equation:

$$CV = 100 \times \frac{\sigma}{\bar{I}(f_i)}. \tag{4.2}$$

In which $\bar{I}(f_i)$ is the mean of the normalised fluorescence intensity recorded from the nanodiamond under study for one of the i applied microwave frequencies. σ_i is the standard deviation of the fluorescence intensity point repeats $I(f_i)$. This gives us the coefficient of variance as a percentage of the mean-normalised fluorescence intensity observed for each of the measurement dwell times used in this experiment. The results show that as the dwell time for photon counting per point repeat is increased, the precision of the measurement also increased (coefficient of variance decreased). This relationship can be modelled using the following equation:

$$CV = \frac{A}{t_{dwell}} + C. \tag{4.3}$$

In which A and C are both constants and t_{dwell} is the dwell time for photon collection. The coefficients of fitting for the data presented in figure 4.3 and the R^2 values describing the goodness of fit are presented in table 4.3. In each case the coefficient of variance is tending towards approximately 0.1% as the dwell time increases to 100 ms. This result is consistent with the number of photons detected increasing linearly with the increase in the integration time for photon detection (see figure 4.4a), thus reducing the percentage error in photon-counting [85].

The aim of this experiment was to determine the parameters that would allow

us to perform the four-point ODMR algorithm both quickly and with high precision. From the results in figure 4.4b, a dwell time of 25 ms, or a mean photon count per frequency point measurement of 25,000 counts per unit dwell time is sufficient to produce a repeatable result in our system. With these measurement parameters the projected variance coefficient is 0.16%, and results in a total measurement time of 20 s. To improve the precision of the measurement to below 0.1%, for example, would require a 3 times the total photon count. This could be achieved by either:

- **Increased dwell time:** An increase in the dwell time would result in more photons being collected per point repeat, resulting in an increase in precision. However, this would result in an increase in the total time required for measurement, which increases the chance that sample drift/movement may affect the measurements performed.

- **Increased laser power:** By increasing the laser power, one can increase the fluorescent signal from the nanodiamond. As shown previously (section 3.5.3) an increase in laser power can result in a loss of ODMR contrast from an NV^- ensemble within a nanodiamond. With this in mind, one needs to be careful not to accidentally decrease the sensitivity of an ODMR probe while trying to maximise the precision of the measurement.

One therefore needs to carefully consider the measurement parameters used for the four-point ODMR measurement in order to balance measurement precision and probe sensitivity.

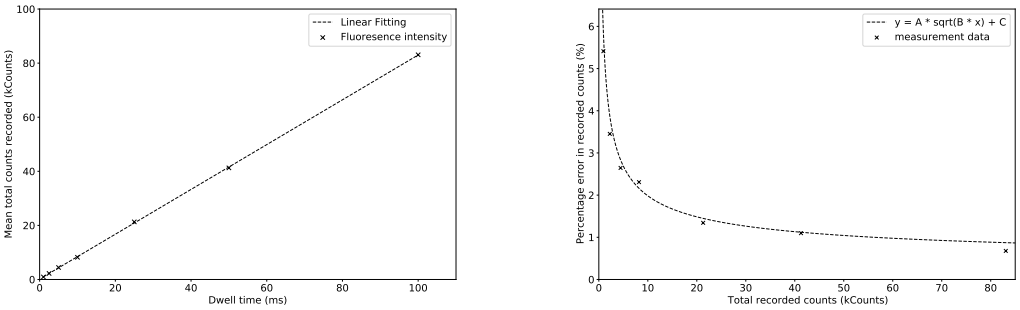

(a) (b)

Figure 4.4: In figure 4.4a we see the linear increase of measured fluorescence intensity with increased dwell time for an applied microwave frequency of 2.858 GHz. The gradient of this line is the fluorescent output from the nanodiamond that we are able to detect with our system. Figure 4.4b shows the decrease in the percentage error as the total mean counts recorded during the four point measurement increase. The percentage error reduces proportionally to the square root of the mean total counts recorded.

Table 4.3: A table showing the fitting parameters for the percentage error of the normalised four point ODMR measurements plotted as a function of the applied dwell time in figure 4.3

Applied Frequency (GHz)	A	C	R^2
2.858	0.357	0.088	0.631
2.860	1.169	-0.108	0.970
2.878	0.507	0.040	0.627
2.880	0.689	0.012	0.865

.

4.3.4 Accuracy

The accuracy of the four-point ODMR measurements was calculated using the following equation:

$$Accuracy = 100 - 100 \times \left(\frac{|\bar{I}_{norm}(f_i) - I_{Lorentzfit}(f_i)|}{I_{Lorentzfit}(f_i)} \right). \tag{4.4}$$

In which, $I_{Lorentzfit}$ is the projected normalised fluorescence intensity from the double-Lorentzian fit, and $\bar{I}_{norm}(f_i)$ is the mean normalised fluorescence intensity from the seven measurements performed for each of the applied dwell times.

The analysis of the measurement accuracy for the dwell times used for photon counting can be seen in figure 4.5a.

The results in figure 4.5 show that in each case, the accuracy of the measurement never dips below 99%. This suggests that for a fluorescence detection rate of 850 kCounts s^{-1} and 100 point repeats per applied microwave frequency is enough to get within 1% of the normalised fluorescence intensity projected by the Lorentzian fit to a full ODMR spectra. Even in the case at which the dwell time for measurement was 1 ms, the accuracy of measurement was still within the expected variation of the fluorescence intensity from the shot-noise limit approximation made [85].

4.3.5 Frequency Point Repeats

Another factor that needs to be considered when optimising the length of the four-point ODMR protocol is the number of point repeats that are used per applied frequency. Performing multiple point repeats allows us to calculate the mean fluorescence intensity for each of the applied microwave frequencies, and reduce the overall measurement error by $\sqrt{n}$, where n is the number of point repeats. In the following section, I investigate how the number of point repeats affects the precision and accuracy of the ODMR measurement. The number of point

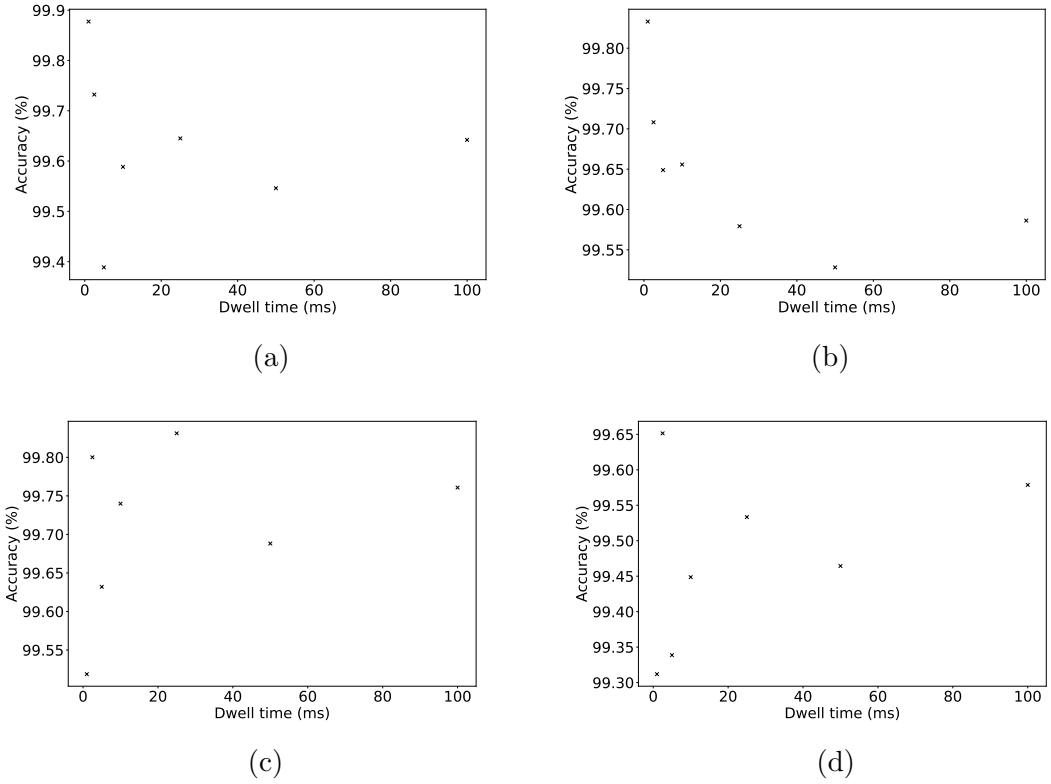

Figure 4.5: The accuracy plots for the fluorescence intensity measurements recorded for the four applied microwave frequencies 2.858 GHz 4.3a, 2.860 GHz 4.3b, 2.878 GHz 4.3c, and 2.880 GHz 4.3d, plotted against the dwell time for a single frequency point measurement. In all cases the accuracy of the measurement is above 99%.

repeats is varied from 10-1000, while the measurement dwell time per applied frequency point remained constant at 10 ms and the detection rate for the NV^- centre fluorescence is 1.15 MCounts s^{-1}, i.e. increasing points directly increases the number of photons detected for a given applied microwave frequency. A 70 nm diamond sample was used for this measurement and the microwave power was fixed throughout this experiment at 40 dBm at the output of the microwave amplifier. In these experiments the ODMR with referencing protocol was used. The four frequency points were chosen using using the method outlined in figure 4.2b, and will be discussed in more depth later in this chapter (section 4.5). 7 measurement repeats were made for each increase in the number of point repeats used throughout this experiment. As was the case for the dwell time analysis, the precision and accuracy of the measurements were calculated from these results.

Precision

The precision of the measurements was quantified using the coefficient of variance between the seven datasets recorded for each measurement regime. The results of these experiments can be seen in figure 4.6, and show the coefficient of variance decreases proportionally with $\frac{1}{n}$, with n being the number of frequency point repeats. From these results it can be seen that for 200 line repeats the precision is starting to approach the asymptotic minima, between 0.1% and 0.2%. For the diamond used in this measurement, 200 frequency point repeats and a fluorescent photon flux of 11,000 counts per unit dwell time produced a sufficiently precise measurement for multi-point ODMR measurements.

Accuracy

I assessed the accuracy of the measurement repeats experiments using equation 4.4. The results of these experiments can be seen in figure 4.7. Here we see no real

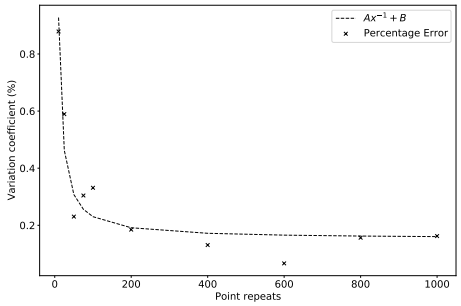

(a) f = 2.8592 GHz

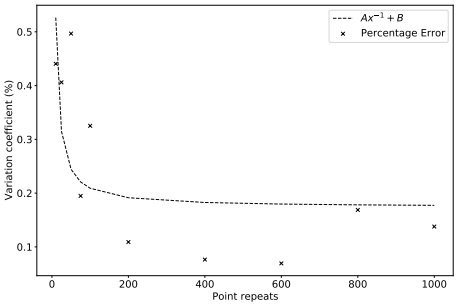

(b) f = 2.8612 GHz

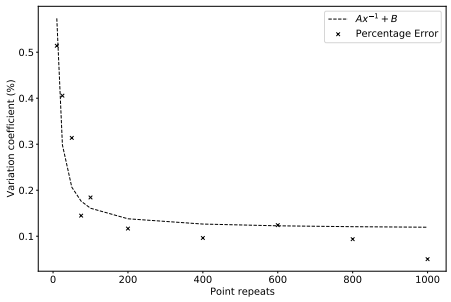

(c) f = 2.8763 GHz

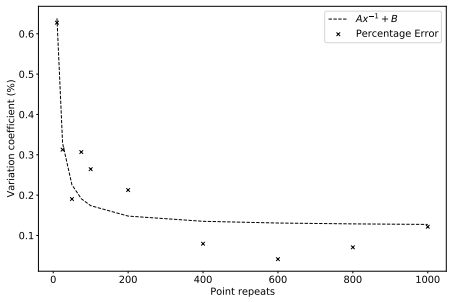

(d) f = 2.8783 GHz

Figure 4.6: Here we see the results of the precision measurements for each of the microwave frequencies used within a four-point ODMR scan with referencing as the number of repeats used in an experiment is increased. We can see that in each case the co-efficient of variance decreases towards an asymptotic value around 0.1% following a $\frac{1}{n}$ relation.

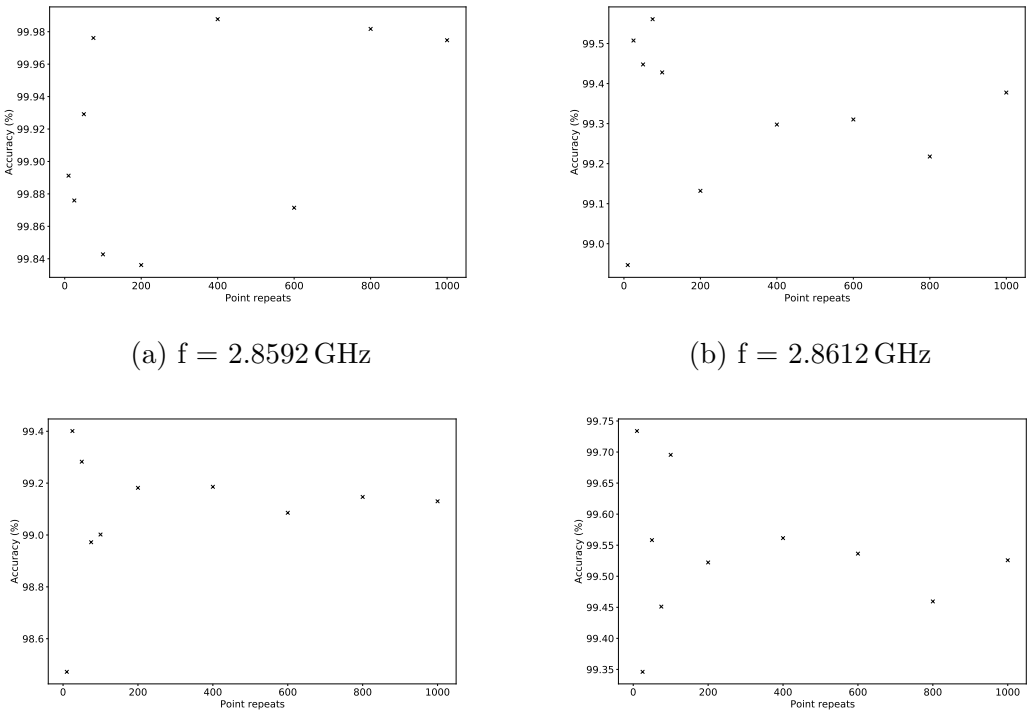

(a) f = 2.8592 GHz

(b) f = 2.8612 GHz

(c) f = 2.8763 GHz

(d) f = 2.8783 GHz

Figure 4.7: The accuracy for the four-point ODMR measurement with referencing when the number of repeats is varied. We can see that for each of the four microwave frequencies applied, the measurement accuracy is universally above 99%, regardless of the number of point repeats used.

dependence of the accuracy on the number of repeats performed as all measurements have an accuracy above 99%. The variation that we see in the accuracy of measurement is likely to be the result of the shot noise in the measurement.

4.4 Simulated Temperature Sensing

In 2010, Acosta *et al* published their paper describing the linear dependence of the resonant microwave frequency of the NV^- centre to temperature in conditions around room temperature [37]. By controlling the environment temperature around a single-crystal diamond containing an ensemble of NV^- defects,

the group were able to monitor changes in the resonant frequency as the temperature was varied between 280 K and 330 K. They discovered that, across this temperature range, the resonant frequency (D) of the NV^- changed as $\frac{dD}{dT} = -74\text{kHz}\,\text{K}^{-1}$. This linear relationship has been confirmed via experiment for NV^- centres within nanodiamond structures as well [35, 102]. To date there is not a theoretical model that is able to accurately describe the results seen in experiment, it is suspected that this temperature dependence is related to lattice expansion coupled to temperature dependence of the phonon-electron interactions [94, 138]. While some variation in the temperature dependency of the NV^- centre resonant frequency has been observed [1], the value of -74 kHz K^{-1} is often quoted in literature [35]. Kucsko *et al* in their work showed that it is possible to accurately determine changes in temperature within a live cell environment via a nanodiamond probe using a multi-point ODMR [35]. This work has since been built upon by Fujiwara *et al* [1] and Singam *et al* [4] showing a small subset of frequencies can be used for ODMR measurements to accurately monitor temperature changes using the NV^- centre for thermometry.

One of the aims of this research project has been to investigate methods that could be used to monitor temperature changes within live-cells using our confocal microscope and nanodiamonds as an all optical probe. We initially looked to investigate the temperature response of our nanodiamond sensors using an Oko-Labs (H301-T) temperature stage. The results of this investigation are outlined in detail in section 3.6. To summarise the results briefly, the magnetic field from the sample holder alongside the sample drift that occurs when the temperature stage is in operation meant that accurate temperature sensing experiments were almost impossible to perform. An example of an ODMR with referencing measurement performed using the temperature stage can be seen in figure 4.8. As a quantification of the quality of the fit, the R^2 value for this fitting was 0.53.

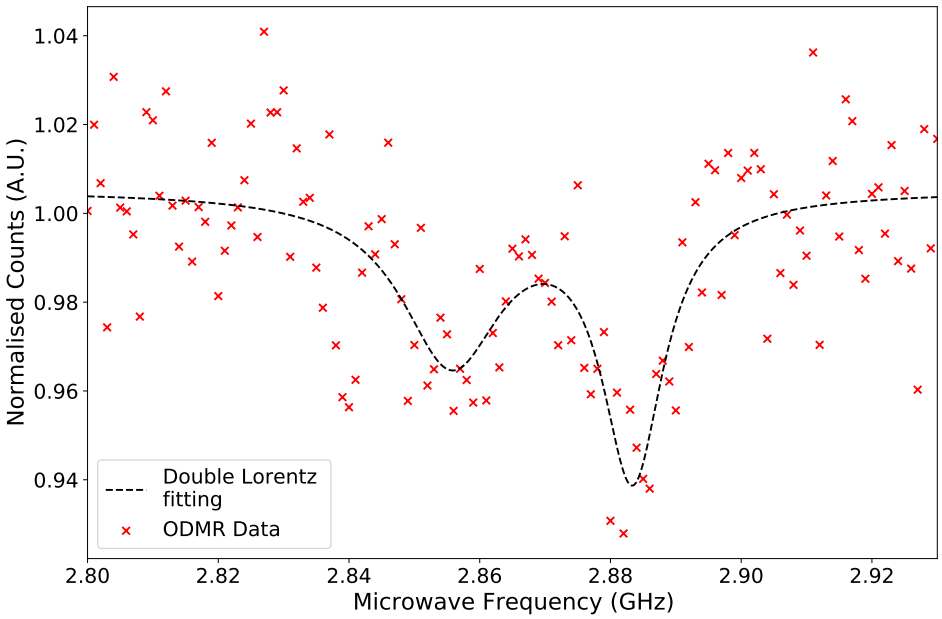

Figure 4.8: The ODMR spectra from a 70 nm diamond crystal while the Oko-Labs temperature stage was mounted in our imaging system. The data shown here shows that the magnetic field from the temperature stage has degraded the quality of the ODMR curve so that NV^- thermometry would not be possible while the temperature stage is in place. The R^2 value for this fitting was 0.53.

This fitting was made with a mean fluorescence intensity of approximately 500 counts per 10 ms. This photon count was very low and no doubt contributes to the quality of the fitting able to be achieved. The reason for choosing such a low laser power, and therefore fluorescence intensity for this measurement was the relatively low ODMR contrast. Any increase in laser power would have resulted in a loss of contrast, which in turn would have affected suitability of the nanodiamond under study for thermometry or magnetometry.

During the investigation of multi-point ODMR methods for temperature sensing, I recognised that it is possible to simulate the effects of temperature. A temperature change of δT is observed in NV^- thermometry as a translation of the

full CW ODMR spectra in frequency by an amount equivalent to $\frac{dD}{dT} \times \delta$ T [37]. We are able to simulate the effects of a temperature change by applying a fixed frequency shift (simulated temperature change) to all of the microwave frequencies applied, effectively shifting the ODMR spectra in frequency as a change in temperature would. In the analysis of these experiments, the results are treated as if this frequency shift was never applied. The aim of analysis is then to try to recover the magnitude of the simulated temperature change (The applied frequency shift) by comparing the results of the measurement to a data set in which $\Delta T_{sim} = 0\,K$. In the following, I will describe the use of simulated temperature change experiments to evaluate the performance of three reported techniques for temperature sensing using multi-point ODMR [35, 1, 4]. All three of these temperature sensing techniques were applied to the same experimental dataset (described in the next section) to allow for direct comparison between the three methods.

4.5 Description of Four-Point ODMR Evaluation Data Set

To compare the performance of the three temperature sensing techniques outlined in [1, 4, 35] with our microscope, I performed a simulated temperature sensing experiment. Using a 70 nm diamond probe, I extracted the four frequency points from a full CW ODMR spectra using the process outlined in [1], and described briefly here:

1. A full CW ODMR spectra was recorded from the nanodiamond in question.
2. A double-Lorentzian lineshape was then fitted to the data.
3. A straight line fit was made to the point of maximum absolute gradient of

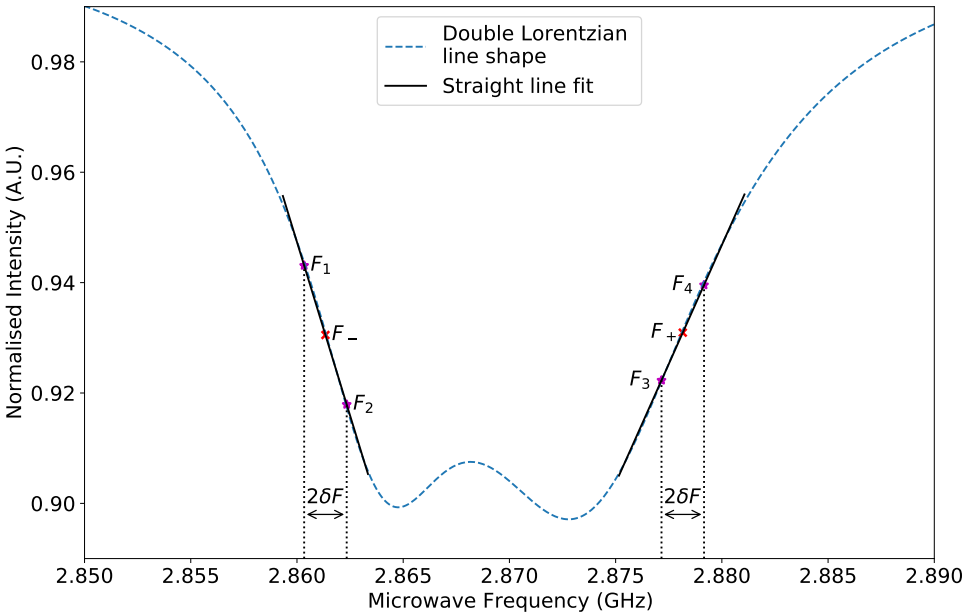

Figure 4.9: A figure showing the four frequencies (f_1 - f_4) selected for performing ODMR as described by the authors of [1].

the Lorentz fitting, extending to the point at which the root mean square error between the straight line fit and the Lorentz fit was larger than 0.2%.

4. The frequency corresponding to the mid-point of the straight line fits was found, denoted as F_- and F_+ in figure 4.9.

5. The four microwave frequencies (f_i) to be used in the experiment following the equation:

$$f_i = f_\pm \pm \delta f \tag{4.5}$$

In which $i = 1, 2, 3, 4$ and δf is a fixed frequency shift (eg: 1MHz). A visual representation of this process can be seen in figure 4.9.

The dataset used for the simulated temperature sensing experiments contained: 56 four-point ODMR data measurements all recorded from the same

nanodiamond. The parameters of the scan were:

- A photon integration time per applied frequency point of 10 ms.
- 250 intensity point repeats per applied microwave frequency.
- The applied microwave power after the amplifier of 38 dBm for both the four-point ODMR microwave generator and the reference microwave frequency generator.
- The reference frequency used in these experiments was fixed at 2.75GHz.

These measurement parameters were kept constant throughout the experiment. The process of the simulated temperature sensing, as described above, involved adding a known frequency shift to the four microwave frequencies used in the four-point ODMR measurement to simulate the effects of a temperature change. For this experiment, a frequency shift of 150 kHz was applied to the sample, assuming Acosta's value for $\frac{dD}{dT} = -74\text{kHz}\,\text{K}^{-1}$, this frequency shift were equivalent to a 2°C temperature change [37]. For each simulated temperature change applied to the sample, seven multi-point ODMR measurements were recorded. This allowed me to quantify the precision of the measured simulated temperature shift and monitor the repeatability of the measurement. Each of the seven measurement repeats are considered to be independent of one another as the excitation laser needed to be optimised to maximise the fluorescent output from the nanodiamond. Once all seven measurements had been recorded, the four applied microwave frequencies were increased by another 150 kHz, and the four-point ODMR measurements recorded. This process was repeated until the total frequency shift applied was 1050 kHz (14°C).

In the following sections, I will outline the analysis techniques presented by Kucsko *et al* [35], Singam *et al* [4] and Fujiwara *et al* [1]. I have evaluated the

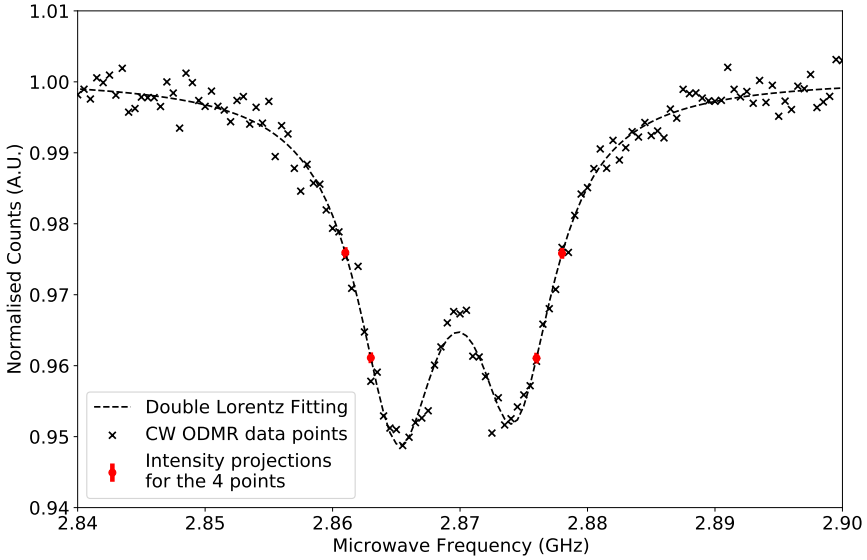

Figure 4.10: The double Lorentzian fitting for the CW ODMR curve from a 70nm diamond used for the selection of the four-points used to generate the initial four-point ODMR measurements in the dataset described. The dataset was recorded with a microwave frequency step size of 0.5MHz, a pixel dwell time of 10ms and 100 point repeats.

above dataset using each of these techniques, and have reported on the effectiveness of each analysis method for temperature sensing in our system. To the best of the author's knowledge, at the time of writing, this is the first time that a comparison between the different multi-point ODMR measurement techniques has been performed on the same experimental dataset.

4.6 Kucsko et al, 2013

The first reported case of using a multi-point ODMR experiment with the NV^- centre was reported by Kucsko *et al* in 2013 [35]. The group used a four-point ODMR measurement to monitor changes in temperature within a live cell system using a nanodiamond sensor [35]. The reported technique for temperature sensing

was to select four frequency points from a recorded CW ODMR curve, two from each side of the Lorentzian dip(s) (as in figure 4.11). A straight line fit was then used to describe the fluorescence intensity recorded from the two low-frequency measurements, and the two from the high-frequency measurements. The frequency at which these two lines intersected was then used to track changes in temperature within the cell [35]. The group initially tested the sensitivity of the measurement scheme by monitoring local increases in the temperature across a glass coverslip as heating was generated by the excitation of surface plasmons of gold-nanoparticles spin coated to the surface of the coverslip. The group were able to measure temperature changes as small as $\delta \mathrm{T} = 44 \pm 10 \mathrm{mK}$ using the nanodiamond probes [35].

This NV^- thermometry method was applied to the dataset described in section 4.5. The results of this analysis are shown in figure 4.12 and show the measured change in the resonant frequency of the NV^- ensemble as a function of the applied simulated temperature change. The graph shows that mean measured change in the resonant frequency across the seven measurements performed drops as the simulated temperature change applied increase. The error in these measurements is calculated by the standard deviation of these values. A linear plot has been fitted to the data to describe the relationship between the applied simulated temperature change and the measured change in resonant frequency. The gradient of the straight-line fit was $m = -0.96 \pm 0.15$. For a perfect system, we would recover a gradient of m_{ideal} = -1, so, from these results, this method would produced just a 5% error in the estimation of the applied temperature change. The limit of sensitivity for the calculation of the mean resonant frequency of the NV^- centre is set by the largest error, which in this case is $\delta \mathrm{D} = 530 \,\mathrm{kHz}$. This value is over three times the frequency step applied to produce the simulated temperature steps. Kucsko *et al* reported a much higher sensitiv-

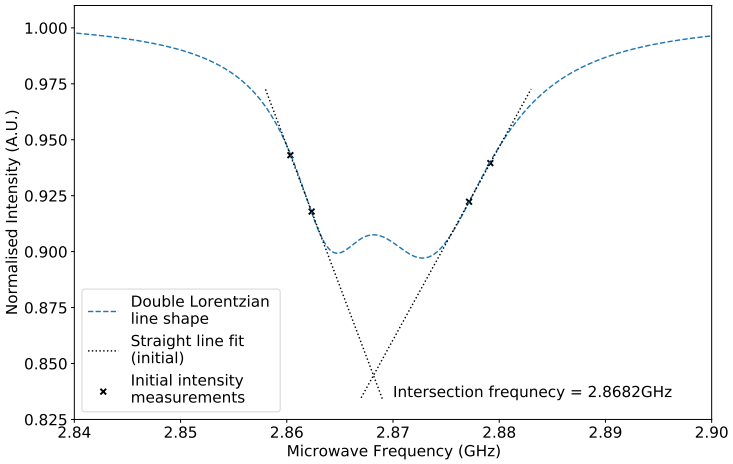

(a)

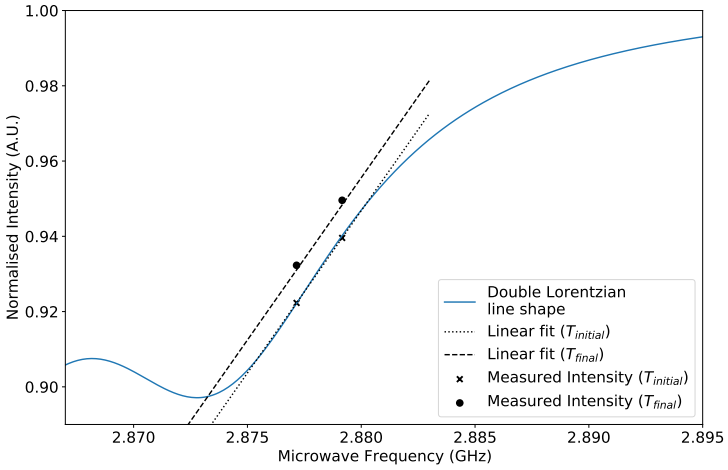

(b)

Figure 4.11: A demonstration of the Kucsko temperature sensing method. Here we see the four-point ODMR measurement results for a simulated dataset both before (figure 4.11a) and after (figure 4.11b) a temperature change is applied. In both cases a linear fit is applied to the two intensity points positioned either side of the central resonant frequency. The intersection point of the two linear fits gives the resonant frequency of the NV^- centre. This method is then used to monitor changes in the resonant frequency as a temperature change is applied as seen in figure 4.11b.

ity in their measurements, reporting the ability to measure temperature changes as small as $\delta T = 1.8$mK [35]. The group report using a confocal microscope system and an avalanche photo-diode for these measurements, which is a similar experimental set-up to our system. Before directly comparing these results, there are a number of points to consider that affect the performance of an ODMR measurement:

- **The fluorescent photon count rate used while performing the ODMR measurement:** Kucsko *et al* do not make it clear the fluorescence intensity that has been used in their measurements [35]. In a shot-noise limited system the noise scales as $\sqrt{N}$ [85], and therefore the strength of the fluorescent signal would have a significant impact on the sensitivity that can be achieved using their measurement protocol.

- **Depth of ODMR dip:** The ODMR spectra shown in Kucsko's paper [35] shows a contrast of 10%. This was roughly double the ODMR contrast that I was able to achieve when recording the measurements used for this analysis. The sensitivity of the NV^- sensor is inversely proportional to the contrast observed in an ODMR measurement, therefore, the greater the ODMR contrast, the smaller the change in temperature one is able to detect [133].

- **Our error analysis:** From the results in figure 4.12 we can see that the associated error of the measurement is quite large, however, given the quality of the linear fit, it is possible we are being conservative with our error estimation. We are not aware of another method of analysing the errors in our experiment that would allow us to use another metric other than the standard deviation in the 7 measurements made at each simulated temperature shift that would allow us to report a lower measurement error.

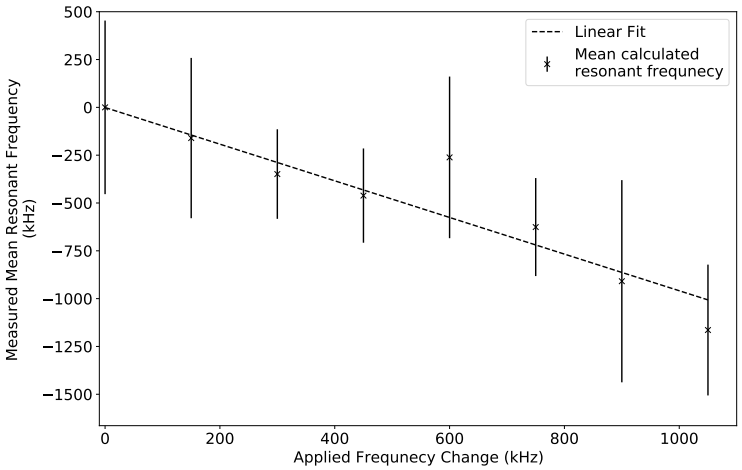

Figure 4.12: The measurement of the change in the measured resonant frequency of the NV^- centre cluster in a 70nm diamond during the simulated temperature sensing experiments. Here the mean resonant frequency measured over 7 measurement repeats can be seen to varying linearly with the change in the applied resonant frequency shifts. The error here comes from the standard deviation of the measurements recorded at each temperature point. The gradient of this straight-line fit is $m = -0.96 \pm 0.15$.

It is important to highlight the difference between the two sets of measurements to get an idea of how we might improve the sensitivity of our system in the future. Unfortunately, there was not time to explore options to improve the sensitivity of our system, and therefore, from these results, the size of the error that we recover using the Kucsko *et al* analysis method are too large to be able to reliably be able to perform NV^- based thermometry with our system.

4.7 Singam et al, 2019

Another multi-point ODMR analysis technique for NV^- based thermometry was presented in the paper of Singam *et al* in 2019 [4]. The group demonstrated that, by monitoring the fluorescence intensity from just two frequency points which describe the the point of maximum gradient of an ODMR curve, temperature

changes as small as 0.5 K can be detected in real time [4]. The process for performing the analysis presented by Singam *et al* is complex, and so is described in the bullet points below, and is represented graphically in figure 4.13.

1. Firstly, a complete ODMR curve is recorded from the nanodiamond in question. From the Lorentz fitting to the data, two microwave frequencies are chosen for the multi-point measurement. These points describe the point of maximum absolute gradient on either side of the Lorentz fitting (see figure 4.13a). These two frequency points should be selected such that they have equal (or as close as possible) fluorescence intensity when applied to the NV^- ensemble.

2. A differential curve is then generated from the complete ODMR curve. This curve is generated used in the following equation:

$$\delta I_i = I(f_{i+\Delta f}) - I(f_i) \tag{4.6}$$

   Where (i) is an index and δI_i is the difference in the normalised fluorescence of two different ODMR intensity measurements made at at applied frequencies f_i and f_j, in which the difference between the two frequencies is equal to δf as shown in figure 4.13a. As example of the central region of a differential curve is shown in figure 4.13b.

3. A linear fit is used to describe the central region of the differential curve (see figure 4.13b, $R^2 = 0.91$). Before any temperature changes are applied, the difference between the fluorescence intensity from the nanodiamond when the two chosen microwave frequencies should equal 0, $\delta I = I(F_-) - I(F_+) = 0$. This has been marked on figure 4.13c.

4. To perform temperature sensing measurements, the fluorescence intensity from the nanodiamond is monitored from the two applied microwave fre-

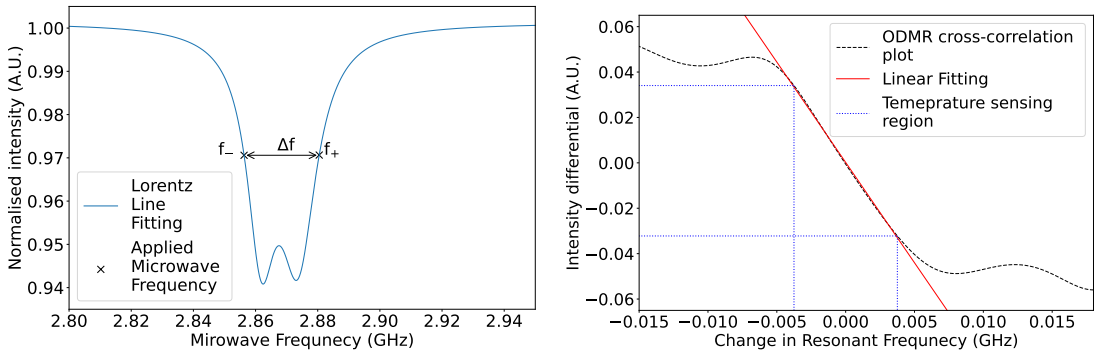

(a) (b)

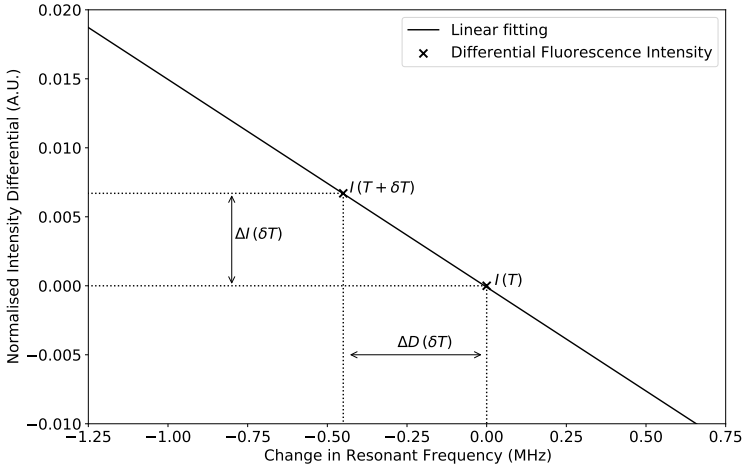

(c)

Figure 4.13: An graphical representation of the procedure used for temperature sensing as outlined in the paper by Singam *et al* [4]. The figure shows the selection of the two frequency points used for the multi-point ODMR measurement 4.13a. From these two points, the differential curve is generated and a linear fit applied to the near-linear region 4.13b. The linear fit is then used as a reference curve, in which any changes in the resonant frequency of the NV^- centre as a result of temperature can be calculated from the fluorescence intensity recorded from the two microwave frequencies selected for measurement 4.13c

quencies. Any shift in the ODMR spectra due to a change in temperature will be reflected in $\delta I \neq 0$.

5. Using the difference between the intensity measured for the two applied frequencies, one can use the linear section of the differential curve to calculate the magnitude of the temperature change, relative to a reference value (as shown in figure 4.13c) [4].

I evaluated the simulated temperature sensing dataset using the analysis method presented by Singam [4]. To apply this method as outlined in [4], I had to convert the four-point ODMR dataset into a two-point dataset. This was done by finding the mean fluorescence intensity for the two low frequency and two high frequency ODMR measurement points respectively. From this point the algorithm as describe above was implemented to determine the simulated temperature changes applied to the sample. The Singam *et al* analysis method proved to produce significantly smaller error than was seen in the Kucsko *et al* analysis method. As a result, the Singam method has been used to evaluate both:

- The results of a single four-point ODMR measurement recorded at each simulated temperature step
- The mean resonant frequency shift measured from all of the seven measurements recorded for each simulated temperature step.

4.7.1 Single measurement per Temperature Step

The analysis of a single four-point ODMR measurement per simulated temperature step can be seen in figure 4.14a. The graph shows a linear decrease in the measured resonant frequency as the simulated temperature change increased. The gradient for the linear fit applied to this graph is 1.04 ± 0.07. This gives a 4% overestimation, using this nanodiamond, for any simulated temperature

changes applied to the sample. The precision from this measurement is consistent for all the applied simulated temperature changes at $\delta\mathrm{D} = 340\,\mathrm{kHz}$, which is approximately double the actual simulated temperature shift applied for these measurements. The precision is given by the largest error in the dataset and is calculated using the following error equations,

$$\delta(\Delta I - C) = \sqrt{(\delta(\Delta I))^2 + (\delta C)^2} \tag{4.7}$$

$$\delta(\Delta D) = \Delta D \times \sqrt{\left(\frac{\delta(\Delta I - C)}{(\Delta I - C)}\right)^2 + \left(\frac{\delta \Delta m}{m}\right)^2}. \tag{4.8}$$

In the above, ΔI is the difference in the measured fluorescence intensity from the two frequency points, C is the y intercept, m is the gradient of the linear fit to the central region of the differential curve and ΔD is the measured simulated temperature change. As noted for the Kucsko *et al* data analysis, this individual measurement error is too high for accurate NV^- thermometry based off a single four-point measurement.

4.7.2 Singam analysis of Many Measurements

Figure 4.14b shows the results of the mean resonant frequency shift from the seven measurements made across all of the simulated temperature changes. A straight line fitting was used to determine the relationship between the measured and applied simulated temperature changes. The gradient of the fitting is 1.05 ± 0.04, in good agreement with the single shot measurement results. The error for this measurement was calculated as the standard deviation of the mean measured change in resonant frequency across the seven measurement repeats for each simulated temperature change. The maximum error in for the results in figure 4.14b is 93 kHz, this would be the equivalent to an error in temperature

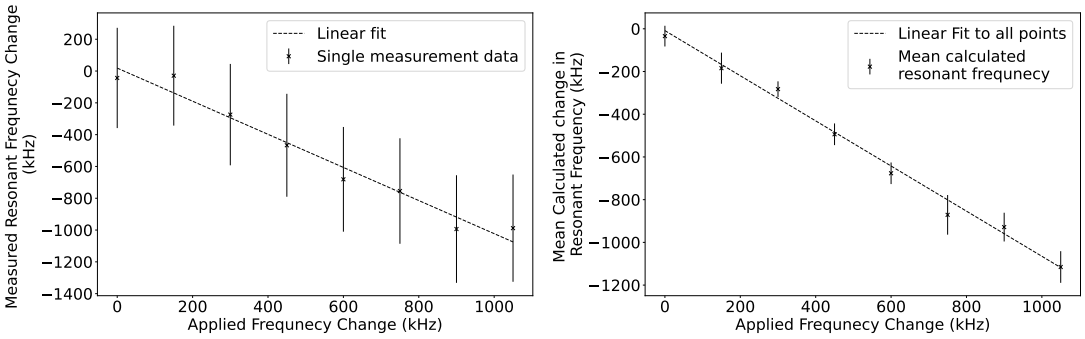

(a) (b)

Figure 4.14: Here the results of the temperature sensing using the Singam *et al* analysis method [4]. Figure 4.14a shows the results of a single four point ODMR measurement containing 250 point repeats for each of the applied microwave frequency. The measured resonant frequency shift of the NV^- centre due to the simulated temperature shift applied can be well modelled by a straight line fit ($R^2 = 0.97$). The gradient for the fitting is $m = 1.04 \pm 0.07$. Figure 4.14b shows the results of the mean microwave resonant frequency change for all seven data-sets recorded for each of the simulated temperature changes applied. A linear fit was also applied to model the results of this experiment ($R^2 = 0.99$). The gradient of this linear fit is $m = 1.06 \pm 0.04$. Errors for this plot come from the standard deviation in the measured microwave resonant frequency changes across the seven measurements recorded.

measurement of $\pm 1.24\,\mathrm{K}$ using the temperature dependence reported by Acosta et al of -74 $\mathrm{kHz\,K^{-1}}$ [37]. This analysis shows a three times improvement to the smallest detectable temperature change when compared to the method presented by Kuscko *et al*, and a move towards being able to detect sub-kelvin temperature changes.

4.7.3 Comparison to Results Reported in Literature.

When comparing our results to those published by Singam *et al*, the most obvious point for comparison would be the sensitivity of their NV^- thermometer. The authors quote a measurement accuracy of 0.5 K (approximately 38 kHz) for a single measurement lasting just 0.1 s [4]. This is a significant improvement on the sen-

sitivity we were able to achieve of 340 kHz in a measurement time of 32 s. When the differences between the two experimental set-ups is explored, we can identify some of the sources behind this discrepancy in sensitivity. In their paper, Singam *et al* report using a confocal microscope set-up with 1 mW laser power used to excite the NV^- centres [4]. This is significantly higher than the laser power used in our experiments ($\approx$10 µW), and would have resulted in a much higher emission rate from their diamond sample than was used in my experiments. The group also describe collecting the voltage-output from a photo-detector, rather than using a single-photon detector in Geiger mode, as we have done in our experiments [4]. We are only able to collect up to ≈ 2 million counts per second in the linear detection regime while operating in Geiger mode. Singam *et al* are able to used a much higher laser power and photon-flux while using the voltage-output from their detector, resulting in a larger signal to noise ratio, and resulting temperature sensitivity using a confocal microscope system [4].

Given the increase in the sensitivity of the measurements reported by Singam *et al*, one may question why it is that we are persisting with using the SPAD detectors operating Geiger mode for photon detection. The answer lies in the future application of the microscope. Singam *et al* were investigating the heating of micro-electronic circuits in their paper [4], so the maximum laser power applied to the sample does not need to be taken into account (beyond ensuring the electronics are not damaged by the laser) [4]. It does not make sense to optimise our sensing regimes for high photon-flux experiments as we intend to perform live-cell sensing experiments. The excitation laser power that we can supply to a live-cell sample will be limited to avoid inducing phototoxic effects [139]. If we were to try and perform thermometry experiments on an otherwise healthy cell with too high a laser power, we could end up impairing the cell's normal function, potentially damaging or destroying the cell [140]. The high quantum efficiency of

the SPADs allow us to perform live-cell imaging and ODMR experiments with a relatively low laser power ($\approx$10 µW). It is more productive, therefore, for us to focus on optimising the measurement regime for low-photon flux experiments as this is closer to the conditions of future use for the system.

4.8 Fujiwara Temperature Sensing

In 2020, Fujiwara *et al* published their method for temperature sensing using a four-point ODMR technique [1]. The group report being able to achieve an overall sensitivity of $1.8\text{K}/\sqrt{\text{Hz}}$ from thermometry experiments using a confocal microscope system and a single photon avalanche detector [1].

The process for the selection of the four applied microwave frequencies used in this data analysis has been described previously four-point ODMR data-set in section 4.5. The key assumption made in this selection process is that the two sides of the ODMR dip can be modelled by a linear fit. By assuming a linear relationship between the applied frequency and the fluorescence intensity measured in this region, one can describe the fluorescence intensity recorded from the four frequency points using the following equations:

$$I(f_1) = I(f_-) + m_1 \left(-\delta f + \delta B + \delta T \frac{dD}{dT} \right) \tag{4.9}$$

$$I(f_2) = I(f_-) + m_1 \left(\delta f + \delta B + \delta T \frac{dD}{dT} \right) \tag{4.10}$$

$$I(f_3) = I(f_+) + m_2 \left(-\delta f - \delta B + \delta T \frac{dD}{dT} \right) \tag{4.11}$$

$$I(f_4) = I(f_+) + m_2 \left(\delta f - \delta B + \delta T \frac{dD}{dT} \right) \tag{4.12}$$

In which, $I(f_\pm)$ is the intensity corresponding to the centre point of the linear

fitting to the CW ODMR curve, m_j is the gradient of the linear fits to the high and low frequency components of the ODMR dip. δB is the change in an applied magnetic field, and is assumed to be $\delta B = 0$ throughout this experiment [1]. δT is a change in temperature, and $\frac{dD}{dT}$ is the change of the resonant frequency with a change in temperature. A further assumption is made that the absolute value for the gradients of the straight line fittings are equal [1]. With these assumptions made, we are able to use the four equations above to generate the following expression for a given change in temperature:

$$\delta T_{NV^-} = \delta f \left(\frac{dD}{dT}\right)^{-1} \frac{(I(f_1) + I(f_2)) - (I(f_3) + I(f_4))}{(I(f_1) - I(f_2)) - (I(f_3) - I(f_4))}. \tag{4.13}$$

Using the dataset described in section 4.5, the suitability of this temperature sensing algorithm for use in our system was evaluated. The results of the analysis are shown in figure 4.15a for a single measurement recorded for each of the simulated temperature changes. The gradient of the linear fitting applied to the experimental data is $m = -0.93 \pm 0.06$. The error in this measurement comes directly from the propagation of the shot-noise error through the calculation in equation 4.13. The maximum error observed is δ D = 175 kHz, which results in a temperature sensitivity limit of give a limit of sensitivity to temperature changes of 2.33°C for a single shot measurement (32s total integration time). The maximum error reduces to 112kHz (1.5°C) in figure 4.15b for the mean measured change in resonant frequency from the seven measurements recorded at each simulated temperature shift. This error comes from the standard error in the calculation of the simulated temperature shift across the seven measurements made. The linear fit for the mean resonant frequency change has a gradient of -0.97 ± 0.05. For all the data analysed, this methodology applied to the mean simulated temperature sensing data produced the most accurate result of the simulated temperature change applied to the sample. This was the most accurate of the three methods investigated.

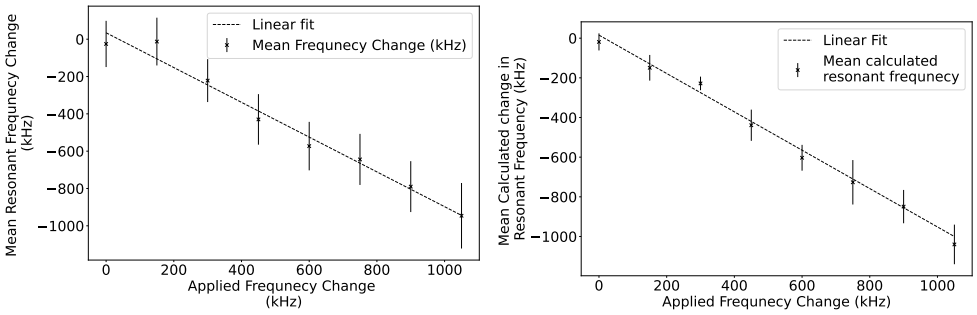

(a) (b)

Figure 4.15: Two plots showing the results of the Fujiwara analysis of the simulated temperature sensing for a single measurement recorded for each of the applied frequency changes 4.15a and the mean frequency change measured from multiple measurements made for each of the applied frequencies 4.15b.

The maximum error in the mean resonant frequency shifts measured is 112kHz from a total measurement integration time of 175s. In the work published by Fujiwara *et al*, they describe the sensitivity of their measurement as being:

$$\eta_T = \sigma_p \times \sqrt{2 \times t_{int}} \tag{4.14}$$

In which, σ_p is the standard error of recorded temperature shift across the measurement, and t_{int} is the total integration time of the measurement. If we take the mean of the errors in figure 4.15b we get that the standard error is σ_p = 73 kHz or (0.98°C). Using this value, the sensitivity of measurement from this data set is $\eta_T = 14.5\,\mathrm{K}/\sqrt{\mathrm{Hz}}$, which is approximately 8 times larger than the sensitivity reported by Fujiwara *et al* [1].

In table 4.4 I have documented the differences in the experiments conducted by Fujiwara *et al* and those that I have performed. In highlighting the differences between the two experimental protocols, I aimed to understand where the difference in the reported sensitivities arises, as both experiments are using confocal microscopy to perform nanodiamond based thermometry measurements.

Parameters	**Corbyn Experiment**	**Fujiwara Experiment**
ND size	70 nm	168 nm
NV Quantity	100 NV^-	900 NV^-
Fluorescence Intensity	0.86 MCounts s^{-1}	2.4 MCounts s^{-1}
ODMR Contrast	5%	12%
FWHM	5 MHz	10 MHz
Photon integration time	20 ms	100 µs
Point repeats	200	2380
Experiment Repeats	7	20
Total measurement time	112 s	38 s

Table 4.4: A comparison between the parameters in thermometry experiments performed by the author (Corbyn) and the work published by Fujiwara *et al* in [1].

There are some interesting differences between the two experiments that have been highlighted in table 4.4. First to note is the different size of NDs and the difference in the quantity of NV^- centres present in the nanocrystal. Fujiwara *et al* are using NDs that are slightly more than 2 times the size of the ones used in my experiment, and have 9 times the number of NV^- centre [1]. From previous discussions in this work, the more laser power used to excite fluorescence in the nanodiamond sample, the lower the ODMR contrast observed. This relationship was also reported by Fujiwara *et al* in their work [1]. By using larger nanodiamond crystals with more fluorescent defects present, the group can achieve a larger fluorescence intensity and a larger ODMR contrast than we would be able to achieve using our 70 nm diamonds. Indeed in the comparison table, we can see that Fujiwara *et al* were able to maintain a 2.5 times greater ODMR contrast than I used for my experiment while using a photon flux approximately 3 times that which I was able to achieve. This effect is unlikely to be solely down to the applied laser power used in these experiments, it is likely that the research group from Osaka also had a more efficient coupling of microwave power to their sample than I was able to achieve. The downside to having a significantly larger number of NV^- centres present in their nanodiamonds is the increase in the FWHM of

the ODMR dips due to the effects of spin mixing [141]. Using the values of fluorescence intensity, ODMR contrast and FWHM reported here, I was able to simulate the two experimental conditions using the double-Lorentz equation. The aim of this simulation was to extract the gradient of the quasi-linear region and calculate the relative uncertainty of the two measurements in terms of measuring the change in the microwave resonant frequency of the NV^- centre induced by an external change in temperature. For these simulations, the upper and lower limits used to define the "linear" portion of the Lorentz curve were:

$$Upper\ limit = 1 - (0.35 \times contrast), \tag{4.15}$$

$$Lower\ limit = 1 - (0.9 \times contrast). \tag{4.16}$$

Using these limits and the parameters as defined in table 4.4, I achieved the following relative errors from the two measurement regimes:

$$\delta D_{Corbyn} = \pm\ 103\ \text{kHz} \tag{4.17}$$

$$\delta D_{Fujiwara} = \pm\ 44\ \text{kHz}. \tag{4.18}$$

The higher fluorescence intensity and the larger ODMR contrast used by Fujiwara *et al* result in a 2.3 times improvement to the 4-point ODMR temperature sensing protocol in the modelled systems. I have made the assumption here that both experimental set-ups were shot-noise limited in the computational analysis of thermometry performance [85]. If we include the 1.76 pre-factor we know from the evaluation of the microscope performance that exist in our measurement system with a dwell time of 20 ms, then this effect would account for a decrease in the sensitivity of our system by a factor of 4.04. This still leaves roughly a factor

of 2 loss in sensitivity that is not accounted for in the discrepancy between our measurements and those reported by Fujiwara *et al* [1]. The final piece of the jigsaw could be attributed to the number of experimental repeats performed during the temperature sensing protocol. The accuracy of a measurement increases as a function of the square root of the number of experimental repeats performed. In their work, Fujiwara *et al* describe using an average of 20 experimental repeats to perform their temperature sensing analysis. This compares to the 7 experiment repeats used in the experiments performed here. The ratio of the square root of the two experimental values is 1.6, which is in line with the remaining discrepancy between the sensitivity of the two measurements. Having identified all the areas of difference between the two measurements, I am confident that we could reproduce the results of [1] given access to the same nanodiamond material and obtaining a similar ODMR contrast from our measurement system.

4.8.1 Further Investigations

The only remaining substantive difference in the way that the two experiments were conducted is that Fujiwara *et al* have used significantly more point repeats per applied microwave frequency than was used in our measurements, at the expense of the total photon integration time [1]. After a lengthy discussion between myself and Dr. Patton, we managed to convince ourselves that neither the number of repeats nor the photon integration time are a limiting factor to the sensitivity of an ODMR measurement, only the total number of photons detected (N). The logic used for this conclusion is outlined in the following worked examples:

Example 1

If we consider a system with: a photon detection rate of of $I = 10^6 \mathrm{s}^{-1}$, a total integration time of $t_{int} = 1s$, and just a single measurement performed, then we

obtain:

$$\sigma = \delta I = \sqrt{I_{tot}} = \sqrt{10^6} = 10^3. \tag{4.19}$$

This in turn leads to a fractional error of:

$$\frac{\delta I}{I_{tot}} = 10^{-3}. \tag{4.20}$$

Example 2

We will now consider the same system, however the integration time has been dropped to $t_{int} = 10^{-4}$s, resulting in a measured photon flux of $I_{short} = 100$, and the number of repeats increased to $n = 10^4$. We now consider the standard error of the photon counts recorded across all repeats as the error for the measurement. As the standard deviation of the photons detected per measurement is $\sqrt{I_{short}}$ from the shot noise approximation [85], we obtain an error of:

$$\sigma = \delta I = \frac{\sqrt{I_{short}}}{\sqrt{n}} = 10^{-1}. \tag{4.21}$$

Which leads to a fractional error of:

$$\frac{\delta I}{I_{short}} = 10^{-3} \tag{4.22}$$

Which is equivalent to that of example 1. Thus we determine that the total photons recorded is the most important factor in determining the precision of an optical shot-noise limited temperature sensing experiment.

We wanted to test this hypothesis using our experimental system and the multi-point ODMR experimental protocol. The reasoning at the time was to rule out that the number of repeats used by Fujiwara *et al* was not a contributing factor to the increased sensitivity that they had reported [1]. For context, this investigation was conducted before all the previous mentioned contributing factors

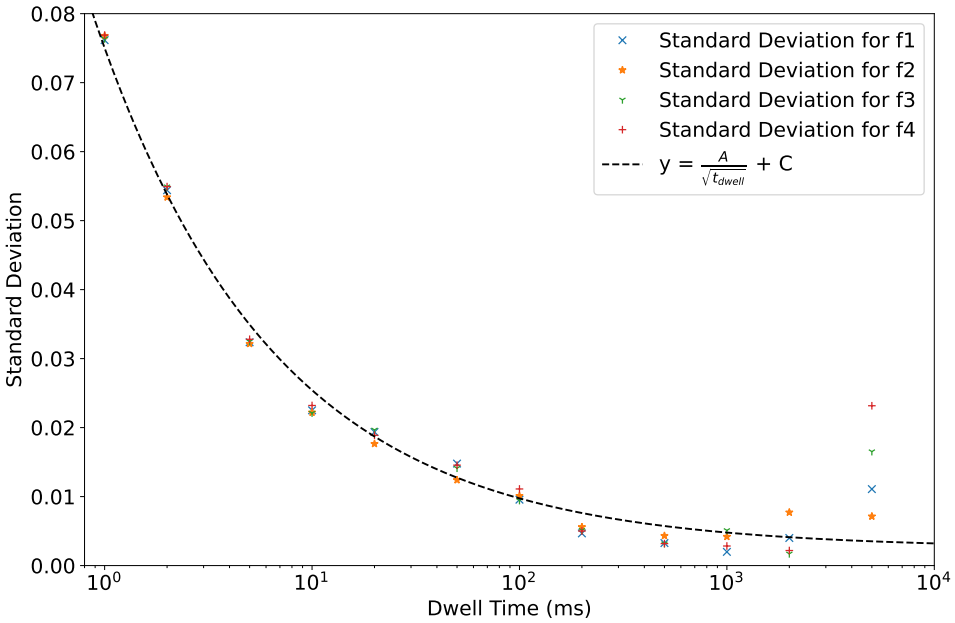

Figure 4.16: Standard Deviation vs dwell time for the four applied frequencies.

had been identified. The experimental protocol for this experiment was to conduct a four-point ODMR measurement in which the total photon counting time for the measurement remained constant (at 40 s) while the photon integration time per frequency point repeat and the number of frequency point repeats were varied respective to one another. The standard deviation and standard error for each of the measurements was investigated to see how these values changed as the photon integration time per frequency point repeat was decreased from 5 s down to 1 ms.

Standard Deviation Measurements

Figure 4.16 shows how the standard deviation for the fluorescence intensity from the NV^- cluster within the nanodiamond varies with the photon integration time (dwell time) per applied microwave frequency measurement changes. The

standard deviation used was calculated using the following formula:

$$\sigma = \sqrt{\frac{\Sigma(x_i - \bar{x})}{n}} \tag{4.23}$$

In which x_i is the normalised intensity value recorded for each of the applied microwave frequencies. $\bar{x}$ is the mean value for the normalised intensity for the applied microwave frequency and n is the number of point repeats per applied frequency (250). Initially, when the dwell time is decreased from 5 s - 0.5 s, we see that the standard deviation decreases to a minimum. This is most likely the result of moving towards a statistically significant number of samples for an accurate calculation of the standard deviation. As the dwell time decreases from 500 ms to 1 ms, the standard deviation increases proportionally to $\frac{1}{\sqrt{t_{dwell}}}$. This most likely reflects the Poisson statistics of photon counting, in which the error associated with photon counting is proportional to $\frac{1}{\sqrt{N}}$. As I have used a constant laser power and photon detection rate throughout these measurements, the number of photons (N) detected is linearly proportional to the photon integration time (dwell time) used [85].

Standard Error Measurements

The results of the investigation to see how photon integration time affects the standard error of a four-point ODMR measurement if the total photon-collection time remains constant by increasing the number of photon detection repeats per applied frequency can be seen in figure 4.17. The standard error (SE) was calculated for the measurements using the following formula:

$$SE = \frac{\sigma}{\sqrt{n}} \tag{4.24}$$

In which σ is the standard deviation as defined in equation 4.23 and n is the number of repeats per applied microwave frequency (250). The results in

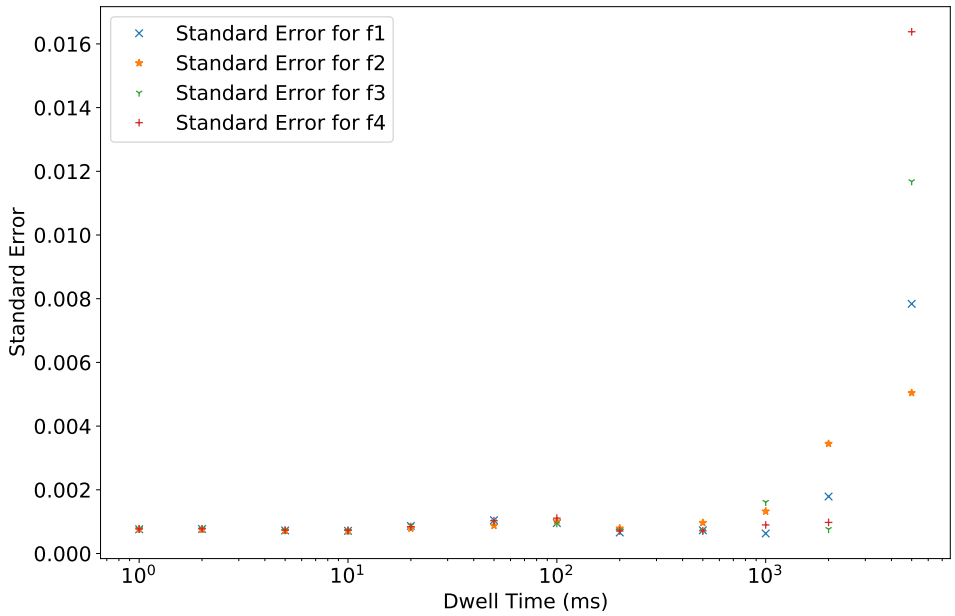

Figure 4.17: Standard error vs the dwell time for each applied frequency.

figure 4.17 from this experiment show that once dwell time was reduced beyond 500 ms (20 point repeats per frequency), there was no further improvement to the measurement of the standard error. The results of this experiment show that for a photon detection rate of $1.10 \pm 0.15 \mathrm{MCountss}^{-1}$ and a 40 s ODMR frequency integration time, the minimum for the standard error of the measurement is 0.00076 normalised counts per unit dwell time. These results also show that the total photons detected in a measurement are the most important factor in determining the sensitivity of a four-point ODMR measurement, and not the number of repeats performed in a shot-noise limited system.

4.9 Summary

In the above chapter I have considered how the CW ODMR protocol could be modified for use in biological systems. In the first instance, I looked to see how aberration correction affects the quality of an ODMR measurement. In these measurements I used the deformable mirror to gradually apply increasing amounts of a chosen aberration to the confocal imaging system and recorded an ODMR measurement to see how the spectra was affected. The results showed that the shape of the ODMR curve did not appear to change as the magnitude of an applied aberration was increased. What we did see is that the recorded fluorescent signal during the ODMR measurement decreased as the applied aberration modes increased in magnitude. This is consistent with what is seen when imaging through a sample induced aberration using a confocal system [71]. This is an interesting result in relation to biological sensing using the NV^- centre because, as discussed previously, the sensitivity of the nanodiamond probes is inversely proportional to the square root of the recorded fluorescence intensity from the nanodiamond [44]. In the cases in which the NV^- centre is to be utilised for *in vivo* biological sensing, the application of adaptive-optics can help to improve the signal to noise ratio of the measurement, therefore improving the sensitivity of a measurement.

The bulk of the work in this chapter has focused on the implementation of a four-point ODMR measurement protocol that would allow faster NV^- based thermometry experiments to be performed. The four-point measurement system was compared to the results of a CW ODMR measurement, with the accuracy and precision of the measured intensity from the four applied frequencies compared to the Lorentz fitting used to fit the original CW ODMR plot. Having confirmed that the four-point ODMR measurement system gives a reliable sample of the microwave frequency dependent fluorescence intensity, I developed the

simulated temperature sensing protocol that allowed me to test the application of three different temperature algorithms using our system. Using the same dataset I have evaluated three different multi-point ODMR temperature sensing techniques outlined in the papers published by Kucsko *et al*, Fujiwara *et al*, and Singam *et al* [35, 1, 4] for use in our measurement system. Both the Singam *et al* and Kucsko *et al* temperature sensing algorithms resulted in similar estimations of the applied frequency shift with a 5% error in the relation between the applied and measured simulated temperature shifts. The most accurate of the three thermometry analysis techniques applied was that of Fujiwara *et al*, this method produced just a 3% error in the measurement of the applied simulate temperature shift. From these results, I would recommend using the Fujiwara *et al* method for temperature sensing using the four-point ODMR measurement system [1]. This is because not only did this method produce the most accurate measurement of the simulated temperature shift, but also because the analysis method works independently of the depth of the original ODMR curve. As will be discussed further, in section 5.3, when exposed to laser power over a long period of time, the ODMR contrast from the same diamond can change, even if all other experimental parameters are kept constant. By having a measurement system that is only reliant on a single ODMR measurement for applied four point frequency selection and nothing else, we have a thermometry system which is robust against changes in the ODMR spectra from the nanodiamond probe. The drawback of the Fujiwara thermometry method is that it is reliant on using a symmetrical ODMR spectra for measurement, which can limit the number of nano-crystals in the sample which can be used for thermometry measurements.

Chapter 5

ODMR in Fixed-Cells

5.1 Introduction

In the previous sections, I have outlined the development of an ODMR protocol that would allow us, in the future, to investigate changes in magnetic field and temperature within live cell samples. The natural next step in the development of these protocols was to investigate the performance of magnetic field and temperature sensing capabilities of nanodiamonds embedded within fixed-cell samples. In collaboration with the Centre for Inflammation Research at Edinburgh University, we gained access to two different cell lines that had our nanodiamond colloidal mixtures added to the growth media. The immune cells were found to readily incorporate the nanodiamonds into the cell body, allowing us to perform ODMR measurements on nanodiamonds with a cell body. The exact mechanism for nanodiamond uptake in the cells used in this study was not examined. Previous research has shown that endocytosis is one of the key routes for the uptake of nanodiamond into the cell body, however, uptake dynamics such as passive diffusion is not ruled out [142, 143].

The cell lines embedded with nanodiamond I had access to during this research porject were:

- Macrophage cells embedded with 20 nm diamond crystals.
- Macrophage cells embedded with 90 nm diamond crystals.
- THP1 cells embedded with 70 nm diamond crystals.

The macrophage is a key part of the immune system's ability to combat infection [144]. In a process called phagocytosis, macrophage cells engulf viruses and other sources of infection within the body [145]. The macrophage then breaks the pathogen down using phagocytic enzymes, and eventually, the remains of the destroyed pathogen are exctreted from the cell in a process called exocytosis [145]. The macrophage also plays an important role in the inflammation response during infection, which is a key component of an effective immune response [146]. Macrophages can be found in almost every area of the human body [145], the cell line that used in this work were monocyte derive macrophage cells.

The THP1 cell is a monocyte cell-line derived from a patient with acute monocytic leukaemia [147]. These monocytes are also associated with the immune response, and are able to differentiate upon maturity to macrophage cells [148].

With these samples, I was able to test the magnetic and temperature sensing protocols that I developed over the course of this research project on nanodiamonds embedded within biological material. In the following chapter, I will discuss the experiments performed and the results of experimentation.

5.2 Macrophage Imaging and Magnetic Field Sensing

In the first instance, we wanted to make sure that it was possible for us to image nanodiamonds when they are embedded within biological material. For the initial

tests of this, Dr Patton, Dr Johnstone and I imaged a macrophage cell with the 90 nm diamonds embedded within its structure. The macrophage cells had been grown for 2 weeks using the method outlined in [149]. In the final 2-3 days of macrophage growth, the nanodiamond colloidal was added to the growth media for uptake within the macrophage structure. The diamonds were not labelled with any anti-body or chemical labelling, so did not preferentially attach themselves to any of the organelles within the cell [30]. The cells were grown on a glass coverslip and fixed before imaging. The sample had been prepared 6 months prior to our experiments, and previously used for confocal imaging. We were able to recover the macrophage coated coverslip and prepare the sample for ODMR experiments using the preparation routine outline in 3.4.2. The immersion media used during sample preparation was Prolong Gold. It was not known at the time of imaging whether the macrophage cell had degraded beyond the point at which auto-fluorescence from the cells might dominate imaging, meaning we would not be able to resolve the nanodiamonds within [150]. The first ND labelled macrophage cell image we recorded can be seen in figure 5.1. The imaging conditions for this measurement were:

- laser power = 35 µW at the back-focal plane of the objective.
- Pixel dwell time = 1.5 ms.
- Averages per frame = 2
- Scan range = 30 µm × 30 µm × 9 µm.
- Voxel size = 200 nm × 200 nm × 300 nm

We can see that this initial macrophage sample used for imaging is very densely populated with nanodiamond. This was typical of the nanodiamond uptake seen across the cells within this sample. This was a positive sign for us

as it showed that macrophages will readily uptake nanodiamond crystals into the cell. The quantity of nanodiamonds in the cell structure proved to be a difficulty when trying to perform ODMR measurements as the cell was so densely populated that it proved to be difficult to isolate a single ND on which to perform ODMR experiments.

We decided to use the macrophage sample which had been grown with a lower density of the 90 nm diamond colloidal added to the growth media at roughly a tenfold lower concentration compared to the above cells, added to the growth medium. The sample with a lower concentration of nanodiamond had also been prepared 6 months previously and was recovered for imaging in the same way as the macrophage sample grown in the dense nanodiamond mixture. A confocal image of one of these macrophage cells can be seen in figure 5.2. In this more sparsely populated macrophage sample, I was able to identify a single nanodiamond within the cell and recorded an ODMR measurement from the sample. This measurement can be seen in figure 5.3a. From this diamond, we obtain a magnetic DC sensitivity of $12 \pm 2\,\mu T/\sqrt{Hz}$. Through the fitting of the double Lorentzian curves, I was able to determine that: the FWHM for the two ODMR dips are 14 ± 1 MHz and 11 ± 1 MHz respectively for the lower and higher frequency resonant spin-transitions. This was found to be approximately in line with the FWHM observed for nanodiamonds drop-cast onto the glass coverslip in previous measurements. The splitting between the resonant microwave frequency of two spin-state transitions was 12.2 ± 0.5 MHz, this loss of degeneracy between the $|\pm 1\rangle$ spin-states is most likely the result of strain within the crystal, as no magnetic field was applied [28].

The sample was stable enough that I was able to place a neodymium magnet on the sample stage, applying a static external magnetic field to the sample. I then repeated the ODMR measurement on a different nanodiamond to see if we were able to observe Zeeman splitting in the recorded ODMR spectra. The re-

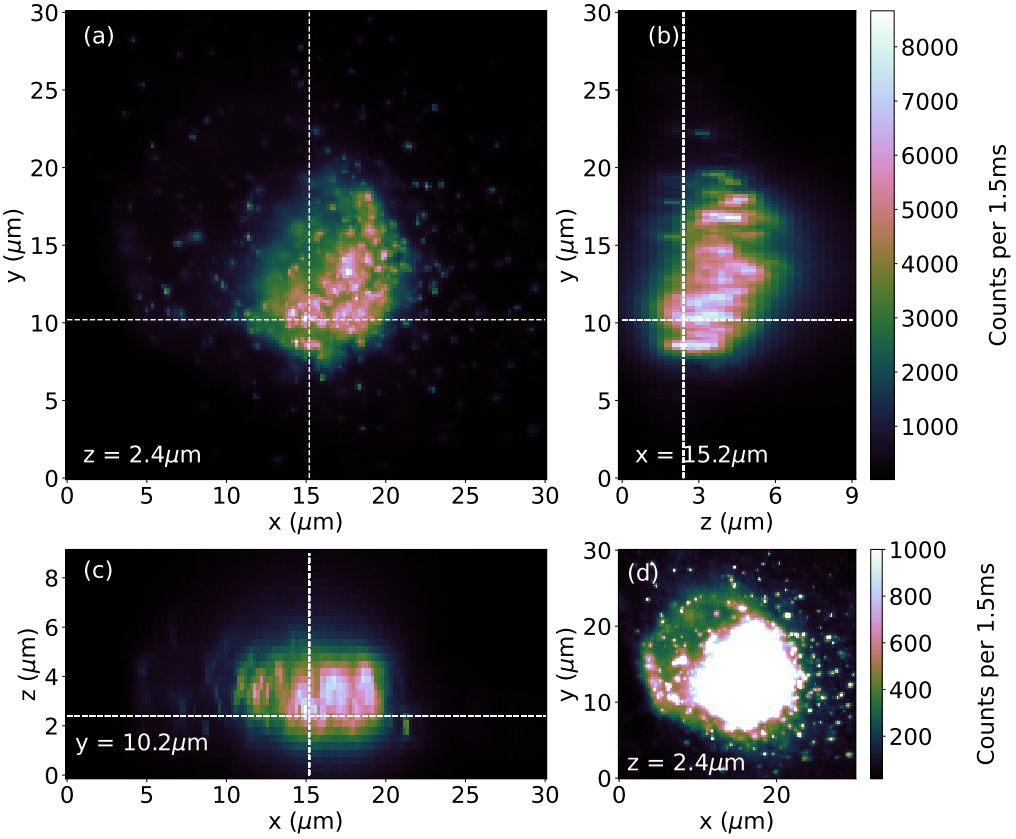

Figure 5.1: A tri-image of a 3D confocal image of a macrophage with 90 nm diamonds embedded within the cell (figures (a), (b), (c). Figure (d) shows the same XY scan as in figure (a), however the maximum brightness of the image has been reduced to clearly show the nanodiamonds within the cell structure.

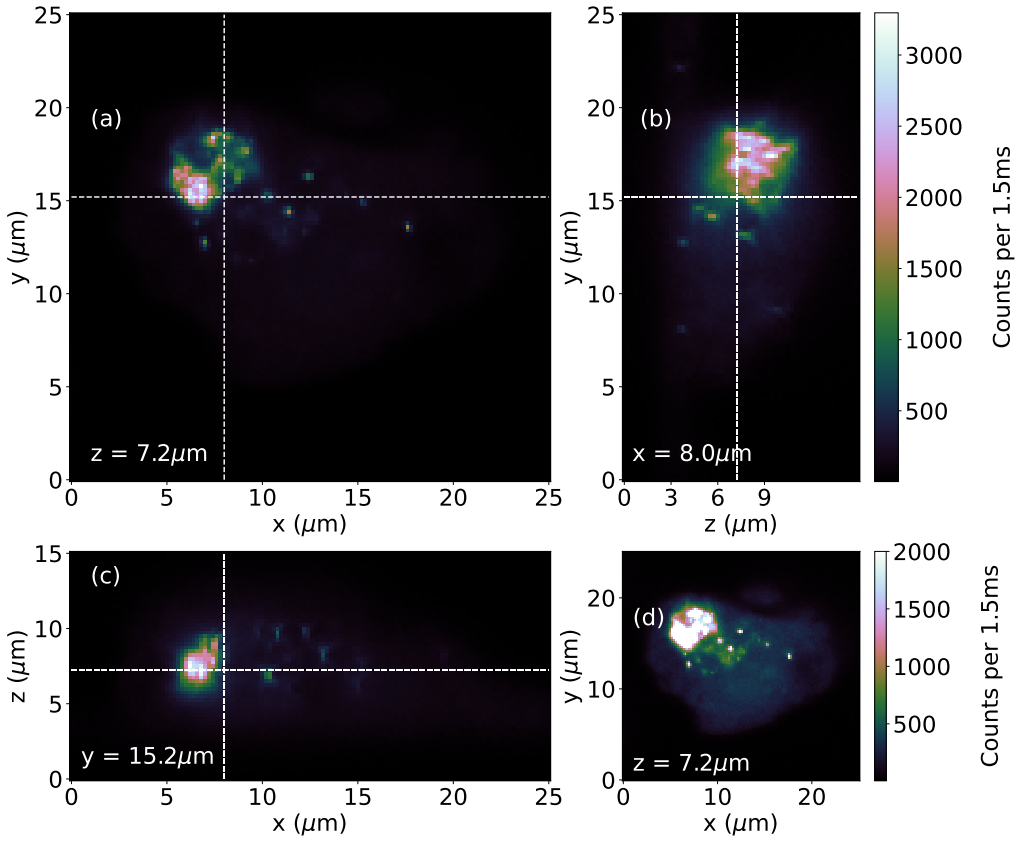

Figure 5.2: A tri-image of a 3D confocal image of a macrophage with 90 nm diamonds embedded within the cell (figures (a), (b), (c). Figure (d) shows the same XY scan as in figure (a), however the maximum brightness of the image has been reduced to clearly show the nanodiamonds within the cell structure.

sults of which can be seen in figure 5.3b. Indeed I was able to observe the effects of Zeeman splitting within the ODMR spectra. Interestingly, we are only able to see one pair of ODMR dips in the measurement. We would expect from the 90 nm diamonds, with > 500 NV^- centres, randomly distributed along the four possible crystallographic orientations of the NV centre, that the application of a magnetic field would result in a minimum of 2 distinct pairs of ODMR dips [105]. Upon further reflection, the most likely reason for the results in figure 5.3b, is that we were actually imaging a macrophage cell that had been grown in an environment with 20 nm diamond. My reasoning behind this is that the 20 nm diamonds only have 1 NV^- centre present, and therefore, we would only recover 1 pair of ODMR dips were a magnetic field applied. At the time of growth, the samples were prepared more for the purposes of proof of principle experiments, rather than rigorous scientific study. Given the shape of the ODMR curve, I would suggest that this is a likely interpretation of the results of this experiment, however, they are still sufficiently promising to warrant inclusion in my thesis to prove the concepts. The diamond colloidal sent to Edinburgh for use in the growth media of the immune cells were in eppendorfs with the diamond size written on the eppendorf itself. It is easy to see how those in a biology lab, unfamiliar with the distinction between the samples, could have mislabelled a sample. Equally, the fault could have occurred in our lab when recovering the sample from its original imaging set-up for use in ODMR measurements. Following these experiments, a much greater care was taken when preparing samples for ODMR measurement.

The Zeeman effect from the applied magnetic field caused the spin-state transitions to be split by 47.5 ± 0.1 MHz, which would be equivalent to a magnetic field strength of 847.6 ± 0.2 µT, orientated along the NV^- axis, applied to a strain free crystal. From figure 5.3a, we know that this crystal has internal strain equivalent to a frequency splitting of 12.2 ± 0.5 MHz in the ODMR spectra. We do

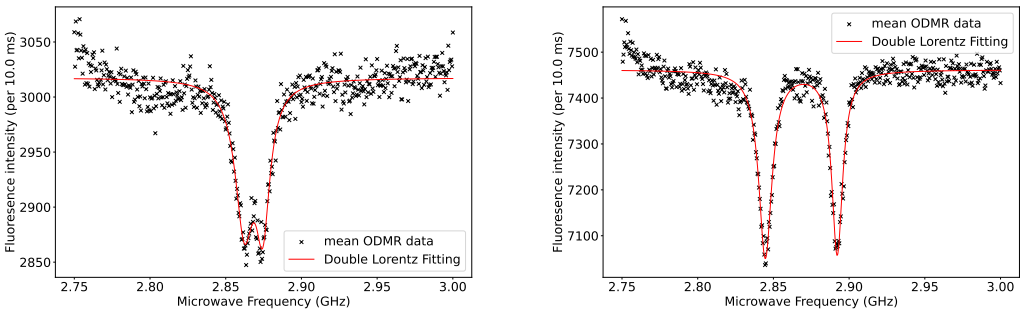

(a) (b)

Figure 5.3: ODMR measurements recorded from nanodiamonds within the same fixed Macrophage cell. Figure 5.3a shows the ODMR spectra before a magnetic field was applied to the sample, and figure 5.3b was recorded with a magnetic field applied.

not know if the magnetic field applied to the sample is parallel or anti-parallel with the NV^- centre, and therefore, we can't tell if the applied magnetic field is compensating for, or accentuating the strain induced splitting. When incorporating the error in magnetic field strength measurement due to the crystallographic strain of the diamond, we find that the applied magnetic field is estimated to be $800 \pm 200\,\mu T$. The full width half maxima of the two ODMR dips are $10.5 \pm 0.3\,MHz$ and $8.7 \pm 0.3\,MHz$ respectively for the lower and higher microwave frequency spin-state transitions. The magnetic DC sensitivity from this measurement is calculated to be $5.1 \pm 0.3\,\mu T/\sqrt{Hz}$. The improvement in sensitivity is the result of an increase in the observed fluorescent signal from this diamond relative to the measurement in figure 5.3a.

These results showed that our system is capable of performing ODMR measurements on nanodiamonds embedded within cellular material. Assuming it is the case that a 20 nm diamond was used for this study, these results are very promising. With the lowest signal to noise of any of our diamond samples, the fact that we were able to image and record ODMR from the 20 nm diamond shows that the ODMR protocols that I had developed and our imaging system

were robust enough for biological imaging and magnetic field sensing.

5.3 Simulated Temperature Sensing in TPC1 Cells

Towards the end of the project, I received the THP1 cells that had had 70 nm diamonds added to the growth media. We requested that these samples be grown as the previously used macrophage samples had degraded to such a point that they could no-longer be used for imaging. With these cells I tested the simulated temperature sensing protocol on the nanodiamonds within a biological sample. A confocal image of the cell used for this study can be seen in figure 5.4. In this image we can see that the nanodiamonds are sparsely distributed throughout the cell's structure, which was to be expected as the ratio of ND to growth media was 200:1, resulting in a lower concentration of nanodiamond for the cells to uptake. After ensuring that it was indeed possible to image the nanodiamonds within the cell structure, I chose one nanodiamond within the cell to perform the simulated temperature sensing experiments on, as outlined in section 4.4. The experimental protocol used was as follows:

- Fluorescence intensity from the diamond maintained at 700 kcounts per second throughout the experiment, with no change to applied excitation laser power.
- The microwave power at the output of the microwave amplifier was 3.16 W (35 dBm), throughout the experiment.
- The number of point repeats recorded per applied microwave frequency was 250, with a photon integration time of 25 ms.
- The frequency shift used to simulate the effects of a change in tempera-

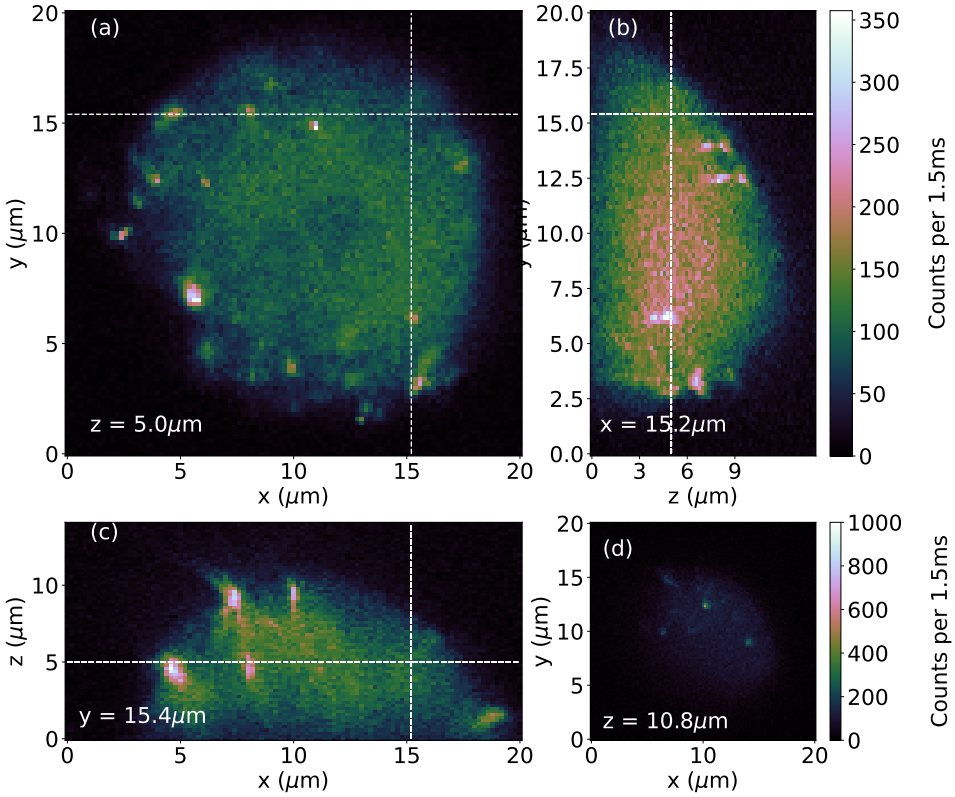

Figure 5.4: A tri-image of a THP1 cell embedded 70 nm diamond crystals embedded in the cell structure. Figures (a) and (d) both show XY cross-sections of the THP1 cell, from different z positions, showing that the nanodiamonds are distributed throughout the cells structure.

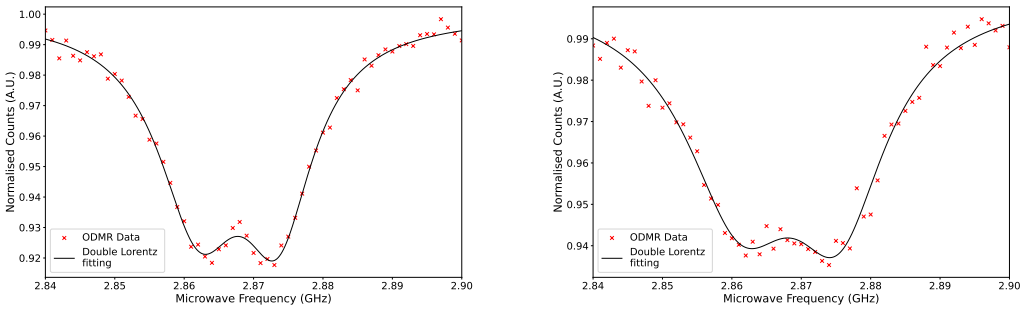

(a) (b)

Figure 5.5: Full ODMR spectra recorded from a 70 nm diamond embedded within a THP1 cell. Figure 5.5a shows an ODMR spectra recorded before the simulated temperature sensing measurements were conducted and figure 5.5b shows the spectra from the diamond after these measurements.

ture was 150 kHz, which is equivalent to 2 K temperature change using the temperature dependence published by Acosta *et al.*

- The range of simulated temperature change used for this measurement was from 0 kHz to 900 kHz (0 K - 12 K). For each simulated change in temperature, the four-point ODMR measurements was repeated 5 times.

The results of these measurements can be seen in figure 5.6, in which the mean measured resonant microwave frequency shift is plotted as a function of the simulated change in temperature. To analyse the results of the simulated temperature experiment, I have applied the Fujiwara *et al* temperature sensing technique, as outlined in section 4.8 and in [1].

The gradient of the linear fit applied to this dataset is -0.80 ± 0.12. It is promising to see that we are able to recover a linear relationship between the applied and measured frequency shifts when measuring frequency shifts through biological material. The measurement accuracy of the applied frequency shift during these measurements has dropped by 15% in comparison to the results recorded for nanodiamonds drop-cast onto the surface of a glass coverslip. From

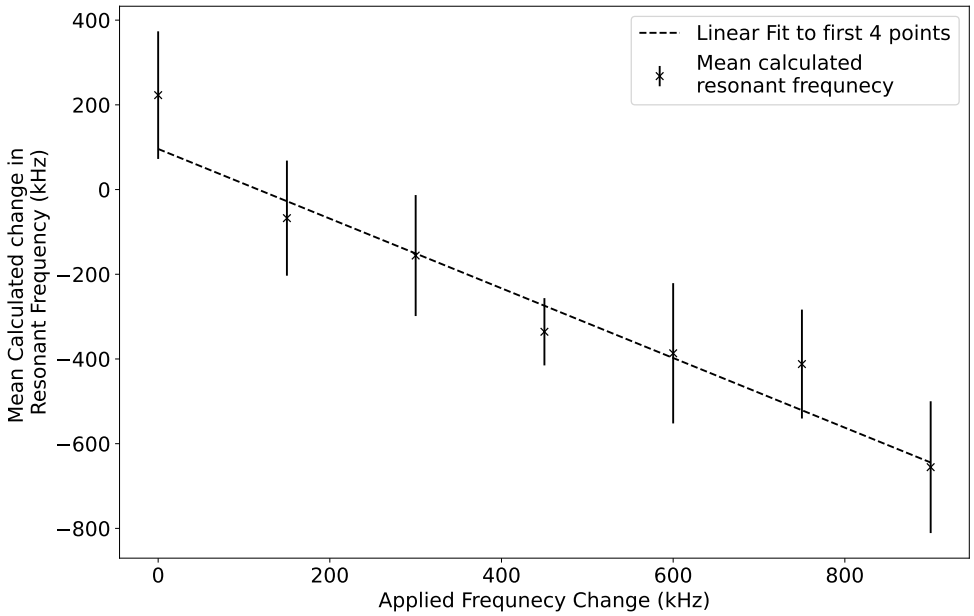

Figure 5.6: The results of the 4-point simulated temperature experiments conducted from a 70 nm diamond embedded within a THP1 cell.

this measurement and using the equation 4.14, we obtain a temperature sensitivity for this measurement is $\eta_T = 28.8\,\mathrm{K}/\sqrt{\mathrm{Hz}}$, which is approximately a factor of 2 drop in the sensitivity of the nanodiamond probe than was achieved using samples in which the nanodiamond probe was drop-cast to a glass coverslip (section 4.8). A possible explanation for this discrepancy is presented in figure 5.5, in which the complete ODMR spectra recorded before and after the simulated temperature experiments are shown. Interestingly, the ODMR contrast dropped by approximately 2%, and the FWHM for the ODMR curve have increased from 9.9 MHz to 12.8 MHz between these two measurements. Both of these changes to the ODMR spectra would result in a loss of sensitivity in the detection of simulated temperature changes [1]. This result was unexpected. I had not previously seen a change in the ODMR spectra from nanodiamonds that has been drop-cast onto the glass coverslips. This suggests that this phenomena may have something to do within the environment that the nanodiamonds find themselves in within the cell. One possible explanation for the change in the ODMR spectra shape would be the formation of, or chemical/structural change to, a protein corona on the surface of the nanodiamonds under illumination of the 532 nm excitation laser [151]. The formation of a protein corona around the surface of the ND centre would bring complex chemical compounds into close proximity to the near-surface NV^- centres, which could result in an increase in the dephasing and/or spin-relaxation rate of these NV centres and a loss of the ODMR contrast and an increase in the FWHM of an ODMR measurement [152].

This change in the ODMR shape of the ODMR spectra presents an interesting problem for analysis of any ODMR thermometry experiments. The Singam *et al* temperature sensing method is reliant on having a stable ODMR spectra from the NV^- ensemble to record changes in temperature [4, 35]. On the basis of these results, the Singam *et al* temperature sensing algorithm would be a poor choice

for tracking changes in temperature within a live-cell system, in which similar effects may be seen [4]. The temperature sensing methodology produced by Kucsko *et al* was found to produce significantly higher errors that the Singam or Fujiwara methods when analysed previously using our system in section 4.6, so is also likely a poor choice for us in terms of live-cell temperature sensing [35]. This leave just the temperature sensing technique presented by Fujiwara *et al*, which is not dependent on keeping a constant ODMR spectra shape for temperature sensing, as long as the four applied microwave frequencies remain within the quasi-linear region of the ODMR dip [1]. It is important to remember though, that the sensitivity of the NV^- ensemble to temperature changes will drop as the ODMR contrast decreases and the FWHM of the spectra increases [37]. As evidence of this, between the beginning and the end of this experiment, the DC magnetic sensitivity of the probe dropped from $3.1 \pm 0.2\,\mu T/\sqrt{Hz}$ to $9 \pm 2\,\mu T/\sqrt{Hz}$. Unfortunately, there was not time remaining to further explore the dynamics of the change in the shape of the recorded ODMR spectra. If this phenomena occurs rapidly after the ND is illuminated by an excitation laser, then it may be that this effect can be compensated for simply by waiting 5 minutes with the nanodiamond under constant illumination before the reference ODMR measurement is performed. If these dynamics are slow, this presents a more complicated problem. If this is the case, CW ODMR is perhaps a more appropriate method of monitoring temperature changes within cells, so an accurate determination of the measurement sensitivity can be made.

There was much to learn from the results of this experiment. Firstly, we are able to report that we were successfully able to use the Fujiwara *et al* analysis technique to monitor the effects of the simulated temperature change on the measured resonant frequency of the NV^- centre from a nanodiamond inside a fixed cell. Secondly, we have identified that the Fujiwara *et al* method for NV^- ther-

mometry is the most compatible thermometer technique reported to date for use in our measurement system. Finally, we have seen that the ODMR spectra from the NV^- ensemble used throughout this measurement changed across the duration of the measurement. While the source of the change in the ODMR spectra has not been confirmed due to project time constraints, it presents an interesting avenue for further research and has wider implications for the sensitivity of NV^- based thermometry, as discussed above.

5.4 Summary

In the work presented in this chapter I have outlined the results of experiments in which nanodiamonds embedded within fixed immune cells were used to monitor the strength of an applied magnetic field, and the ability to measure the effects of a simulated temperature change. For 90 nm diamonds within a macrophage cell, I was able to show that I was able to measure the Zeeman splitting introduced to the ODMR spectra of the NV^- ensemble by an externally applied magnetic field. This is encouraging as an indication that we may be able to apply our measurement technique to monitor the magnetic fields generated by live-cell systems, such as that produced by a neuron when firing [34]. I was also able to monitor the effects of a simulated change in temperature using a nanodiamond embedded within the structure of the THP1 cell. This again is an encouraging step in the development of our measurement protocols, as I have shown we have the capability to measure temperature changes as they occur within a biological sample. These proof of principle measurement show that, given more time, the protocols outlined within this thesis could be used to monitor the magnetic-field or temperature dynamics of a live-cell system.

Chapter 6

Conclusions

6.1 Conclusions

The work presented here is the culmination of three years of work in which I have explored the application of NV^- quantum sensing to monitor temperature changes and magnetic fields within single cell environments. In this chapter I will highlight some of the key learning outcomes, practical skills developed and my contribution to the progression of this research project. The following will be split into three sections to reflect the key aspects of the work presented here. These sections are:

- Optical Alignment and Microscope Development
- Sample Preparation
- ODMR Development

6.2 Optical Alignment and Microscope Development

Throughout this research project I have been responsible for the alignment of the bespoke confocal microscope system. I have, at one point or another, aligned every optical component that makes up the confocal microscope system. In addition to alignment, I have also been involved in the calibration and installation of a number of components within the microscope system. I will briefly discuss my contributions to the calibration and installation of the deformable mirror in the following subsection:

6.2.1 Deformable Mirror

The key point of difference between our ODMR measurement system and those that have been previously reported is that we have included a deformable mirror (DM) in our optical setup. The addition of the DM in our system allows for the systematic removal of sample induced aberrations to improve the signal to noise ratio of our experiments and improve the quality of our confocal images [2, 49]. I have detailed the installation and calibration of our deformable mirror in this work. I have also outlined the procedure used for sensorless aberration correction which we make use of within the research group. Finally, I have included an example of how the DM has been used to improve the point-spread function (PSF) of the microscope following the installation of the mirror and realignment of the microscope, removing a significant amount of coma from a direct PSF measurement.

6.3 Sample Preparation

One of the challenges of this project has been to develop a methodology that would allow me to reliably prepare our samples for ODMR measurement and confocal imaging simultaneously. While preparing to perform experiments on the double split ring resonators (DSRR) [87], I needed to develop an adaptor that would allow me to securely mount the sample within the sample chamber. I used CAD software to design a mounting plinth for the DSRR and later redesigned for the coplanar waveguides. The DSRR and coplanar waveguides were fixed to the mounting plinths using super-glue. This combination proved stable enough for all ODMR measurements presented in this work, including the 12 minute ODMR scan in which only 9% of fluorescence intensity was lost.

I also was able to create a protocol for sample preparation for confocal imaging and ODMR, and is outlined in 3.4.2. In preparing the samples using this method, I was able to reuse the coplanar waveguides for multiple experiments, which helped to reduce cost and waste throughout the project.

6.4 ODMR Development

The primary focus of this research project has been the development of an ODMR protocol that would allow us to perform magnetic field and temperature sensing measurements using nanodiamond probes within a live-cell environment. I will split the conclusion of the work performed on the development of the ODMR protocol into the following three subsections:

- Microwave delivery.
- Development of ODMR protocols
- Biological sensing

6.4.1 Microwave Delivery

The initial development of the ODMR protocol was performed using the double-split ring resonator (DSRR) [87]. Using this resonator design, we were able to observe the ODMR spectra from NV^- ensemble inside a 90 nm diamond sample. From this initial measurement, I identified a series of improvements that could be made to the measurement protocol that would make the data recorded more reliable and the data easier to analyse. These were quickly implemented, allowing me to assess the performance of the DSRRs for using in our experimental setup. Initial experiments revealed that in the central region of the DSRR, the ODMR contrast was lower than 1%, even with maximum microwave power supplied to the system. To achieve a contrast greater than 1%, I needed to explore the sample beyond the area that could be observed using the wide-field camera when back-lighting the sample. This result presented an immediate problem for the use of the DSRR in our system. Firstly, the major driving factor for the use of the DSRR was the large area uniform microwave field produced in the centre of the resonators [87]. We needed to move outside of this area in order to achieve a suitable ODMR contrast for biological sensing measurements. Secondly, by moving outside the central region of the resonator, we moved away from the area of the sample that could be viewed when back-lit. The relatively poor ODMR contrast that we observed during these measurement (relative to those results produce by Bayat *et al* [87]), was thought to be the result of the oil immersion objective, required for high-resolution biological imaging, grounding the microwave signal produced by the resonator. In the end, it was decided that in order to progress with the project, we would need to find an alternative method of microwave delivery for these experiments.

From this point, I implemented the coplanar waveguides with a micro-wire antenna, used throughout this work and presented in section 3.4. In the charac-

terisation of these waveguides I was able to show that the coplanar waveguides were consistently able to produce a higher ODMR contrast than observed using the DSRR. Through the design of the coplanar waveguides and the characteristically small-area microwave field produced by the micro-wire antenna, I was able to ensure that the all nanodiamonds used for ODMR were within the field-of-view of the wide-field imaging arm when the sample was back-lit. The introduction of the coplanar waveguide solved two of the major problems I observed encountered when using the DSRRs.

6.4.2 Development of ODMR Protocols

Once the coplanar waveguide had been shown to be an effective method of microwave delivery in our microscope system, I was able to investigate the factors that can affect the quality of an ODMR measurement, as reported in section 3.5. Two of the key experimental parameters that play an important role in the sensitivity of a nanodiamond probe used for NV^- metrology are the applied microwave power and the excitation laser power. I have shown in this work that, as the microwave power is increased, the ODMR contrast (C) also increases towards an asymptotic maximum value, which is consistent with what is reported in literature [28]. With the increase in measurement contrast, I also found evidence of power broadening of the ODMR dips as a result of the increase in microwave power [120]. Using equation 3.9, I was able to show how the increase in the applied microwave power affected the DC magnetic sensitivity of the NV^- ensemble. The results showed that the maximum sensitivity not when the largest microwave power was applied, but when the following fraction $\frac{\Delta F}{C}$ was minimised (ΔF is the FWHM of the ODMR curve). In the case of the laser power, I found that as the laser power was increased, the ODMR contrast dropped. This result had also been reported in literature for nanodiamond probes, and is attributed to the reduction in spin-state transitions from the applied microwave field due

to the increased optical cycling of the NV^- centre as a result of increased laser power [122, 123]. This was an interesting result and presents a challenge when optimising ODMR performance, as the sensitivity of the probe is linearly dependent on the product of the square-root of the counts recorded ($\sqrt{N}$) and the ODMR contrast. Additionally, as this is an all optical measurement, the associated fractional measurement error is proportional to ($\frac{1}{\sqrt{N}}$). So the applied laser power needs to be finely balanced to maximise measurement contrast and minimise measurement error. From the measurements performed in this study, it appears that the larger nanodiamond samples I had available. with the NV^- concentrations above 100 defects per crystal would produce the highest measurement sensitivity, due to the increased number of fluorescent emitters within the crystal.

Following the discovery of the electromagnetic noise within the infrastructure of the building housing our microscope, and the sample drift attributed to the Oko-Labs temperature stage, it was decided that we needed to adapt our ODMR protocols to try and combat the effects of sample drift in our system. This was achieved by introducing the ODMR with Referencing measurement scheme, in which a reference measurement of the photon-flux from the nanodiamond probe was recorded for each applied ODMR microwave frequency. Normalising the ODMR data to the referenced data results in the removal of any impact in measurement drift on the produced ODMR spectra, allowing for accurate determination of the resonant frequency of the spin-state transitions. Some groups do perform ODMR with referencing without the use of a second microwave generator [42]. We found, however, that the inclusion of a second microwave generator helped to mitigate the effects of thermal drift as the reference measurement was applied.

To increase the speed of the ODMR measurement, I trialed the four-point

ODMR measurement scheme that was initially developed for temperature sensing [35, 1]. Following successful preliminary tests of the multi-point ODMR measurement scheme, I developed the simulated temperature sensing protocol. I used the results of a simulated temperature sensing experiment to test the performance of three different NV^- sensing analysis methods [35, 4, 1]. Of the three methods used, all were able to recover the magnitude of the applied simulated temperature change to within 5%. The method presented by Kucsko *et al* in [35] gave the highest error of the three analysis techniques (equivalent to roughly 7 K). The error attributed to the methods presented by Singam *et al* [4] and Fujiwara *et al* [1] were similar, both allowing for minimum temperature resolution of within 1.5 K. In these measurements largest contribution to the measurement error was found to be the photon flux used in our measurement compared to the results published in literature.

Throughout the development of the ODMR protocols, I have worked towards the aim of implementing the measurement scheme for biological sensing. The introduction of the ODMR with Referencing was significant, as it allows us to remove the effects of drift when trying to identify the resonant frequency of the NV^- centre. This will be of use to us when trying to record ODMR measurements from nanodiamonds inside live-cells, as there is likely to be more nanodiamond movement away from the focal spot of the confocal system [1]. To reduce the overall measurement time for temperature sensing, we have introduced a four-point ODMR measurement protocol. The aspiration for the multi-point measurement protocols is to allow us to sample the real-time temperature changes within a live-cell as external stimuli are applied. From the results of the above study, we are limited to time scales of over 100 s using the 70 nm nanodiamonds. It is possible we may be able to improve measurement accuracy using a nanodiamond sample with a larger total number of NV^- centres within the crystal.

6.4.3 Biological Sensing

I was able to test the biological sensing protocols that I have developed throughout this project on nanodiamonds embedded within immune cells, thanks to our collaboration with the Centre for Inflammation Research at the University of Edinburgh. Initially I showed that we were able to resolve 90 nm nanodiamonds within a macrophage cell using our confocal imaging system. I was also able to perform ODMR measurements on a selected nanodiamond within a macrophage. Not only was I able to determine the resonant microwave frequency for spin-state transitions of the NV^- centre, I was also able to recover the strength of an applied external magnetic field. This was a significant result, it showed that we were able to recover the strength of an applied magnetic field from a nanodiamond embedded within a cell body. It is not therefore, a significant leap in logic to suggest that we would be able to detect a magnetic field produced by a cell labelled using nanodiamonds using the experimental protocols developed here, however it is likely we are not yet at a regime of sufficient sensitivity to directly measure these fields.

The most important result throughout the whole of the research project was that of the simulate temperature sensing measurements performed on a nanodiamond within a THP1 cell. Primarily, the results were exciting because it showed that we were able to observe the effects of the simulated temperature changes from a nanodiamond embedded within a cell using the NV^- centre as an all optical temperature probe. The more significant result, however, was the discovery that the shape of the ODMR curve changed over the course of the course of the measurement, with the FWHM increasing and the ODMR contrast decreasing. It is not known at the time of writing what has caused this to occur, it is the suspicion of the author it is the result of the formation of, or change to a protein carona on the surface of the nanodiamond under illumination from the excitation

laser [151]. With this result, we were able to determine that the temperature sensing analysis technique presented by Fujiwara *et al* is the most suitable for our experimental setup [1]. The logic behind this assertion is first of all that the measurement scheme produced a significantly lower error when used to compare the same dataset as the method presented by Kucsko *et al* [35]. The analysis scheme presented by Singam *et al* on the other hand, requires a stable ODMR spectra from the nanodiamond across the measurement in order to accurately track temperature changes [4]. As a result, in a system in which the shape of the ODMR spectra might change, the Singam technique for temperature measurement is not suitable. The Fujiwara *et al* analysis method is only dependent on the ODMR spectra remaining symmetrical, but not on the actual shape of the ODMR curve itself, so long as the four applied microwave frequencies remain within the linear bounded region of the ODMR spectra. This gives us a direct avenue for development as the project progresses in the future.

Chapter 7

Future Work

7.1 Temperature Sensing

In the previous sections I have discussed the calibration of nanodiamond thermometers using simulated temperature sensing techniques using the four-point ODMR with Referencing measurement technique (section 4.4). Prior to the development of the simulated temperature sensing experiments, I was also able to perform preliminary calibration measurements using the Oko-Labs temperature stage (section 3.6). If more time were available, the natural progression of this project would be to try and calibrate the NV ensemble sensors against a known temperature shift while using the Oko-Labs 301-H temperature stage. Given another 3-6 months, I believe it would be possible to have sufficiently developed the sample preparation techniques to ensure minimal nanodiamond agglomeration [127], and to compensate for the magnetic field associated with the temperature stage 3.6. The combination of these two improvements to the experimental procedure would allow for single NDs or small ND clusters to be calibrated for use as temperature probes. This would allow us to test, for ourselves, if the size of commercially available nanodiamonds affects the sensitivity of the NV^- resonant frequency to temperature. At present, the temperature sensitivity of the NV^-

centre is thought to be the result, at least in part, to the thermal expansion of the diamond lattice [153]. The internal crystallographic strain within nanodiamonds is larger than that observed in bulk diamonds as a result of the greater percentage of atoms at the surface of the crystal [154]. The inhomogeneity of the strain through the nanodiamond crystals has been reported to have been reduced via thermal annealing, which would reduce the effects of inhomogeneous broadening of the NV^- ensembles as the temperature applied increased [155]. The manufacturers of the nano-crystals I have used throughout this project would not reveal anything about their manufacturing processes, and thus leaves the question open as to how the different sizes of nanodiamond, and potentially between batches of the same size nanodiamond, would respond when exposed to the same temperature sensing calibration measurements. At the time of writing, I have not seen anything in the literature in which the temperature sensitivity of a variety of ND sizes has been compared using the same experimental set-up. In previous works, it appears that the value of -74 kHz K^{-1} observed by Acosta *et al* in bulk diamond [37] has been observed in nanodiamond crystals of a similar size to those I have been using in this thesis [35]. This temperature dependency has been shown in nanodiamonds as small as 5 nm, however, these crystals were specially treated and annealed before temperature sensing measurements were preformed [102].

There are several considerations that need to be made when preparing for temperature sensing experiments:

- **The cyclical stage drift:** As shown previously in section 3.6, the temperature stage causes a cyclical axial drift of the sample. The amplitude of oscillation observed in the fluorescence detection was up to a 10% of the mean fluorescent signal observed. The cyclic sample drift should be well compensated for using the ODMR with Referencing measurement protocol. The axial drift of the sample can be minimised over the course of the

measurement using the four-point temperature sensing techniques explored in section 4.3.1, due to reduced measurement times. This would allow for temperature sensing calibrations to be performed before the sample drift degrades the quality of the measurement to the point where the ODMR signal is indistinguishable from the random measurement noise.

- **Magnetic field from the stage:** The Oko-Labs temperature stage has a magnetic field that has been shown to affect the ODMR measurements in our system (section 3.6). It has been proposed that the addition of a magnetic field can increase the sensitivity of a temperature sensing measurement [133]. The disadvantage of the magnetic field from the Oko-Labs stage can't be optimised for the orientations of the nanodiamonds used for the measurement. The addition of a secondary magnetic field, with a controllable orientation, could help to optimise the performance of the NV^- thermometry by aligning the magnetic field to the crystallographic axis of the defect. The addition of the nebuliser reported in [127] would also help to reduce agglomeration of NDs in the sample under study. This should help in the ODMR measurements in the presence of a magnetic field as the different orientation of the NV^- ensembles in the randomly orientated ND cluster can make observing the B-field split ODMR dips more complicated.

- **Relative brightness of ND sizes:** As discussed, the different sizes of nanodiamonds have differing quantities of NV^- centres present in their crystals, ranging from $1\,NV^-$ to $500\,NV^-$ centres. The differing number of NV centres in the ND sizes presents an interesting problem for experimental planning and analysis. As more NV^- centres exist in the larger ND crystals, for the same applied laser power, they will produce a higher fluorescence intensity than the smaller NDs. The larger NV^- ensembles are expected to have a greater amount of spin-mixing as a result of the number of defects

within the diamond structure, and as a result, will have a larger inherent FWHM ODMR dip. To perform a direct comparison between the sensitivity of the different sizes of nanodiamonds, one will need to either keep the photon flux from the ND cluster comparable, or ensure the applied laser power and photon integration times are consistent across all thermometry measurements.

- **Laser power dependency of the ODMR contrast:** As shown in section 3.5.3, the laser power applied to the nanodiamond impacts the ODMR contrast observed in the ODMR measurements. This has implications for the above bullet point, as it may be that in order to maximise the sensitivity of different size ND sensors, different laser power and dwell times are needed. This is further complicated by the results of 2.7, which suggests that simply increasing the dwell time of photon integration may introduce the effects of lower frequency noise into our measurement system, which further degrades the sensitivity of the ODMR measurements.

The value of the above experiments is that it would allow for the direct comparison of a number of different sizes of nanodiamond for thermometry. It also opens up the possibility of comparing how the number of NV^- centres present within a nanodiamond affects the temperature sensitivity, independent of sample size. Several groups, such as that of Dr. Williams in Cardiff are capable of fabricating nanodiamonds [127]. By fabricating a number of nanodiamonds of the same size, but differing NV^- concentration, then one could test the theoretical model that the sensitivity of the NV^- thermometer does increase proportionally to the square-root of the number of NV^- centres present [1]. I have highlighted a number of difficulties associated with using the Oko-Labs temperature stage, there are other products on the market, such as the VAHEAT system from interherence (https://interherence.com/vaheat/), which present an interesting

alternative to the traditional environment chamber for temperature sensitive measurements.

7.1.1 Live-Cell Thermometry

Once the calibration of the ND sensors has been completed, the natural evolution of this experiment would be to monitor temperature changes that occur inside first fixed cells and then live-cell samples. The group has recently gained access to a bio-lab and are focusing on growing *C.elegans*, a transparent worm that has been used for NV^- thermometry experiments previously [1]. This provides a base-line by which to compare any live-cell temperature measurements that we might perform. The transition to live-cell temperature sensing will come with a series of additional challenges, such as:

- **Sample drift:** Live cell systems have the ability to move. This presents a challenge in terms of keeping the nanodiamond sensor in the focus of the confocal microscope. McGuinness *et al* have reported performing ODMR on nanodiamonds while tracking them in three dimensional space [156]. It is possible that a similar tracking regime could be incorporated for use in our system to track the nanodiamond as it diffuses through a cell body.

- **Cell labelling:** The most interesting results for an intra-cellular thermometry is to localise heating to specific organelles or points of interest within the cell. In order to do this effectively and efficiently, the nanodiamonds need to be functionalised to label structures within the cell would be of interest. We do not currently have this expertise in the research group, and thus would need to look at forming collaborations with groups such as Dr. Jayasinghe's that have started work on immuno-labelling with nanodiamond [30].

- **Probe calibration:** Working with live-cell samples will rarely give one the

opportunity to perform a full calibration of the nanodiamond sensor before performing temperature sensing measurements. Experiments such as those performed by Nishimura *et al* have shown that there is some variation between the behaviour of NV^- ensemble sensors, even when within the same environment [157]. As a result, one is reliant on having either a good calibration of the temperature response of the NV^- ensembles within the nanodiamond size selected, and/or perform an average temperature sensing measurement from several nanodiamonds close to the area of interest for direct comparison. The simulated temperature sensing measurements may help to provide a baseline for the responsiveness of a nanodiamond probe to shifts in temperature by revealing the smallest shift in temperature that can be observed given the photon-flux, ODMR contrast and line-width.

7.2 ODMR in Other Optical Systems

Recently there have been examples of ODMR measurements being performed using wide-field measurement systems [158, 157, 130]. A wide-field sensing technique for ODMR offers an advantage over the confocal system in that it allows one to monitor the temperature or magnetic field gradient across a sample from a single measurement [130]. The ODMR measurement regimes used here all discuss using a similar ODMR with Referencing protocol to the one that I have outlined in this work [158, 157, 130]. With the knowledge that the ODMR protocol that I have implemented is compatible with wide-field systems, an interesting future experiment would be to test the ODMR protocol on a number of different optical set-ups. This work is already starting within the group, with early results coming from measurements using: a wide-field fluorescence microscope, a TIRF system and an adaptive-optics enhanced fluorescent light-sheet microscope. Using these systems it will be possible to investigate the temperature gradient across, or mag-

netic field generated by live-cell organisms with nanodiamonds integrated into the cell body. One of the additional benefits of using a wide-field fluorescence measurement system is that it is less sensitive to axial sample drift than a confocal system [157]. This is a result of the lack of optical sectioning in wide-field microscope systems [54]. Sample stability is therefore less of an issue when performing wide-field ODMR, and means that the movement of a live-cell within the field-of-view will not necessarily prohibit magnetic field or temperature sensing within the sample [158].

Analysis of the wide-field experiments does come with challenges that are not present when performing ODMR using a confocal system. The most obvious of these problems is the selection of the region with which to perform the ODMR analysis [158]. In confocal ODMR, a point-like object is held within the focus of the microscope, only the fluorescence intensity from this point in the sample can be used for ODMR. This makes analysis relatively simple, as one only needs to consider the fluorescence intensity recorded as a function of the microwave frequency [89]. The effects of moderate sample drift in a confocal ODMR measurement can be mitigated for via the Referencing scheme outlined in section 3.7. When performing ODMR using a wide-field system and a nanodiamond sample, it is very unlikely that one will be investigating a single nanodiamond within the field of view. As a result, regions of interest need to be determined in order to glean the ODMR information from a measurement [159]. The difficulty lies then in where one draws the boundary for such a measurement. It is often the case that the nanodiamonds will agglomerate during sample preparation [127]. These clusters need to be treated as a single fluorescent entity in the analysis as it is not possible to isolate single diamonds within the structure. This in turn can affect the sensitivity of the ODMR measurements, especially when strain effects are known to be non-uniform across nanodiamonds from the same batch [92].

7.3 AC Magnetometry

One of the target applications of the technology and analysis that I have developed throughout this project has been to monitor the magnetic field generated when a neuron fires [160]. Such experiments have already been explored using diamond sensors [34, 158]. The aim of our experiments would be to label the surface of a neuron using functionalised nanodiamond. We could then use our confocal ODMR system monitor the magnetic field generated by the cell as it fires [158]. The higher spatial resolution available from the confocal system will allow for a more detailed analysis of the strength of the magnetic field generated across the different regions of the neuron.

In the experiments outlined in this work, we have only ever been able to monitor DC magnetic fields (section: 3.6). In order to be able to monitor the magnetic field generated by a neuron, we would need to implement an AC magnetometry measurement protocol [34]. In current magnetoencephalography methods, such as super-conducting quantum interference devices (SQUIDS) or atomic vapour cells, the sampling frequency used is between 1 kHz - 2 kHz [161]. In order to accurately monitor the magnetic fields generated by neurons, we would need to ensure similar sampling rates in our system. Using the current experimental protocol, using a 1 MHz frequency step, a photon integration time of 1 ms and a frequency sweep from 2.84 GHz - 2.90 GHz would result in a single line scan sampling frequency of 16.6 Hz. If we include the referencing measurements in this protocol then the sampling frequency drops by half. In a paper presented by Kuwahata *et al*, the authors outline a method of AC magnetometry using the NV centre that is based on lock-in amplification [162]. The measurement scheme works by first recording a ODMR spectra from the NV^- centre(s) with a bias magnetic field applied to the sample. Using the lowest frequency component of the Zeeman split spec-

tra, the point of maximum gradient on the ODMR dip is identified and used for the AC magnetometry measurements [162]. Using a home-built electromagnet, a low amplitude AC magnetic field was applied to the diamond sample, and using lock-in measurement technique, the frequency and strength of the applied field could be determined [162]. The use of lock-in amplification is popular within the diamond community for AC magnetometry experiments [163, 164, 165], as it allows for low amplitude signals to be observed even in measurement regimes where the noise is significantly larger than the signal of interest [163]. The application of a lock-in amplifier in our system, in which frequency modulation is applied to a single frequency point within the ODMR spectra would allow us to monitor the application of the small magnetic field associated with neuron firing [161].

I would recommend before an attempt is made at measuring the magnetic field generated by a live-cell a series of preliminary and proof of principle measurements are made. In the first instance, we would need to implement a lock-in amplification measurement system that would allow us to monitor low-amplitude AC magnetic fields. I would suggest following in the footsteps of Kuwahata *et al* and implementing a home-built electromagnet positioned close to the sample stage [162]. A full assessment of the stability of the microscope then needs to be conducted with the electromagnet in place. As shown in section 3.5.2, the peizo-electric controller for the objective stage is sensitive to AC magnetic fields generated within the building. We would need to ensure that generating an electromagnet so close to the objective does not affect the stability of the ODMR measurement. The second consideration is that the fast steering mirror and the resonant scanner are also controlled by electromagnets, and so calibration measurements would be needed to ensure that the stability of the laser-spot for imaging is not affected. Assuming that the stability of the microscope is not affected by the electromagnet, one can then set about implementing an AC mag-

netometry protocol such as that described in [162] to measure the strength and frequency of an alternating magnetic field.

Once calibration measurements have been made and the ability to measure the strength of a controlled magnetic field has been applied, then one could move onto measuring the magnetic field generated by a live-neuron. Barry *et al* reported detecting magnetic fields generated by a single firing axon in the range of 100's of pico-Tesla [34]. In this work the researchers are also using a lock-in amplification technique for detection, but were using a bulk-diamond crystal and a TIRF style excitation of the NV centres within the diamond. This gave the researchers access to a large number of NV^- centres to perform the sensing measurements, increasing the sensitivity relative to a single NV centre by $\sqrt{N}$. Another interesting observation of this work is that the researchers required many repeat firings from the neuron in order to achieve this level of magnetic sensitivity [34]. The work by Barry *et al* provides a solid foundation to build upon in the development of a NV^- based magnetometer for biological sensing. It is intended, as we have the ability to perform multi-colour imaging in our microscope, to use this measurement technique alongside complementary technology. Proteins, such as GCamp, have been used to track the image neuronal firing, as the protein is fluorescent when the concentration of calcium ions increases within the cell. The calcium ion transport and concentration are a key component for neuronal firing and are a good indication of neuronal activity [45].

7.4 STED Microscopy

One of the upgrades to the microscope that has yet to be implemented is the incorporation of the depletion arm to allow for stimulated emission depletion (STED) microscopy to be performed. This is a super-resolution imaging technique

that has been well described previously [166, 167, 168] and has shown to work well with nanodiamond probes [169].

The principle of STED microscopy is that two lasers are used during imaging. The first is an excitation laser used to raise the energy level of the fluorescence probe used for imaging. The second is the depletion laser. The depletion beam has a phase mask applied to it (in our system from an SLM) which creates a region of zero intensity in the centre of beam focal spot [49]. By co-aligning these two beams and timing the pulse sequence correctly, the depletion beam can be used to excite stimulated emission from the region of the sample in which both lasers are incident on the sample [170]. This leaves the region of the sample that is excited only by the excitation beam to emit via spontaneous emission and therefore have a different emission wavelength to the region of the sample emitting via stimulated emission [166]. By using a series of optical filters when recording the fluorescence from the sample, one can remove the stimulated emission leaving only emission from the minima of the depletion beam profile, with the limit of resolution (Δx) being dependant on the following equation [167]:

$$\Delta x = \frac{\lambda}{2NA\sqrt{(1 + \frac{I}{I_{sat}})}} \tag{7.1}$$

In which, λ is the wavelength of the excitation laser, NA is the numerical aperture of the objective, I is the applied depletion beam power and I_{sat} is the saturation power for the fluorophore under study, denoting when the laser power is so large that the probability of spontaneous emission is reduced to 0.5 [167].

The addition of STED capability to our microscope system would allow us to record non-computational super-resolution images of biological material to help further biomedical research [168]. Due to their photostability and broad emission spectra, fluorescent nanodiamonds make an ideal probe for STED microscopy, as

the limits of image resolution are proportional to the square root of the applied depletion beam laser power [171]. For any fluorophores which experience bleaching STED microscopy becomes a difficult imaging technique to utilise as the laser power involved from both the excitation and depletion beams can rapidly result in bleaching [167].

One of the most interesting experiments that we would perform once the microscope has been upgraded would be to see if STED imaging results in sample heating. In the case of our experimental set-up, the depletion laser used for STED imaging is 775 nm laser at the far-red section of the visible spectra. During STED imaging, the intensity at the focus of the microscopy can be as high as GW/cm^2 [167]. It is difficult to see how having this much laser power passing into a sample would not result in heating. Using the temperature sensing protocols that have been discussed in depth within this thesis, one could utilise the NV^- centre to monitor any temperature changes that arise as a result of STED imaging. In such an experiment, a base-line measurement should be recorded before the depletion beam is applied. Following this, the depletion beam can be applied with temperature measurements being made as the depletion beam power is increased incrementally. The results of this measurement could be coupled with 3D scans of the nanodiamond used for study to give a measurement of the practical resolution limit for and applied depletion power as well as the increase in temperature. As the thermal conductivity of diamond is so high [48], there should not be a requirement to wait for thermal equilibrium to set in as the laser power is increased.

A consideration when making these experiments is that the increase in the applied power supplied to a nanodiamond under study by the depletion beam may result in the ODMR contrast being completely lost, in which case it would not be possible to measure any increase in temperature during STED microscopy [123].

The adaptive optics enhanced microscope described here has three excitation lasers. It would be fairly trivial to test if the addition of a secondary laser light source on the sample with a power of the order of mW affects the ODMR contrast from a nanodiamond sample. This would be a good test of feasibility before a significant amount of time and effort is put into attempting to measure the sample heating effects of STED microscopy.

Appendix A

Sample Preparation

Throughout this research project I have been using commercially available nanodiamond colloidal mixtures for the measurements described in this work. In the following two appendices, I will describe:

1. The process of dilution used to reduce the concentration of nanodiamond in the mixture. This reduced the amount of diamond material used in each experiment and made it significantly easier to identify single or small clusters of nanodiamond when imaging.

2. The process of sample preparation used to prepare a coplanar waveguide for imaging and ODMR experiments.

A.1 Colloidal Dilutions

1. Firstly, the dilution ratio of the dense, store-brought, colloidal mixture and the distilled water was calculated. For this work, we typically used ratios of 1:20, 1:50 or 1:100 ND colliodal:water.

2. The size of the diamonds wanted in the colloidal dilution is selected and the appropriate vial of dense nanodiamond colloidal is placed in a water-bath

sonicator and left to mix for 15 minutes.

3. After sonication, the dense colloidal was removed from the water bath and, using a pipette, the required quantity of the dense ND mixture was removed from the vial and placed into a 1.5 mL cuvette. This was then mixed with the quantity of distilled water required to make the desired dilution ratio.

4. The diluted ND colloidal sealed in the cuvette and placed back into the water-bath sonicator for a further hour. This was to ensure good mixing of the nanodiamonds within the dilution and to limit the agglomeration between nanoparticles.

5. The diluted sample was then kept within the cuvette in the samples fridge within the sample-preparation laboratory. When a dilution was required for use, it would be sonicated for at least 15 minutes before use, to again ensure good sample mixing and break up any nanoparticle aggregates that may have occurred while the sample was not in use.

A.2 ODMR Sample Preparation

1. To prepare the waveguides for use, the SMA adpators needed to be soldered onto the PCB board, with the central pin placed on the conductive channel pad on the waveguide, and the two ground pins on the pad either side of the central channel. It is noted here that the SMA adaptors were only soldered to the top (patterned) side of the PCB and not underneath.

2. With the PCB prepared for microwave conduction, a 20 mm $\times$ 20 mm glass coverslip was secured to the surface of the coplanar waveguides by small amounts of nail-varnish applied to the corners of the coverslip, this was then left to dry. The coverslip was positioned in the centre of the coplanar

waveguide, with the centre of the coverslip over the hole in the waveguide used for back-lighting the sample. This coverslip will be known as the "base-plate coverslip" from here onwards.

3. The 40 µm copper wire was then secured to the coplanar waveguide using silver paint (this was found to have good conduction of microwave power through the copper wire) allowing for waveguides to be re-used. Soldering the wire in place would have meant a new coplanar waveguide would have been required for each new experiment. The copper wire was pulled tight across the surface of the base-plate coverslip. The copper wire was secured in position along the conducting portion of the waveguide using tape until the silver paint applied had dried. The silver paint was applied directly to the dielectric coating on the PCB. There was not any loss in microwave power associated with applying the sliver paint to the dielectric, rather than the copper of the conduction plate underneath.

4. A glass coverslip of 18 mm in diameter was used for nanodiamond drop-casting. The diluted nanodiamond mixture of choice is selected and, using a pipette, 10 µm-20 µm of the dilution is applied to the surface of the coverslip. The coverslip is then heated on a hot-plate at 50°C until the diamond colloidal has completely evaporated.

5. With the nanodiamonds now drop cast onto the surface of the glass coverslip, the immersion media is added to the nanodiamond coated surface of the 18 mm diameter coverslip. The immersion media used in this work was most often either: A single drop of distilled water, a single drop of immersion oil (refractive index = 1.35) or a single drop of prolong diamond.

6. The diamond coated coverslip would then be placed on top of the base-plate coverslip, immersion media side down. Upon contact with the base-

plate coverslip, the immersion media will naturally spread between the two coverslips and cover the total area of the diamond coated coverslip. If using prolong diamond, the sample is then left for 24 hours in the dark so that the prolong can set properly.

7. The nanodiamond coated coverslip is then fixed to the surface of the base-plate coverslip using a small amount of epoxy resin glue. The resin was applied using a cocktail stick. This allowed for good control of the application of the resin of a small amount of resin around the edge of the 18 mm coverslip. The sample was then left to dry before use in the confocal microscope system.

8. We found it useful to check the quality of a sample using a low-cost wide-field bright-field/fluorescence microscope. This allowed us to check for any air-bubbles in the immersion media around the copper wire and to check we were able to see nanodiamond fluorescence in close proximity to the wire as well.

Bibliography

[1] M Fujiwara, S Sun, A Dohms, Y Nishimura, K Suto, Y Takezawa, K Oshimi, L Zhao, N Sadzak, Y Umehara, Y Teki, N Komatsu, O Benson, Y Shikano, and E Kage-Nakadai. Real-time nanodiamond thermometry probing in vivo thermogenic responses. *Science Advances*, 6(37), 2020.

[2] M. J. Booth, M. A. A. Neil, R. Juskaitis, and T. Wilson. Adaptive aberration correction in a confocal microscope. *Proceedings of the National Academy of Sciences*, 99(9):5788–5792, April 2002.

[3] D. Burke, B. Patton, F. Huang, J. Bewersdorf, and M. J. Booth. Adaptive optics correction of specimen-induced aberrations in single-molecule switching microscopy. *Optica*, 2(2):177–185, Feb 2015.

[4] S. K. R. Singam, M Nesladek, and E Goovaerts. Nitrogen-vacancy nanodiamond based local thermometry using frequency-jump modulation. *Nanotechnology*, 31(10):105501, March 2020.

[5] C. J. R. Sheppard. The development of microscopy for super-resolution: Confocal microscopy, and image scanning microscopy. *Applied Sciences*, 11(19), 2021.

[6] R. Hooke. *Micrographia: Or, Some Physiological Descriptions of Minute Bodies Made by Magnifying Glasses. With Observations and Inquiries*

Thereupon. Early English Books Online / EEBO. J. Allestry, printer to the Royal Society, 1667.

[7] S.J. Wright and D. J. Wright. Chapter 1 - introduction to confocal microscopy. In Brian Matsumoto, editor, *Cell Biological Applications of Confocal Microscopy*, volume 70 of *Methods in Cell Biology*, pages 1–85. Academic Press, 2002.

[8] Amicia D. Elliott. Confocal Microscopy: Principles and Modern Practices. *Current Protocols in Cytometry*, 92(1), March 2020.

[9] M Papa, Mc Bundman, V Greenberger, and M Segal. Morphological analysis of dendritic spine development in primary cultures of hippocampal neurons. *J. Neurosci.*, 15(1):1–11, January 1995.

[10] J Vangindertael, R Camacho, W Sempels, H Mizuno, P Dedecker, and K P F Janssen. An introduction to optical super-resolution microscopy for the adventurous biologist. *Methods Appl. Fluoresc.*, 6(2):022003, March 2018.

[11] S. Culley, K. L. Tosheva, P. Matos Pereira, and R. Henriques. SRRF: Universal live-cell super-resolution microscopy. *The International Journal of Biochemistry & Cell Biology*, 101:74–79, August 2018.

[12] H. Zhong. Photoactivated localization microscopy (palm): An optical technique for achieving 10-nm resolution. *Cold Spring Harbor protocols*, 2010:pdb.top91, 12 2010.

[13] J. Xu, H. Ma, and Y. Liu. Stochastic optical reconstruction microscopy (storm). *Current Protocols in Cytometry*, 81(1):12.46.1–12.46.27, 2017.

[14] S. W. Hell. Microscopy and its focal switch. *Nature Methods*, 6(1):24–32, Jan 2009.

[15] Bianmiao L., Qiaoling Y., and Yixiang D. Fluorescent labels in biosensors for pathogen detection. *Critical Reviews in Biotechnology*, 35(1):82–93, 2015.

[16] C. Cottet-Rousselle, X. Ronot, X. Leverve, and J-F. Mayol. Cytometric assessment of mitochondria using fluorescent probes. *Cytometry Part A*, 79A(6):405–425, 2011.

[17] L. Shang, F. Stockmar, N. Azadfar, and U. Nienhaus. Intracellular Thermometry by Using Fluorescent Gold Nanoclusters. *Angew. Chem. Int. Ed.*, 52(42):11154–11157, October 2013.

[18] R. M. Hoffman. Application of gfp imaging in cancer. *Laboratory Investigation*, 95(4):432–452, Apr 2015.

[19] N. Nath, B. Godat, and M. Urh. Antibody labeling with fluorescent dyes using magnetic protein a and protein g beads. *JoVE*, (115):e54545, Sep 2016.

[20] J. Schnitzbauer, M. T. Strauss, T. Schlichthaerle, F. Schueder, and R. Jungmann. Super-resolution microscopy with dna-paint. *Nature Protocols*, 12(6):1198–1228, Jun 2017.

[21] N. Shaner, M. Lin, M. McKeown, P. Steinbach, K. Hazelwood, M. Davidson, and R. Tsien. Evaluating and improving the photostability of fluorescent proteins. *Proc SPIE*, 7191, 02 2009.

[22] Ghauharali and Brakenhoff. Fluorescence photobleaching-based image standardization for fluorescence microscopy. *Journal of Microscopy*, 198(2):88–100, 2000.

[23] R. Alford, H. M. Simpson, J. Duberman, G. Craig Hill, M. Ogawa, C. Regino, H. Kobayashi, and P. L. Choyke. Toxicity of organic fluo-

rophores used in molecular imaging: Literature review. *Molecular Imaging*, 8(6):7290.2009.00031, 2009.

[24] A. M. Ansari, A. K. Ahmed, A. E. Matsangos, F. Lay, L. J. Born, G. Marti, J. W. Harmon, and Z. Sun. Cellular gfp toxicity and immunogenicity: Potential confounders in in vivo cell tracking experiments. *Stem Cell Reviews and Reports*, 12(5):553–559, Oct 2016.

[25] P. P. Laissue, R. A. Alghamdi, P. Tomancak, E. G. Reynaud, and H. Shroff. Assessing phototoxicity in live fluorescence imaging. *Nature Methods*, 14(7):657–661, Jul 2017.

[26] V. M. Runge and J. T. Heverhagen. *Imaging Basics: Signal-to-Noise Ratio*, pages 36–37. Springer International Publishing, Cham, 2022.

[27] W. W-W. Hsiao, Y. Y. Hui, P-C. Tsai, and H-C. Chang. Fluorescent nanodiamond: A versatile tool for long-term cell tracking, super-resolution imaging, and nanoscale temperature sensing. *Accounts of Chemical Research*, 49(3):400–407, Mar 2016.

[28] M. W. Doherty, F. Dolde, H. Fedder, F. Jelezko, J. Wrachtrup, N. B. Manson, and L. C. L. Hollenberg. Theory of the ground-state spin of the nv^- center in diamond. *Phys. Rev. B*, 85(20):205203, May 2012.

[29] P. Kehayias, M. W. Doherty, D. English, R. Fischer, A. Jarmola, K. Jensen, N. Leefer, P. Hemmer, N. B. Manson, and D. Budker. Infrared absorption band and vibronic structure of the nitrogen-vacancy center in diamond. *Phys. Rev. B*, 88:165202, Oct 2013.

[30] K. K. Narayanasamy, J. C. Price, R. Mesquita-Riberio, M. L. Mather, and I. Jayasinghe. Self-activated photoblinking of nitrogen vacancy centers in

nanodiamonds (sandstorm): A method for rapid single molecule localization microscopy with unlimited observation time. *bioRxiv*, 2020.

[31] A. Nagl, S. R. Hemelaar, and R. Schirhagl. Improving surface and defect center chemistry of fluorescent nanodiamonds for imaging purposes—a review. *Analytical and Bioanalytical Chemistry*, 407(25):7521–7536, Oct 2015.

[32] Amanda M. Schrand, Houjin Huang, Cataleya Carlson, John J. Schlager, Eiji Ōsawa, Saber M. Hussain, and Liming Dai. Are Diamond Nanoparticles Cytotoxic? *J. Phys. Chem. B*, 111(1):2–7, January 2007.

[33] D. Le Sage, K. Arai, D. R. Glenn, S. J. DeVience, L. M. Pham, L. Rahn-Lee, M. D. Lukin, A. Yacoby, A. Komeili, and R. L. Walsworth. Optical magnetic imaging of living cells. *Nature*, 496(7446):486–489, Apr 2013. 23619694[pmid].

[34] J. F. Barry, M. J. Turner, J. M. Schloss, D. R. Glenn, Y. Song, Mikhail D. Lukin, H. Park, and R. L. Walsworth. Optical magnetic detection of single-neuron action potentials using quantum defects in diamond. *Proc. Natl. Acad. Sci. U.S.A.*, 113(49):14133–14138, December 2016.

[35] G. Kucsko, P. C. Maurer, N. Y. Yao, M. Kubo, H. J. Noh, P. K. Lo, H. Park, and M. D. Lukin. Nanometre-scale thermometry in a living cell. *Nature*, 500(7460):54–58, August 2013.

[36] F. Jelezko, T. Gaebel, I. Popa, A. Gruber, and J. Wrachtrup. Observation of Coherent Oscillations in a Single Electron Spin. *Phys. Rev. Lett.*, 92(7):076401, February 2004.

[37] V. M. Acosta, E. Bauch, M. P. Ledbetter, A. Waxman, L.-S. Bouchard, and

D. Budker. Temperature Dependence of the Nitrogen-Vacancy Magnetic Resonance in Diamond. *Phys. Rev. Lett.*, 104(7):070801, February 2010.

[38] R. Körber, J-H. Storm, H. Seton, J. P. Mäkelä, R. Paetau, L. Parkkonen, C. Pfeiffer, B. Riaz, J. F. Schneiderman, H. Dong, S. Hwang, L. You, B. Inglis, J. Clarke, M. A. Espy, R. J. Ilmoniemi, P. E. Magnelind, A. N. Matlashov, J. O. Nieminen, P. L. Volegov, K. C. J. Zevenhoven, N. Höfner, M. Burghoff, K. Enpuku, S. Y. Yang, J-J. Chieh, J. Knuutila, P. Laine, and J. Nenonen. SQUIDs in biomagnetism: a roadmap towards improved healthcare. *Superconductor Science and Technology*, 29(11):113001, sep 2016.

[39] T. H. Sander, J. Preusser, R. Mhaskar, J. Kitching, L. Trahms, and S. Knappe. Magnetoencephalography with a chip-scale atomic magnetometer. *Biomedical optics express*, 3(5):981–990, May 2012. 22567591[pmid].

[40] C. O'Dwyer, S. J. Ingleby, I. C. Chalmers, P. F. Griffin, and E. Riis. A feed-forward measurement scheme for periodic noise suppression in atomic magnetometry. *Review of Scientific Instruments*, 91(4):045103, 2020.

[41] S. P. Singh. Magnetoencephalography: Basic principles. *Annals of Indian Academy of Neurology*, 17(Suppl 1):S107–S112, Mar 2014. 24791076[pmid].

[42] J. C. Price, R. Mesquita-Ribeiro, F. Dajas-Bailador, and M. L. Mather. Widefield, spatiotemporal mapping of spontaneous activity of mouse cultured neuronal networks using quantum diamond sensors. *Frontiers in Physics*, 8, 2020.

[43] J. M. Taylor, P. Cappellaro, L. Childress, L. Jiang, D. Budker, P. R. Hemmer, A. Yacoby, R. Walsworth, and M. D. Lukin. High-sensitivity diamond magnetometer with nanoscale resolution. *Nature Physics*, 4(10):810–816, Oct 2008.

[44] M Radtke, E Bernardi, A Slablab, R Nelz, and E Neu. Nanoscale sensing based on nitrogen vacancy centers in single crystal diamond and nanodiamonds: achievements and challenges. *Nano Futures*, 3(4):042004, December 2019.

[45] J. E. Hartung and M. S. Gold. Gcamp as an indirect measure of electrical activity in rat trigeminal ganglion neurons. *Cell Calcium*, 89:102225, 2020.

[46] K. Okabe, R. Sakaguchi, B. Shi, and S. Kiyonaka. Intracellular thermometry with fluorescent sensors for thermal biology. *Pflügers Archiv - European Journal of Physiology*, 470(5):717–731, May 2018.

[47] J-M. Yang, H. Yang, and L. Lin. Quantum Dot Nano Thermometers Reveal Heterogeneous Local Thermogenesis in Living Cells. *ACS Nano*, 5(6):5067–5071, June 2011.

[48] Y. Yamamoto, T. Imai, K. Tanabe, T. Tsuno, Y. Kumazawa, and N. Fujimori. The measurement of thermal properties of diamond. *Diamond and Related Materials*, 6(8):1057–1061, 1997.

[49] B. R. Patton, D. Burke, D. Owald, T. J. Gould, J. Bewersdorf, and M. J. Booth. Three-dimensional sted microscopy of aberrating tissue using dual adaptive optics. *Opt. Express*, 24(8):8862–8876, Apr 2016.

[50] J. Jonkman, C. M. Brown, G. D. Wright, K. I. Anderson, and A. J. North. Tutorial: guidance for quantitative confocal microscopy. *Nature Protocols*, 15(5):1585–1611, May 2020.

[51] N Aslam, G Waldherr, P Neumann, F Jelezko, and J Wrachtrup. Photo-induced ionization dynamics of the nitrogen vacancy defect in diamond investigated by single-shot charge state detection. *New J. Phys.*, 15(1):013064, January 2013.

[52] Ph Tamarat, N B Manson, J P Harrison, R L McMurtrie, A Nizovtsev, C Santori, R G Beausoleil, P Neumann, T Gaebel, F Jelezko, P Hemmer, and J Wrachtrup. Spin-flip and spin-conserving optical transitions of the nitrogen-vacancy centre in diamond. *New J. Phys.*, 10(4):045004, April 2008.

[53] K. Huebener, R. S. Schoenfeld, J. Kniepert, C. Oelmueller, and W. Harneit. Odmr of nv centers in nano-diamonds covered with n@c60. *physica status solidi (b)*, 245, 2008.

[54] M. Minsky. Memoir on inventing the confocal scanning microscope. *Scanning*, 10(4):128–138, 1988.

[55] T. WILSON. Resolution and optical sectioning in the confocal microscope. *Journal of Microscopy*, 244(2):113–121, 2011.

[56] C. Perego, S. Fumagalli, and M-G. De Simoni. Three-dimensional confocal analysis of microglia/macrophage markers of polarization in experimental brain injury. *Journal of visualized experiments : JoVE*, (79):50605, Sep 2013. 24056862[pmid].

[57] Y-W. Lim, H. P. Lo, T. E. Hall, and R. G. Parton. *Live Confocal Imaging of Zebrafish Notochord Cells Under Mechanical Stress In Vivo*, pages 175–187. Springer US, New York, NY, 2020.

[58] C. M. St. Croix, S. H. Shand, and S. C. Watkins. Confocal microscopy: comparisons, applications, and problems. *BioTechniques*, 39(6S):S2–S5, 2005. PMID: 20158500.

[59] S. Inoué. *Foundations of Confocal Scanned Imaging in Light Microscopy*, pages 1–19. Springer US, Boston, MA, 2006.

[60] E. H. K. Stelzer, F. Strobl, B-J. Chang, F. Preusser, S. Preibisch, K. McDole, and R. Fiolka. Light sheet fluorescence microscopy. *Nature Reviews Methods Primers*, 1(1):73, Nov 2021.

[61] J. Oreopoulos, R. Berman, and M. Browne. Chapter 9 - spinning-disk confocal microscopy: present technology and future trends. In Jennifer C. Waters and Torsten Wittman, editors, *Quantitative Imaging in Cell Biology*, volume 123 of *Methods in Cell Biology*, pages 153–175. Academic Press, 2014.

[62] J. Wiedenmann, F. Oswald, and G. U. Nienhaus. Fluorescent proteins for live cell imaging: Opportunities, limitations, and challenges. *IUBMB Life*, 61(11):1029–1042, 2009.

[63] C. Wang, A. Fukazawa, M. Taki, Y. Sato, T. Higashiyama, and S. Yamaguchi. A phosphole oxide based fluorescent dye with exceptional resistance to photobleaching: A practical tool for continuous imaging in sted microscopy. *Angewandte Chemie International Edition*, 54(50):15213–15217, 2015.

[64] J. Xu, Ho. Ma, and Y. Liu. Stochastic optical reconstruction microscopy (storm). *Current Protocols in Cytometry*, 81(1):12.46.1–12.46.27, 2017.

[65] E. Petryayeva, W. R. Algar, and I. L. Medintz. Quantum Dots in Bioanalysis: A Review of Applications across Various Platforms for Fluorescence Spectroscopy and Imaging. *Appl Spectrosc*, 67(3):215–252, March 2013.

[66] C. J. R. Sheppard and C. J. Cogswell. Effects of aberrating layers and tube length on con focal imaging properties. *Optik*, 87:34–38, 1991.

[67] Colin J. R. Sheppard and P. To¨ro¨k. Effects of specimen refractive index on confocal imaging. *Journal of Microscopy*, 185, 1997.

[68] S. F. Gibson and F. Lanni. Experimental test of an analytical model of aberration in an oil-immersion objective lens used in three-dimensional light microscopy. *J. Opt. Soc. Am. A*, 8(10):1601–1613, Oct 1991.

[69] K. M. Hampson, R. Turcotte, D. T. Miller, K. Kurokawa, J. R. Males, N. Ji, and M. J. Booth. Adaptive optics for high-resolution imaging. *Nat Rev Methods Primers*, 1(1):68, December 2021.

[70] M. Jemielita, M. J. Taormina, A. DeLaurier, C. B. Kimmel, and R. Parthasarathy. Comparing phototoxicity during the development of a zebrafish craniofacial bone using confocal and light sheet fluorescence microscopy techniques: Comparing light sheet and confocal derived phototoxicity in bone development. *J. Biophoton.*, 6(11-12):920–928, December 2013.

[71] M. J Booth. Adaptive optical microscopy: the ongoing quest for a perfect image. *Light Sci Appl*, 3(4):e165–e165, April 2014.

[72] R. Rodrigues de Mercado, H. van Hoorn, M. de Valois, C. Backendorf, J. Eckert, and T. Schmidt. Characterization of cell-induced astigmatism in high-resolution imaging. *Biomed. Opt. Express*, 13(1):464–473, Jan 2022.

[73] H. W. Babcock. The Possibility of Compensating Astronomical Seeing. *PASP*, 65:229, October 1953.

[74] J. W. Hardy, J. E. Lefebvre, and C. L. Koliopoulos. Real-time atmospheric compensation. *J. Opt. Soc. Am.*, 67(3):360–369, Mar 1977.

[75] M. J. Booth. Adaptive optics in microscopy. *Phil. Trans. R. Soc. A.*, 365(1861):2829–2843, December 2007.

[76] V. N. Mahajan. Zernike Circle Polynomials and Optical Aberrations of Systems with Circular Pupils. *Appl. Opt.*, 33(34):8121, December 1994.

[77] I. D. Varano. Characterization of Optical Aberrations Induced by Thermal Gradients and Vibrations via Zernike and Legendre Polynomials. *OPJ*, 06(06):113–123, 2016.

[78] V. Lakshminarayanan and A. Fleck. Zernike polynomials: a guide. *Journal of Modern Optics*, 58(7):545–561, 2011.

[79] B. Dong and M. J. Booth. Wavefront control in adaptive microscopy using shack-hartmann sensors with arbitrarily shaped pupils. *Opt. Express*, 26(2):1655–1669, Jan 2018.

[80] A. Thayil and M. Booth. Self calibration of sensorless adaptive optical microscopes. *Journal of the European Optical Society - Rapid publications*, 6(0), 2011.

[81] J. Antonello, J. Wang, C. He, M. Phillips, and M. Booth. *Interferometric calibration of a deformable mirror*, March 2020.

[82] ThePulsarBE. How to build an autocollimator. https://www.youtube.com/watch?v=5ZgB6Zj8Nzg&t=, 2017.

[83] P Thirupathi and S. Pagidipally. Strehl Ratio of Point Spread Function with First-Order Parabolic Filter. *International Journal of Engineering Research*, 3(3):3, 2014.

[84] L. C. Roberts Jr., M. D. Perrin, F. Marchis, A. Sivaramakrishnan, R. B. Makidon, J. C. Christou, B. A. Macintosh, L. A. Poyneer, M. A. van Dam, and M. Troy. Is that really your Strehl ratio? In Domenico Bonaccini Calia, Brent L. Ellerbroek, and Roberto Ragazzoni, editors, *Advancements in Adaptive Optics*, volume 5490, pages 504 – 515. International Society for Optics and Photonics, SPIE, 2004.

[85] J. A. Lane. The central limit theorem for the poisson shot-noise process. *Journal of Applied Probability*, 21(2):287–301, 1984.

[86] C. A. Casacio, L. S. Madsen, A. Terrasson, M. Waleed, K. Barnscheidt, B. Hage, M. A. Taylor, and W. P. Bowen. Quantum-enhanced nonlinear microscopy. *Nature*, 594(7862):201–206, Jun 2021.

[87] K. Bayat, J. Choy, M. Farrokh Baroughi, S. Meesala, and M. Loncar. Efficient, Uniform, and Large Area Microwave Magnetic Coupling to NV Centers in Diamond Using Double Split-Ring Resonators. *Nano Lett.*, 14(3):1208–1213, March 2014.

[88] G. Davies and M. F. Hamer. Optical Studies of the 1.945 eV Vibronic Band in Diamond. *Proceedings of the Royal Society A: Mathematical, Physical and Engineering Sciences*, 348(1653):285–298, February 1976.

[89] F Jelezko and J Wrachtrup. Read-out of single spins by optical spectroscopy. *Journal of Physics: Condensed Matter*, 16(30):R1089–R1104, jul 2004.

[90] L Rondin, J-P Tetienne, T Hingant, J-F Roch, P Maletinsky, and V Jacques. Magnetometry with nitrogen-vacancy defects in diamond. *Rep. Prog. Phys.*, 77(5):056503, May 2014.

[91] N. B Manson, M. Hedges, M. S. J. Barson, R. Ahlefeldt, M. W. Doherty, H. Abe, T. Ohshima, and M. J. Sellars. Nv^- - n^+ pair centre in 1b diamond. *New Journal of Physics*, 20(11):113037, nov 2018.

[92] P. Ovartchaiyapong, K. W. Lee, B. A. Myers, and A. C. B. Jayich. Dynamic strain-mediated coupling of a single diamond spin to a mechanical resonator. *Nature Communications*, 5(1):4429, Jul 2014.

[93] J. F. Barry, J. M. Schloss, E. Bauch, M. J. Turner, C. A. Hart, L. M.

Pham, and R. L. Walsworth. Sensitivity optimization for NV-diamond magnetometry. *Rev. Mod. Phys.*, 92(1):015004, March 2020.

[94] M. Fujiwara and Y. Shikano. Diamond quantum thermometry: from foundations to applications. *Nanotechnology*, 32(48):482002, November 2021.

[95] N. B. Manson, J. P. Harrison, and M. J. Sellars. Nitrogen-vacancy center in diamond: Model of the electronic structure and associated dynamics. *Phys. Rev. B*, 74(10):104303, September 2006.

[96] F Jelezko, C Tietz, A Gruber, I Popa, A Nizovtsev, S Kilin, and J Wrachtrup. Spectroscopy of Single N-V Centers in Diamond. *Single Mol.*, page 6, 2001.

[97] K. Oshimi, Y. Nishimura, T. Matsubara, M. Tanaka, E. Shikoh, L. Zhao, Y. Zou, N. Komatsu, Y. Ikado, Y. Takezawa, E. Kage-Nakadai, Y. Izutsu, K. Yoshizato, S. Morita, M. Tokunaga, H. Yukawa, Y. Baba, Y. Teki, and M. Fujiwara. Glass-patternable notch-shaped microwave architecture for on-chip spin detection in biological samples. *Lab Chip*, pages –, 2022.

[98] M. Bass, C. DeCusatis, J. M Enoch, V. Lakshminarayanan, G. Li, C. A. MacDonald, V. N. Mahajan, and E. W. Van Stryland. *Handbook of optics*. McGraw-Hill's AccessEngineering. McGraw-Hill, New York, 3rd ed. edition, 2010.

[99] V. M. Boitsov. Homogeneous and inhomogeneous broadening in the spectra of free complex molecules. *Journal of Applied Spectroscopy*, 36(2):203–206, Feb 1982.

[100] A. O. Levchenko, V. V. Vasil'ev, S. A. Zibrov, A. S. Zibrov, A. V. Sivak, and I. V. Fedotov. Inhomogeneous broadening of optically detected mag-

netic resonance of the ensembles of nitrogen-vacancy centers in diamond by interstitial carbon atoms. *Applied Physics Letters*, 106(10):102402, 2015.

[101] M. Fujiwara, A. Dohms, K. Suto, Y.i Nishimura, K. Oshimi, Y. Teki, K. Cai, O. Benson, and Y. Shikano. Real-time estimation of the optically detected magnetic resonance shift in diamond quantum thermometry toward biological applications. *Phys. Rev. Research*, 2(4):043415, December 2020.

[102] S. Sotoma, D. Terada, T. F. Segawa, R. Igarashi, Y. Harada, and M. Shirakawa. Enrichment of ODMR-active nitrogen-vacancy centres in five-nanometre-sized detonation-synthesized nanodiamonds: Nanoprobes for temperature, angle and position. *Sci Rep*, 8(1):5463, December 2018.

[103] T. Yanagi, K. Kaminaga, W. Kada, O. Hanaizumi, and R. Igarashi. Optimization of wide-field odmr measurements using fluorescent nanodiamonds to improve temperature determination accuracy. *Nanomaterials (Basel, Switzerland)*, 10(11):2282, Nov 2020. 33217922[pmid].

[104] N. Zhang, C. Zhang, L. Xu, M. Ding, W. Quan, Z. Tang, and H. Yuan. Microwave Magnetic Field Coupling with Nitrogen-Vacancy Center Ensembles in Diamond with High Homogeneity. *Appl Magn Reson*, 47(6):589–599, June 2016.

[105] M. W. Doherty, N. B. Manson, P. Delaney, F. Jelezko, J. Wrachtrup, and L. C.L. Hollenberg. The nitrogen-vacancy colour centre in diamond. *Physics Reports*, 528(1):1 – 45, 2013. The nitrogen-vacancy colour centre in diamond.

[106] H. An, Z. Yin, C. Mitchell, A. Semnani, A. R. Hajrasouliha, and M. Hosseini. Nanodiamond ensemble-based temperature measurement in living cells and its limitations. *Measurement Science and Technology*, 32(1):015701, oct 2020.

[107] S. Knauer, J. P. Hadden, and J. G. Rarity. In-situ measurements of fabrication induced strain in diamond photonic-structures using intrinsic colour centres. *npj Quantum Inf*, 6(1):50, December 2020.

[108] F. Jelezko and J. Wrachtrup. Single defect centres in diamond: A review. *phys. stat. sol. (a)*, 203(13):3207–3225, October 2006.

[109] O. R. Opaluch, N. Oshnik, R. Nelz, and E. Neu. Optimized Planar Microwave Antenna for Nitrogen Vacancy Center Based Sensing Applications. *Nanomaterials*, 11(8):2108, August 2021.

[110] R. Hanson, O. Gywat, and D. D. Awschalom. Room-temperature manipulation and decoherence of a single spin in diamond. *Phys. Rev. B*, 74(16):161203, October 2006.

[111] P. Siyushev, M. Nesladek, E. Bourgeois, M. Gulka, J. Hruby, T. Yamamoto, M. Trupke, T. Teraji, J. Isoya, and F. Jelezko. Photoelectrical imaging and coherent spin-state readout of single nitrogen-vacancy centers in diamond. *Science*, 363(6428):728–731, February 2019.

[112] J. M. Rios. Quantum manipulation of nitrogen-vacancy centers in diamond: from basic properties to applications. page 206.

[113] W.J. Getsinger. An introduction to microwave transmission lines. In *[1992] Proceedings of the 35th Midwest Symposium on Circuits and Systems*, pages 1016–1019, Washington, DC, USA, 1992. IEEE.

[114] S. Rosloniec. Design of Coupled Microstrip Lines by Optimization Methods (Short Paper). *IEEE Trans. Microwave Theory Techn.*, 35(11):1072–1074, November 1987.

[115] B.R. Rao. Effect of Loss and Frequency Dispersion on the Performance of

Microstrip Directional Couplers and Coupled Line Filters (Short Papers). *IEEE Trans. Microwave Theory Techn.*, 22(7):747–750, July 1974.

[116] Microwaves101. Stripline calculator. https://www.microwaves101.com/calculators/1202-stripline-calculator, 2022.

[117] K. L. Chung, H. Tian, S. Wang, B. Feng, and G. Lai. Miniaturization of microwave planar circuits using composite microstrip/coplanar-waveguide transmission lines. *Alexandria Engineering Journal*, 61(11):8933–8942, 2022.

[118] M. E. Robinson, J. D. Ng, H. Zhang, J. T. Buchman, O. A. Shenderova, C. L. Haynes, Zh. Ma, R. H. Goldsmith, and R. J. Hamers. Optically detected magnetic resonance for selective imaging of diamond nanoparticles. *Analytical Chemistry*, 90(1):769–776, 2018. PMID: 29131578.

[119] M. L. Citron, H. R. Gray, C. W. Gabel, and C. R. Stroud. Experimental study of power broadening in a two-level atom. *Phys. Rev. A*, 16(4):1507–1512, October 1977.

[120] L. L. Allen. *Optical resonance and two-level atoms*. Dover, New York, 1987.

[121] G Battaglia, E Brunetti, M M R Chishti, G Lorusso, D O'Donnell, M Scheck, S M Wiggins, and D A Jaroszynski. Laser-driven radioisotopes production at SCAPA for medical and industrial application. *Journal of Physics: Conference Series*, 1643(1):012200, dec 2020.

[122] A. Dréau, M. Lesik, L. Rondin, P. Spinicelli, O. Arcizet, J.-F. Roch, and V. Jacques. Avoiding power broadening in optically detected magnetic resonance of single NV defects for enhanced dc magnetic field sensitivity. *Phys. Rev. B*, 84(19):195204, November 2011.

[123] E. Bourgeois, A. Jarmola, P. Siyushev, M. Gulka, J. Hruby, F. Jelezko, D. Budker, and M. Nesladek. Photoelectric detection of electron spin resonance of nitrogen-vacancy centres in diamond. *Nature Communications*, 6(1):8577, Oct 2015.

[124] Yu-Chen Chen, Benjamin Griffiths, Laiyi Weng, Shannon S. Nicley, Shazeaa N. Ishmael, Yashna Lekhai, Sam Johnson, Colin J. Stephen, Ben L. Green, Gavin W. Morley, Mark E. Newton, Martin J. Booth, Patrick S. Salter, and Jason M. Smith. Laser writing of individual nitrogen-vacancy defects in diamond with near-unity yield. *Optica*, 6(5):662–667, May 2019.

[125] J. Lacoste, C. Vining, D. Zuo, A. Spurmanis, and C. M. Brown. *Optimal Conditions for Live Cell Microscopy and Raster Image Correlation Spectroscopy*, pages 269–309. Springer New York, New York, NY, 2012.

[126] D. J. DeTroye and R. J. Chase. The Calculation and Measurement of Helmholtz Coil Fields:. Technical report, Defense Technical Information Center, Fort Belvoir, VA, November 1994.

[127] B. D. Wood, G. A. Stimpson, J. E. March, Y. N. D. Lekhai, C. J. Stephen, B. L. Green, A. C. Frangeskou, L. Ginés, S. Mandal, O. A. Williams, and G. W. Morley. Long Spin Coherence Times of Nitrogen Vacancy Centres in Milled Nanodiamonds. *arXiv:2112.01899 [cond-mat, physics:physics, physics:quant-ph]*, December 2021. arXiv: 2112.01899.

[128] E. Moreva, E. Bernardi, P. Traina, A. Sosso, S. Ditalia Tchernij, J. Forneris, F. Picollo, G. Brida, Ž. Pastuović, I. P. Degiovanni, P. Olivero, and M. Genovese. Practical Applications of Quantum Sensing: A Simple Method to Enhance the Sensitivity of Nitrogen-Vacancy-Based Temperature Sensors. *Phys. Rev. Applied*, 13(5):054057, May 2020.

[129] L. M. Pham, N. Bar-Gill, D. Le Sage, C. Belthangady, A. Stacey, M. Markham, D. J. Twitchen, M. D. Lukin, and R. L. Walsworth. Enhanced metrology using preferential orientation of nitrogen-vacancy centers in diamond. *Phys. Rev. B*, 86:121202, Sep 2012.

[130] D. A. Simpson, E. Morrisroe, J. M. McCoey, A. H. Lombard, D. C. Mendis, F. Treussart, L. T. Hall, S. Petrou, and L. C. L. Hollenberg. Non-neurotoxic nanodiamond probes for intraneuronal temperature mapping. *ACS Nano*, 11(12):12077–12086, 2017. PMID: 29111670.

[131] Z. Wang, D. Wei, L. Wei, Y. He, G. Shi, X. Wei, and Y. Zhang. Aberration correction during real time in vivo imaging of bone marrow with sensorless adaptive optics confocal microscope. *Journal of Biomedical Optics*, 19(8):1 – 7, 2014.

[132] Martin J. Booth, Mark A. A. Neil, Rimas Juškaitis, and Tony Wilson. Adaptive aberration correction in a confocal microscope. *Proceedings of the National Academy of Sciences*, 99(9):5788–5792, 2002.

[133] K. Hayashi, Y. Matsuzaki, T. Taniguchi, T. Shimo-Oka, I. Nakamura, S. Onoda, T. Ohshima, H. Morishita, M. Fujiwara, S. Saito, and N. Mizuochi. Optimization of Temperature Sensitivity Using the Optically Detected Magnetic-Resonance Spectrum of a Nitrogen-Vacancy Center Ensemble. *Phys. Rev. Applied*, 10(3):034009, September 2018.

[134] Yuen Y. H., W. W-W. Hsiao, S. Haziza, M. Simonneau, F. Treussart, and H-C. Chang. Single particle tracking of fluorescent nanodiamonds in cells and organisms. *Current Opinion in Solid State and Materials Science*, 21(1):35–42, 2017. Nanodiamond Science and Technology.

[135] Y. Wu, Y. Rivenson, H. Wang, Y. Luo, E. Ben-David, L. A. Bentolila, C. Pritz, and A. Ozcan. Three-dimensional virtual refocusing of fluorescence

microscopy images using deep learning. *Nature Methods*, 16(12):1323–1331, Dec 2019.

[136] A. J. Wright and S. P. Poland. *Adaptive Optics for Aberration Correction in Optical Microscopy*, pages 585–612. Springer Netherlands, Dordrecht, 2017.

[137] L. Sherman, J. Y. Ye, O. Albert, and T. B. Norris. Adaptive correction of depth-induced aberrations in multiphoton scanning microscopy using a deformable mirror. *Journal of Microscopy*, 206(1):65–71, 2002.

[138] M. W. Doherty, V. M. Acosta, A. Jarmola, M. S. J. Barson, N. B. Manson, D. Budker, and L. C. L. Hollenberg. Temperature shifts of the resonances of the nv^- center in diamond. *Phys. Rev. B*, 90:041201, Jul 2014.

[139] D. L. Coutu and T. Schroeder. Probing cellular processes by long-term live imaging – historic problems and current solutions. *Journal of Cell Science*, 126(17):3805–3815, 09 2013.

[140] R. Dixit and R. Cyr. Cell damage and reactive oxygen species production induced by fluorescence microscopy: effect on mitosis and guidelines for non-invasive fluorescence microscopy. *The Plant Journal*, 36(2):280–290, 2003.

[141] E. I. Baibekov. Decay of rabi oscillations induced by magnetic dipole interactions in dilute paramagnetic solids. *JETP Letters*, 93(5):292, May 2011.

[142] E. Perevedentseva, S.-F. Hong, K.-J. Huang, I.-T. Chiang, C.-Y. Lee, Y.-T. Tseng, and C.-L. Cheng. Nanodiamond internalization in cells and the cell uptake mechanism. *Journal of Nanoparticle Research*, 15(8):1834, Jul 2013.

[143] S. Behzadi, V. Serpooshan, W. Tao, M. A. Hamaly, M. Y. Alkawareek, E. C. Dreaden, D. Brown, A. M. Alkilany, O. C. Farokhzad, and M. Mahmoudi. Cellular uptake of nanoparticles: journey inside the cell. *Chem. Soc. Rev.*, 46:4218–4244, 2017.

[144] M. A. Elhelu. The role of macrophages in immunology. *Journal of the National Medical Association*, 75(3):314–317, Mar 1983. 6343621[pmid].

[145] M. Kenneth and W. Casey. *Janeway's Immunobiology.*, volume 9th edition. W.W. Norton & Company, 2017.

[146] S. S. Evans, E. A. Repasky, and D. T. Fisher. Fever and the thermal regulation of immunity: the immune system feels the heat. *Nature reviews. Immunology*, 15(6):335–349, Jun 2015. 25976513[pmid].

[147] S. Tsuchiya, M. Yamabe, Y. Yamaguchi, Y. Kobayashi, T. Konno, and K. Tada. Establishment and characterization of a human acute monocytic leukemia cell line (thp-1). *International Journal of Cancer*, 26(2):171–176, 1980.

[148] P. Zwicker, T. Schmidt, M. Hornschuh, H. Lode, A. Kramer, and G. Müller. In vitro response of thp-1 derived macrophages to antimicrobially effective phmb-coated ti6al4v alloy implant material with and without contamination with s. epidermidis and p. aeruginosa. *Biomaterials Research*, 26(1):1, Jan 2022.

[149] SD Grant, GS Cairns, J Wistuba, and BR Patton. Adapting the 3d-printed openflexure microscope enables computational super-resolution imaging [version 1; peer review: 2 approved]. *F1000Research*, 8(2003), 2019.

[150] N. Billinton and A. W. Knight. Seeing the wood through the trees: A review

of techniques for distinguishing green fluorescent protein from endogenous autofluorescence. *Analytical Biochemistry*, 291(2):175–197, 2001.

[151] D. Khanal, Q. Lei, G. Pinget, D. A. Cheong, A. Gautam, R. Yusoff, B. Su, S. Yamaguchi, A. Kondyurin, J. C. Knowles, G. Georgiou, L. Macia, J-H Jang, I. Ramzan, K. W. Ng, and W. Chrzanowski. The protein corona determines the cytotoxicity of nanodiamonds: implications of corona formation and its remodelling on nanodiamond applications in biomedical imaging and drug delivery. *Nanoscale Adv.*, 2:4798–4812, 2020.

[152] Q.-Y. Cao, P.-C. Yang, M.-S. Gong, M. Yu, A. Retzker, M.B. Plenio, C. Müller, N. Tomek, B. Naydenov, L.P. McGuinness, F. Jelezko, and J.-M. Cai. Protecting quantum spin coherence of nanodiamonds in living cells. *Phys. Rev. Applied*, 13:024021, Feb 2020.

[153] X.-D. Chen, C.-H. Dong, F.-W. Sun, C.-L. Zou, J.-M. Cui, Z.-F. Han, and G.-C. Guo. Temperature dependent energy level shifts of nitrogen-vacancy centers in diamond. *Appl. Phys. Lett.*, 99(16):161903, October 2011.

[154] AM Zaitsev. Optical properties of diamond: A data handbook, 1–3 springer-verlag berlin heidelberg. *New York*, 2001.

[155] S. O. Hruszkewycz, W. Cha, P. Andrich, C. P. Anderson, A. Ulvestad, R. Harder, P. H. Fuoss, D. D. Awschalom, and F. J. Heremans. In situ study of annealing-induced strain relaxation in diamond nanoparticles using bragg coherent diffraction imaging. *APL Materials*, 5(2):026105, 2017.

[156] L. P. McGuinness, Y. Yan, A. Stacey, D. A. Simpson, L. T. Hall, D. Maclaurin, S. Prawer, P. Mulvaney, J. Wrachtrup, F. Caruso, R. E. Scholten, and L. C. L. Hollenberg. Quantum measurement and orientation tracking of fluorescent nanodiamonds inside living cells. *Nature Nanotech*, 6(6):358–363, June 2011.

[157] Y. Nishimura, K. Oshimi, Y. Umehara, Y. Kumon, K. Miyaji, H. Yukawa, Y. Shikano, T. Matsubara, M. Fujiwara, Y. Baba, and Y. Teki. Wide-field fluorescent nanodiamond spin measurements toward real-time large-area intracellular thermometry. *Sci Rep*, 11(1):4248, December 2021.

[158] J. C. Price, R. Mesquita-Ribeiro, F. Dajas-Bailador, and M. L. Mather. Widefield, spatiotemporal mapping of spontaneous activity of mouse cultured neuronal networks using quantum diamond sensors. *Frontiers in Physics*, 8, 2020.

[159] C. Foy, L. Zhang, M. E. Trusheim, K. R. Bagnall, M. Walsh, E. N. Wang, and D. R. Englund. Wide-field Magnetic Field and Temperature Imaging using Nanoscale Quantum Sensors. *arXiv:1903.05717 [physics]*, March 2019. arXiv: 1903.05717.

[160] L. Caruso, T. Wunderle, C. M. Lewis, J. Valadeiro, V. Trauchessec, J. Trejo Rosillo, J. P. Amaral, J. Ni, P. Jendritza, C. Fermon, S. Cardoso, P. P. Freitas, P. Fries, and M. Pannetier-Lecoeur. In vivo magnetic recording of neuronal activity. *Neuron*, 95(6):1283–1291.e4, Sep 2017. 28844526[pmid].

[161] J. Velmurugan, S. Sinha, and P. Satishchandra. Magnetoencephalography recording and analysis. *Annals of Indian Academy of Neurology*, 17(Suppl 1):S113–S119, Mar 2014. 24791077[pmid].

[162] Akihiro Kuwahata, Takahiro Kitaizumi, Kota Saichi, Takumi Sato, Ryuji Igarashi, Takeshi Ohshima, Yuta Masuyama, Takayuki Iwasaki, Mutsuko Hatano, Fedor Jelezko, Moriaki Kusakabe, Takashi Yatsui, and Masaki Sekino. Magnetometer with nitrogen-vacancy center in a bulk diamond for detecting magnetic nanoparticles in biomedical applications. *Sci Rep*, 10(1):2483, December 2020.

[163] R. L. Patel, L. Q. Zhou, A. C. Frangeskou, G. A. Stimpson, B. G. Breeze, A. Nikitin, M. W. Dale, E. C. Nichols, W. Thornley, B. L. Green, M. E. Newton, A. M. Edmonds, M. L. Markham, D. J. Twitchen, and G. W. Morley. Sub-nanotesla magnetometry with a fibre-coupled diamond sensor. *arXiv:2002.08255 [physics]*, February 2020. arXiv: 2002.08255.

[164] M. Parashar, A. Bathla, D. Shishir, A. Gokhale, S. Bandyopadhyay, and K. Saha. Sub-second temporal magnetic field microscopy using quantum defects in diamond. *Scientific Reports*, 12(1):8743, May 2022.

[165] I. V. Fedotov, L. V. Doronina-Amitonova, A. A. Voronin, A. O. Levchenko, S. A. Zibrov, D. A. Sidorov-Biryukov, A. B. Fedotov, V. L. Velichansky, and A. M. Zheltikov. Electron spin manipulation and readout through an optical fiber. *Scientific Reports*, 4(1):5362, Jul 2014.

[166] G. Vicidomini, P. Bianchini, and A. Diaspro. Sted super-resolved microscopy. *Nature Methods*, 15(3):173–182, Mar 2018.

[167] B. Harke, J. Keller, C. K. Ullal, V. Westphal, A. Schönle, and S. W. Hell. Resolution scaling in sted microscopy. *Opt. Express*, 16(6):4154–4162, Mar 2008.

[168] T. Müller, C. Schumann, and A. Kraegeloh. Sted microscopy and its applications: New insights into cellular processes on the nanoscale. *ChemPhysChem*, 13(8):1986–2000, 2012.

[169] G. Laporte and D. Psaltis. Sted imaging of green fluorescent nanodiamonds containing nitrogen-vacancy-nitrogen centers. *Biomedical optics express*, 7(1):34–44, Dec 2015. 26819815[pmid].

[170] B. M. Heffernan, S. A. Meyer, D. Restrepo, M. E. Siemens, E. A. Gibson, and J. T. Gopinath. A fiber-coupled stimulated emission depletion

microscope for bend-insensitive through-fiber imaging. *Scientific Reports*, 9(1):11137, Jul 2019.

[171] H. Blom and H. Brismar. Sted microscopy: increased resolution for medical research? *Journal of Internal Medicine*, 276(6):560–578, 2014.